Spring 2020

Design of x-ray source for real-time computed tomography

Wesley William Tucker

DESIGN OF X-RAY SOURCE FOR REAL-TIME COMPUTED TOMOGRAPHY

by

WESLEY WILLIAM TUCKER

A DISSERTATION

Presented to the Graduate Faculty of the

MISSOURI UNIVERSITY OF SCIENCE AND TECHNOLOGY

In Partial Fulfillment of the Requirements for the Degree

DOCTOR OF PHILOSOPHY

in

NUCLEAR ENGINEERING

2020

Approved by:

Hyoung Koo Lee, Advisor
Carlos Castaño
Samuel Frimpong
Gary Mueller
Tiezhi Zhang

ABSTRACT

The reduction of motion blur in computed tomography (CT) drives the current research for multisource CT. Due to their compact nature, the current multisource systems utilize stationary angled anodes. Unfortunately, these configurations neither simplify the imaging geometry, nor satisfy the need for managing the high thermal loads demanded by real-time CT (30 acquisition frames per second). To add to the current field of knowledge, two x-ray tube concepts are presented in this dissertation. First, a simulation of transient thermal analysis was performed on a compact transmission-type x-ray tube anode operating in pulse-mode. A correlation was found between deposited beam power and maximum anode temperature for any anode thickness beyond 0.5 mm.

A second approach was developed for higher current applications: a rotating cylindrical anode. A modified Oosterkamp equation was developed and used to investigate three beam-sweeping sequences. It was found that although increasing beam sweeping speed increased the maximum power, the deposited energy in the focal spot per acquisition time decreased. Ultimately the step-and shoot sequence was found to be optimal for the cylindrical anode. Next, MCNP was used to find the angular dependence of the fraction of energy that the backscattered electrons carry away from the focal spot for a curved anode. That information was then used in COMSOL to find the electron beam efficiency and maximum power for different incident angles using various focal spot lengths and anode diameters. After that a correlation between maximum deposited power, focal spot length, and rotational surface speed was found. Finally, design considerations are reported based upon a sensitivity analysis of a preliminary design for the cylindrical multisource anode.

ACKNOWLEDGMENTS

I want to give thanks to the individuals who helped me throughout my graduate career. To my advisor, Dr. Lee, thank you for guiding me through this process. It wasn't easy for both of us, but I couldn't have made it without your guidance and sense of humor. To my committee members- Dr. Castaño, Dr. Frimpong, Dr. Mueller, and Dr. Zhang- thank you for meeting with me when I had questions about my work (and your work). You always made time for me, even though I know you were busy. To Ashish, my dear friend, thank you for all your advice. My life would have been so much easier if I would have just listened to it. To Amanda, my wife, thank you for your patience over these past four years. You are my best friend.

I would also like to thank the Department of Education for supporting my education through the GAANN Fellowship. This work is supported by grant number P200A150327.

TABLE OF CONTENTS

Page

ABSTRACT iii

ACKNOWLEDGMENTS iv

LIST OF ILLUSTRATIONS x

LIST OF TABLES xiii

SECTION

1. INTRODUCTION 1

1.1. BACKGROUND OF THE RESEARCH PROBLEM 1

1.2. STATEMENT OF THE RESEARCH PROBLEM 2

1.3. RESEARCH OBJECTIVES AND SCOPE 3

1.4. RESEARCH METHODOLOGY 6

1.5. SCIENTIFIC CONTRIBUTIONS 7

1.6. STRUCTURE OF DISSERTATION 8

2. LITERATURE REVIEW 9

2.1. X-RAY COMPONENTS 9

2.1.1. Cathode. 9

2.1.2. Anode. 12

2.2. HEAT MANAGEMENT IN DIAGNOSTIC X-RAY ANODES 12

2.2.1. Deposition of Electron Energy in the Anode. 12

2.2.2. Focal Spot. 13

2.2.3. Electron Interaction Outside the Focal Spot. 14

2.2.3.1. Electron backscatter. 14

2.2.3.2. Off-focal radiation and electron trap. 15

2.2.4. X-Ray Anode Designs. 16

2.2.4.1. Transmission anodes. 16

2.2.4.2. Stationary angled anodes. 17

2.2.4.3. Rotating angled anodes. 18

2.3. COMPUTED TOMOGRAPHY 19

2.3.1. First-Generation. 20

2.3.2. Second-Generation. 21

2.3.3. Third-Generation. 21

2.3.4. Fourth-Generation. 21

2.3.5. Cardiac CT. 22

2.4. DISTRIBUTED SOURCE AND MULTISOURCE COMPUTED TOMOGRAPHY 23

2.4.1. Multisource X-Ray Systems. 24

2.4.2. Multisource CT. 25

3. TRANSMISSION TUBE SETUP AND SIMULATION 27

3.1. TUBE DESIGN 27

3.1.1. Cathode Assembly. 28

3.1.1.1. Tungsten filament. 28

3.1.1.2. Focusing cup. 29

3.1.2. Electrostatic Lenses. 29

3.1.2.1. Lens groups. 29

3.1.2.2. Particle-In-Cell (PIC) simulation. 30

3.2. COMSOL SIMULATION 31

3.2.1. Stationary CT Design. 31

3.2.2. Methods for COMSOL Simulation. 31

3.2.2.1. Electron deposition. 32

3.2.2.2. Spectrum simulation in MCNP. 33

3.2.2.3. Modeling maximum temperature rise of anode. 34

3.2.3. Results for COMSOL Simulation. 36

3.2.3.1. Electron deposition. 36

3.2.3.2. Maximum temperature rise of anode. 37

3.2.3.3. Temperature VS beam power. 39

3.2.3.4. Spectrum. 40

3.2.4. Summary of Findings. 41

3.3. CYLINDRICAL ANODE 42

4. COMPARISON OF ELECTRON BEAM SEQUENCES FOR ROTATING CYLINDER MULTISOURCE ANODE 43

4.1. METHODS FOR SWEEPING STUDY 44

4.1.1. Modifying the Oosterkamp Equation. 44

4.1.2. COMSOL Simulations. 48

4.1.2.1. Step-and-shoot sequence 49

4.1.2.2. X-sweeping with rotation sequence. 50

4.1.2.3. Y-sweeping with rotation sequence. 51

4.2. RESULTS FOR SWEEPING STUDY 52

4.2.1. Pulse Shape and Deposited Power Definition for COMSOL Simulations. 56

4.2.2. Comparing Deposited Power Capabilities for X-Sweeping and Y-Sweeping. 57

4.2.3. Step-And-Shoot. 61

4.3. DISCUSSION 62

4.4. CONCLUSIONS FOR SWEEPING STUDY 63

5. DESIGN CONSIDERATIONS FOR CYLINDER MULTISOURCE ANODE 64

5.1. METHODS FOR DESIGN CONSIDERATIONS 65

5.1.1. Description of the Geometry. 67

5.1.2. Angular Dependence of Backscatter Energy Fraction. 67

5.1.3. Finite Element Simulation. 69

5.1.3.1. Power efficiency per incident beam angle. 69

5.1.3.2. Maximum deposited power per angle. 70

5.1.3.3. Sensitivity analysis of thermal properties and dimension changes. 71

5.2. RESULTS FOR DESIGN CONSIDERATIONS 72

5.2.1. Electron Backscatter. 72

5.2.2. Power Efficiency. 73

5.2.3. Rotation Direction and L/d. 74

5.2.4. Maximum Deposited Power VS Focal Spot Size and Rotational Speed. 75

5.2.5. Sensitivity Analysis. 75

5.3. DESIGN IMPLICATIONS AND DISCUSSION 77

5.4. CONCLUSIONS FOR DESIGN CONSIDERATIONS 78

6. DISCUSSION AND CONCLUSION 79

6.1. GENERAL CONCLUSIONS 79

6.2. FUTURE WORK 80

REFERENCES 81

VITA 90

LIST OF ILLUSTRATIONS

Figure Page

1.1 G-force as a function of gantry rotation frequency 2

1.2 Schematic of proposed stationary CT architecture utilizing transmission anodes 4

1.3 Basic design of the cylindrical multisource x-ray system 6

2.1 Diagram of a simple x-ray tube 9

2.2 Grid switching of the focusing cup 10

2.3 Visual example of the inefficiency of the x-ray production process 11

2.4 Monte Carlo simulation of a 1 μm diameter beam of 100 keV electrons interacting in an infinite tungsten layer 13

2.5 a) Off-focal radiation caused by small interelectrode distance b) Philips iMRC utilizes an electron trap 15

2.6 Transmission x-ray tube 16

2.7 X-ray tube utilizing stationary angled anode 17

2.8 Rotating anode with line focus 19

2.9 CT scanner setup of Hounsfield experiment at EMI laboratory 20

2.10 Generations of computed tomography scanners 22

2.11 Intrinsic antiscatter properties of inverse geometry 24

2.12 Electron beam CT 26

3.1 Schematic of linear x-ray tube 27

3.2 CAD model of cathode assembly 28

3.3 OOPIC output 29

3.4 Schematic of stationary CT with 3 simultaneously firing projections 32

3.5 MCNP geometry for spectrum comparison of a 60 keV beam attenuated by 0.5 mm of beryllium, copper, or aluminum 33

3.6 A detailed schematic of the geometry of the transmission-type anode 35

3.7 Electron heat deposition in tungsten with aluminum anode 36

3.8 Electron heat deposition in tungsten with beryllium anode 37

3.9 Electron heat deposition in tungsten with copper anode 37

3.10 Comparison study of pulses using volume function input and surface heat flux 38

3.11 Maximum Single Pulse temperature for anode thicknesses between 0.05 mm and 2 mm for (a) 30 keV. (b) 60 keV. (c) 100 keV. (d) 150 keV 39

3.12 Maximum Peak Pulse temperature for anode thicknesses between 0.05 mm and 2 mm for (a) 30 keV. (b) 60 keV. (c) 100 keV. (d) 150 keV 40

3.13 Relationship of beam power to maximum temperature in the anode 41

3.14 60 keV x-ray spectra comparison for 0.5 mm anode block 42

4.1 Rough schematic of cylinder CT array 44

4.2 Visual representation of focal spot variables 46

4.3 Different sequences being tested 48

4.4 COMSOL simulation for step-and-shoot 53

4.5 COMSOL simulation for X-sweeping 54

4.6 COMSOL simulation for Y-sweeping 55

4.7 Maximum deposited power for a) 0.9 mm wide x-sweeping b) 6.3 mm long y-sweeping 59

4.8 Energy deposited in focal spot for: a) x-sweeping b) y-sweeping 60

4.9 Energy deposited in focal spot for step-and-shoot beam sequence 61

4.10 Deposited power vs rotational surface speed 62

5.1 Cross-section of the cylinder multisource x-ray anode 65

5.2 Geometry of the cylindrical anode 66

5.3 MCNP geometry 68

5.4 Backscatter electron energy fraction 72

5.5 Power efficiency per angle 73

5.6 Effect of L/d, rotation direction, and beam angle on normalized deposited power 74

5.7 Maximum deposited power vs speed and focal spot length 75

5.8 Sensitivity analysis 76

LIST OF TABLES

Table Page

5.1 Baseline Properties..... 71

1. INTRODUCTION

Research in computed tomography (CT) has not slowed down since its inception in 1973. With the advent of multidetector row CT[1], helical CT [2], [3], and dual-source CT[4]–[6], the scanning times for volumetric acquisitions have become lightning fast. However, even modern designs are still based on the rotating gantry concept developed 50 years ago, which significantly hampers any major advancements in temporal resolution[7].

1.1. BACKGROUND OF THE RESEARCH PROBLEM

Reduction of cardiac motion blur is the main driving force for the appearance of multisource x-ray designs[8]. In order to acquire the adequate information to reconstruct a 2D slice in a traditional CT, the source-detector pair must travel 180° (plus the fan angle of the beam) around the object being imaged. The time it takes to do this is called the CT scanner's temporal resolution. But if there are two pairs of source-detector sets[4], then you only have to travel half the distance to get the same information, implying that the temporal resolution could be halved. Extrapolating this concept to its logical end by creating an array of sources that completely surround the imaging object would mean rotation would be totally eliminated and the temporal resolution would only be limited by the speed at which the x-ray sources could be activated. This is the rationale behind the development of some of the previous multisource CT systems.

Recent investigations into multisource x-ray imaging have yielded fascinating results. Inverse geometry and tetrahedron beam computed tomography (TBCT) broke new ground in beam architecture and volumetric data acquisition[9]–[12]. Stationary CT

architectures potentially improve reliability while also increasing temporal resolution[13]–[17]. Due to space constraints, these designs used stationary anodes. This limits the maximum deposited power, and consequently, the x-ray output power.

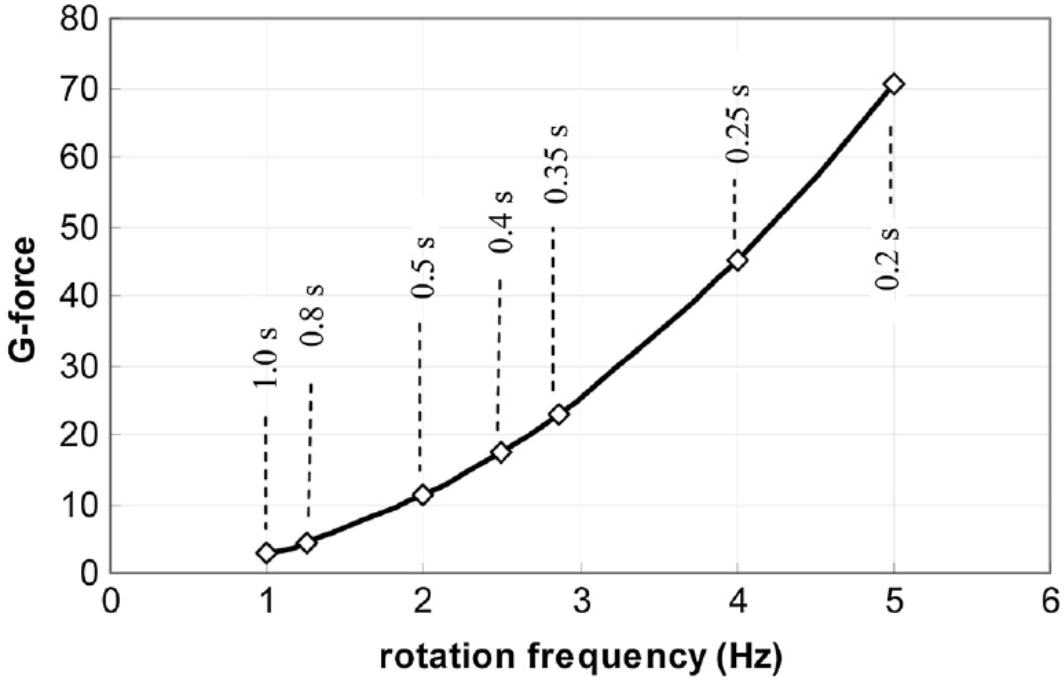

Figure 1.1 G-force as a function of gantry rotation frequency [3]

1.2. STATEMENT OF THE RESEARCH PROBLEM

3rd generation design requires that the source and detector rotate around the gantry to acquire projections from all angles. These systems can reach up to 1000 kg[3]. Since the centrifugal force acting on the gantry increases with the square of rotational frequency, bringing the acquisition rate to real-time (30 acquisition-frames per second) would create incredible stress on the gantry (Figure 1.1). The conclusion one could draw from this is that real-time CT cannot be reached using the conventional 3rd generation CT architecture.

In order to achieve real-time CT, the rotational motion of the gantry needs to be completely eliminated. In its place, a ring of stationary source spots completely surrounding the imaging object (i.e. the patient) is placed next to a detector ring (Figure 1.2). With the gantry rotation gone, temporal resolution is limited by the amount of energy that can be deposited per focal spot needed to maintain image quality. We estimate the goal for most applications is around 9-10 joules deposited per focal spot based on previous cardiac CT outputs[18].

Increasing the temporal resolution means that the energy is deposited during a shorter period of time, meaning the deposited heat rate increases linearly with increasing temporal resolution. This increase in heat rate, if not properly managed, causes an increase in temperatures which can lead to x-ray tube failures. Thus, the management of heat in the anode is one of the main limiting factors in increasing the temporal resolution in multisource CT systems to real-time.

1.3. RESEARCH OBJECTIVES AND SCOPE

This work seeks to investigate the feasibility of two multisource concepts intended for real-time CT (30 acquisition-frames per second) in the scope of heat transfer. The first is a linear x-ray tube utilizing a transmission anode and electrostatic lenses as part of a continuous, long-term research project for stationary CT architecture[19]–[21]. Recent innovations in CT reconstruction using compressed sensing allows for a small number of source projections in order to attain quality images[22]. Thanks to that concept, we placed around 200 linear tube sources in a ring, each tilted towards a neighboring detector ring.

The completely stationary design would provide a reliable and fast alternative to third generation CT (Figure 1.2).

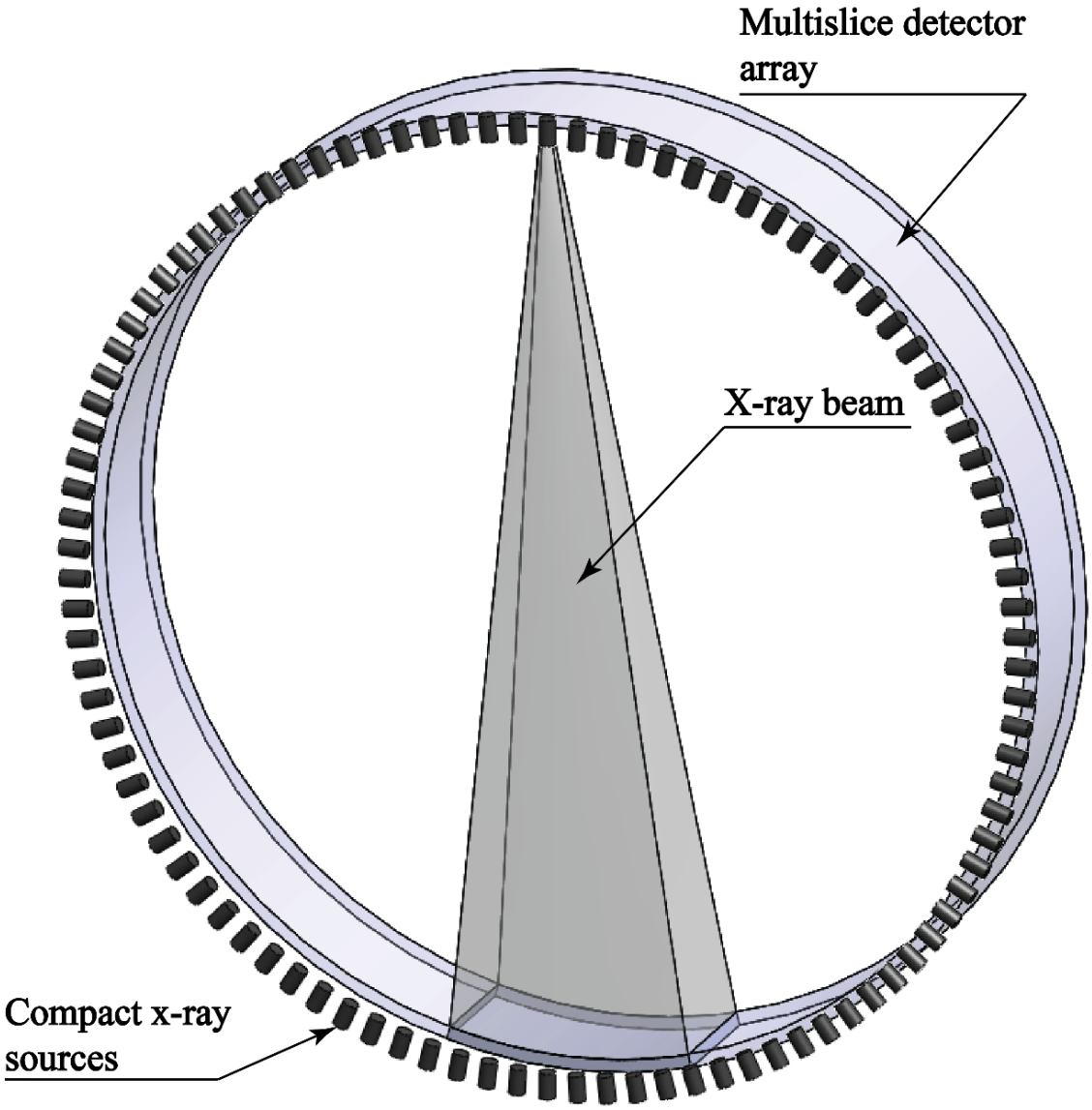

Figure 1.2 Schematic of proposed stationary CT architecture utilizing transmission anodes

To determine the feasibility of the stationary CT system, a thermal analysis had to be performed. The physical design of the transmission anode was the primary focus of the research. Tungsten thickness and anode material were determined from a list of previously investigated parameters. The detector ring design was not taken into consideration. Other forms of electron emission, such as field emission, were not taken into consideration as these had already been investigated elsewhere[23]–[26].

The second design is a rotating cylinder anode proposed to be used in a multisource module[27] (Figure 1.3). The anode would have the same benefits as previous attempts at multisource designs, such as line focusing and fast pulsed-beam sequences, but would allow for a significant increase in power due to the rotating motion of the cylinder. The transition from stationary to rotating has already been seen in conventional x-ray tubes. The rotating disk anode (see Section 2.2.4.3) is commonly used in CT scanners today. The disk diameters can reach up to 200 mm[28], meaning it would be impossible to distribute them in a multisource configuration with enough focal spots.

The work for the cylinder anode will be limited to just the novelties of the anode structure without any strong consideration of module design. Previous versions of multisource designs have used a magnetically swept electron beam sequence[17], [29]–[31]. The consequence of applying this sequence, as well as our own sequences, to the rotating anode will be investigated. Also, the effects of a curved surface on heat deposition distribution will be studied. Finally, design considerations for a research prototype anode concept will be given based upon a sensitivity analysis for various parameters considered in design.

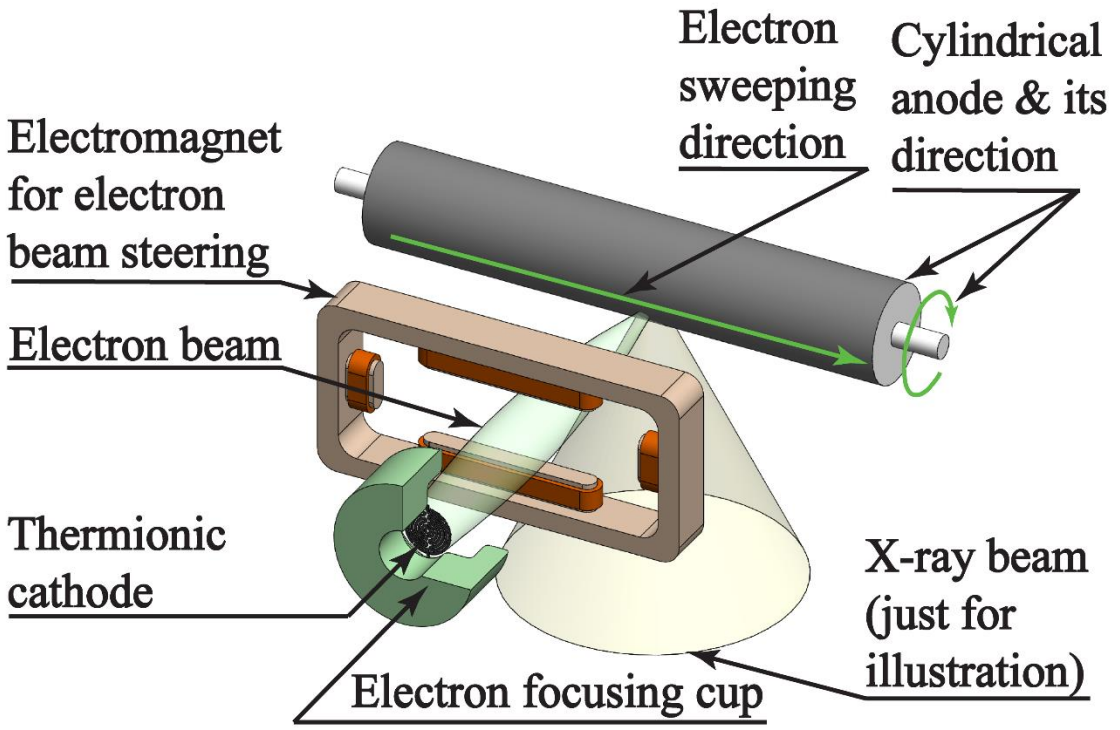

Figure 1.3 Basic design of the cylindrical multisource x-ray system

1.4. RESEARCH METHODOLOGY

This research uses a combination of literature review, mathematical and numerical modeling, and analysis of simulation results to investigate the research objective. The literature review is used to define the frontier of knowledge and act as a compass for the needed analysis. It also forms the foundation to the mathematical modeling of temperature rise that is used for comparing beam sweeping sequences.

Electron interaction with the target material is modeled using two Monte Carlo software CASINO [32] and MCNP [33]. CASINO is used to find the energy and material

dependent electron heat deposition for the thermal analysis of the transmission anode. The output is used as a depth dependent heat profile in COMSOL Multiphysics [34] software.

MCNP is used to find the angular dependence of the energy spectrum and backscatter fraction of electrons impinging on a tungsten surface. This information is then used as an input for the Heat Flux Node in COMSOL, allowing for the differential heat distribution to be mapped for any combination of incident angle and focal-spot-length-to-diameter ratio.

COMSOL Multiphysics is used to model heat transfer in conduction, convection, and radiative emission. In this particular application, the maximum temperature in the anode is found for different power inputs, geometries, and materials. This relation is analyzed in MATLAB and organized in a form that allows the reader to easily ascertain the novelties of the results.

1.5. SCIENTIFIC CONTRIBUTIONS

This work contributes to the overall goal of real-time CT. Previous attempts at multisource anodes have used a stationary anode. This work is the first to utilize a rotating cylinder anode that significantly increases the thermal loading in the system. Using the results in this research, a designer can efficiently navigate the novelties that the cylinder anode provides, giving rise to the ultimate goal of real-time CT. Applications of this technology can be used in cardiac CT and research in traumatic brain injury, as well as Tetrahedron Beam CT in radiation therapy devices.

1.6. STRUCTURE OF DISSERTATION

This dissertation is organized as follows: Section 1 introduces the novelties and objectives of the research. Section 2 gives a literature review of the relevant material to understand the problem and frontier of knowledge. Section 3 contains the study for the transmission-type anode design. Section 4 introduces the cylindrical multisource anode and compares three types of 2-D beam sweeping techniques. Section 5 presents some design considerations for the cylindrical multisource anode. Section 6 gives some general conclusions from the work, as well as set the stage for future research. At the end of the dissertation is a list of references used throughout the research.

2. LITERATURE REVIEW

2.1. X-RAY COMPONENTS

Section 2.1 talks about the relevant components of a conventional x-ray tube in the scope of this dissertation.

2.1.1. Cathode. From a technical standpoint, x-ray generation is a fairly straight-forward process. All you need is an electron emitter (cathode), a high-Z target (anode), and a way to accelerate the electrons (Figure 2.1). Most cathodes used in conventional x-ray tubes primarily operate from a mechanism called thermionic emission where the cathode filament is heated up to a couple thousand degrees, allowing a current of electrons to escape

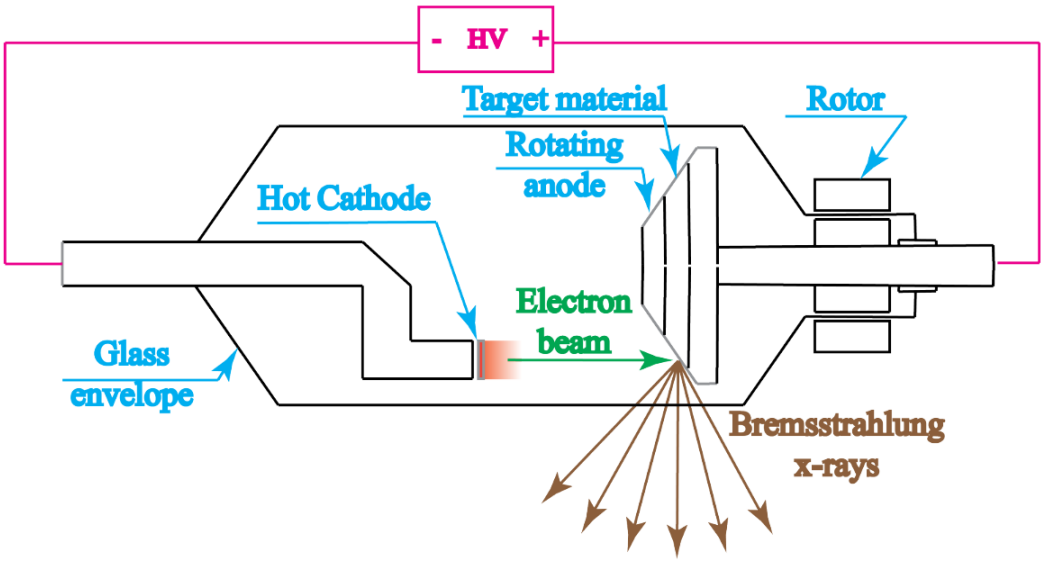

Figure 2.1 Diagram of a simple x-ray tube. An electric potential is applied between a cathode and anode. Electrons released from the cathode accelerate towards the anode, producing x-rays useful for imaging. [19]

the metal and enter the tube vacuum[35]. The relationship between filament temperature and electron current density can be estimated by the Richardson equation.

$$J = A(1 - r)T^2 e^{(-\Phi/KT)} \quad (1)$$

where J is the current density, A is Richardson's constant, r is the reflection coefficient, T is temperature, Φ is work function, and k is Boltzmann's constant. The ideal choice for filament material would be a metal that has a very high melting temperature and a low work function. Tungsten (or tungsten alloy) is typically the choice for such an application; and although it doesn't have the lowest work function, its high melting temperature (3400°C) more than makes up for it.

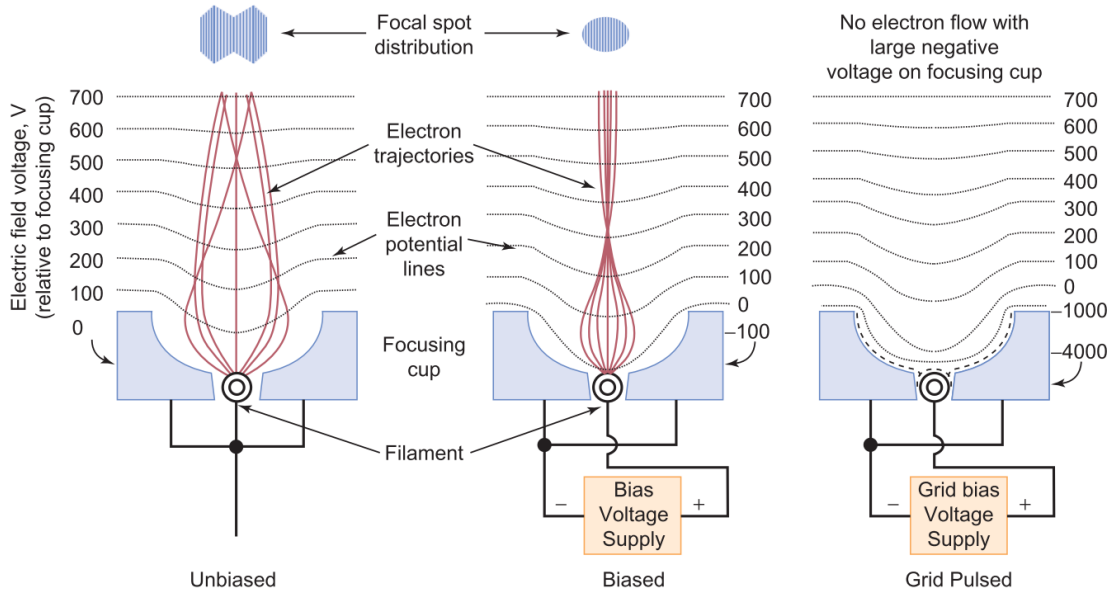

Figure 2.2 Grid switching of the focusing cup. The cup on the left shows the electron beam trajectory being shaped by the focusing cup at the same electric potential as the filament. Notice how the focal spot is blurry and unformed. Applying a slightly negative potential to the cup relative to the filament further compresses the electron beam, creating a more focused focal spot (in the middle). Applying a largely negative bias voltage to the cup completely shuts off the flow of electrons (right). [36]

Surrounding the filament is the focusing cup. This acts as a form of control and focus for the flow of electrons from the cathode down to the anode, which is held at a more positive potential[36]. When the focusing cup is at the same voltage as the hot filament, the electrons leave the cathode (unfocused) and bombard the anode (Figure 2.2 on the left). Applying a slightly negative bias to the focusing cup creates a repelling force on the electron stream and focuses the beam into a point-like spot on the anode target (Figure 2.2 in the center). Lowering the relative potential on the focusing cup even further will eventually raise the 0 V potential line above the surface of the filament, shutting off the flow of electrons altogether (Figure 2.2 on the right). Quickly fluctuating the focusing cup potential allows for the electron beam to be pulsed on and off as needed. This action is called grid-switching.

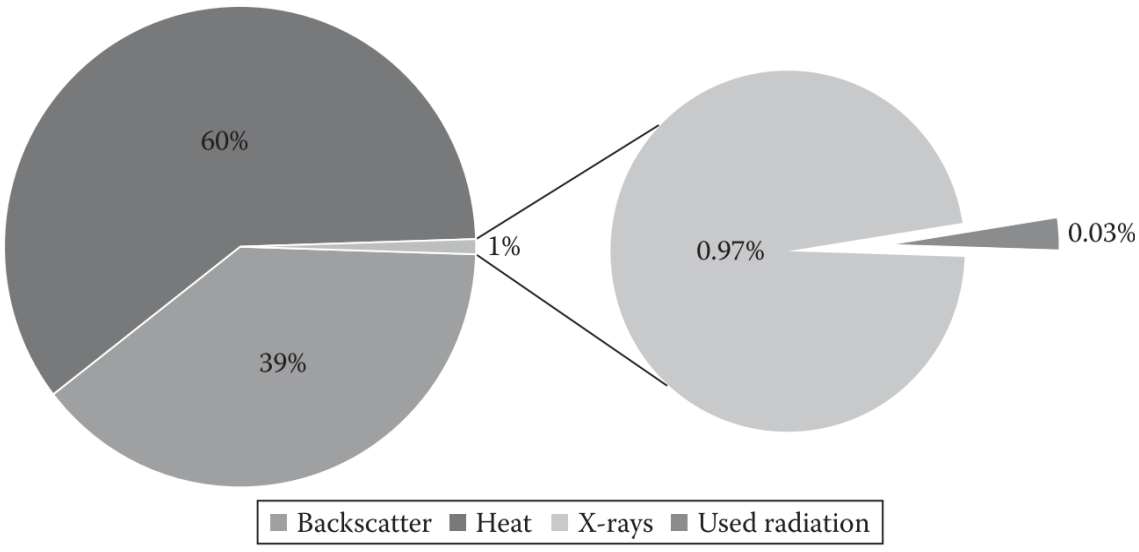

Figure 2.3 Visual example of the inefficiency of the x-ray production process. Values used are for 100 keV electron energies[37].

2.1.2. Anode. The newly emitted electrons are accelerated across the x-ray tube by the potential difference between the cathode and anode. The anode has two primary functions: generation of x-rays (target layer) and dissipation of heat (anode block). The first function is an extremely inefficient process as shown by Equation (2) [37]:

$$P = \propto I_t * Z * {V_t}^2 \quad (2)$$

where P is the total X-ray power, I_t is the tube current, Z is the proton number of the target, and V_t is the tube voltage. For diagnostic energies (50 keV - 150 keV) using tungsten as the target material (Z=74), the efficiency is less than 1% (Figure 2.3). The other 99% is either deposited in the focal spot as heat, or scattered back out into the vacuum and deposited elsewhere in the anode as heat (see Section 2.2.3.1).

2.2. HEAT MANAGEMENT IN DIAGNOSTIC X-RAY ANODES

Section 2.1.2 mentioned how the process of creating x-rays is quite inefficient, making the dissipation of heat in the anode the dominating factor for determining the x-ray tube output power[38].

2.2.1. Deposition of Electron Energy in the Anode. In order to understand the approaches for *how* the heat is *dissipated,* we must first find out *where* the heat is *deposited*. The incident electrons undergo many interactions during their journey through the anode. Primarily, energy loss in the beam occurs from the disturbance of the electron cloud in the target as it travels through the metal, slightly perturbing its trajectory. This relation is more or less linear and was studied using thin films[39]–[41]. Unfortunately, this concept does not take other forms of scattering into account, which significantly changes the energy-depth profile. The true trajectories of electrons are far more chaotic, as shown in

Figure 2.4. In most anodes, the electrons only penetrate several microns into the target, which is basically on the surface[42], [43].

2.2.2. Focal Spot. The focal spot is the area on the anode utilized as the source spot for radiographic projection onto the detector. From an image resolution standpoint, the ideal focal spot would be a point source, but this is obviously not practical. The focal spot does, however, need to be kept as small as possible. The determination of the focal spot size requires a compromise between image quality and anode power loading ability[36].

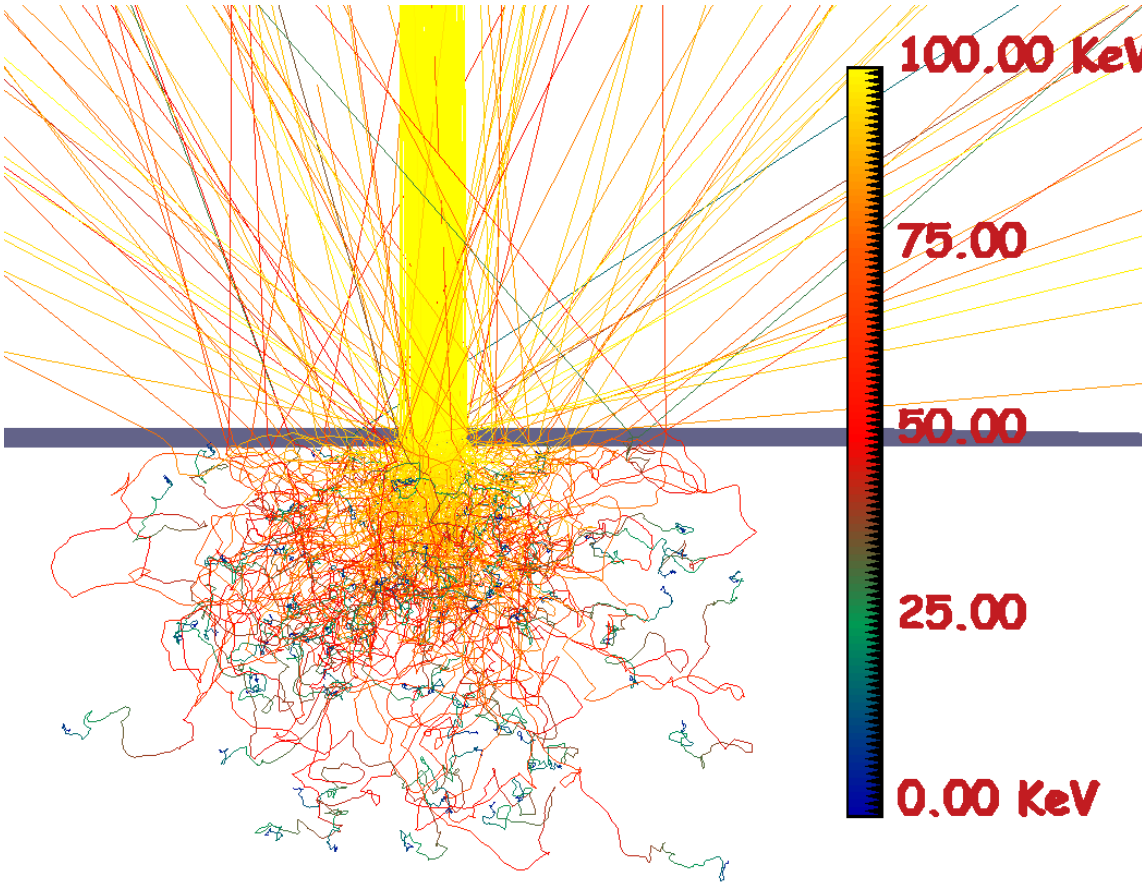

Figure 2.4 Monte Carlo simulation of a 1 μm diameter beam of 100 keV electrons interacting in an infinite tungsten layer. The color of the trajectories denotes the energy of the electrons. Notice that some of the electrons backscatter out of the anode with almost all of their original energy. Image made using CASINO [32].

As previously stated, around 99% of the energy from the electron beam is converted to heat. Since the heat is deposited in the first few microns of the target (See Section 2.2.1), the input heat rate (i.e. the maximum deposited power) will be limited by the target's ability to disperse the heat via conduction and the size of the focal spot. We can estimate the temperature rise ΔT in the focal spot of area A for pulses of short duration τ (less than about 0.05 seconds) using the following equation[44]:

$$\Delta T = \frac{2 * \Lambda}{A} \sqrt{\frac{\tau}{k \rho c_p \pi}} \tag{3}$$

where k is the thermal conductivity, ρ is the density, and c_p is the heat capacity for the target material. As mentioned earlier, the deposited power Λ is proportional to the x-ray output power. So, the design of the anode should find a way to maximize this value by manipulating the other variables in the equation (k, ρ, c_p, A, τ).

2.2.3. Electron Interaction Outside the Focal Spot. This section discusses the mechanisms that lead to bombardment by electrons outside the focal spot and how it can be alleviated.

2.2.3.1. Electron backscatter. Section 2.1.2 mentioned that some of the electrons backscatter out of the focal spot and deposit their energy outside the focal spot. As a matter of fact, for a 100 keV beam normally incident to a tungsten surface, approximately 50% of the primary electrons will scatter outside the focal spot carrying almost 40% of the original energy[37]. The values increase sharply as the incident angles increase and as Z increases[45], [46]. The backscattered electron trajectories and their energies can be seen in Figure 2.4.

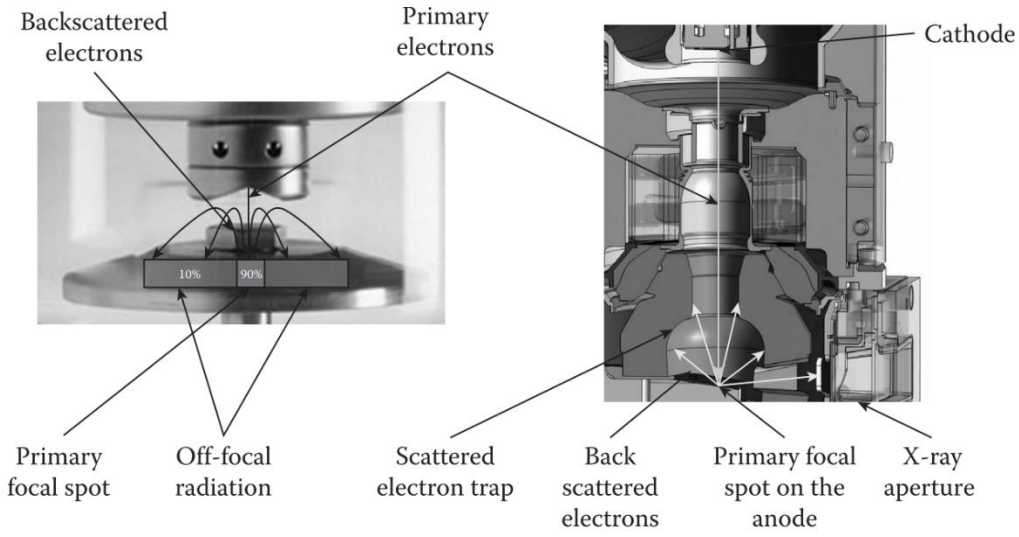

Figure 2.5 a) Off-focal radiation caused by small interelectrode distance b) Philips iMRC utilizes an electron trap[37]

2.2.3.2. Off-focal radiation and electron trap. The fate of the electrons backscattered into the vacuum is largely determined by the design of the x-ray tube. For systems where the cathode is very close to the anode, the strong electric field causes the electrons to curve back to the anode and land outside the focal spot, creating heat and x-rays outside of the region (see Figure 2.5a). This is called off-focal radiation.

Off-focal radiation is undesirable for two reasons. First, it puts unnecessary heat back into the anode. Second, and more importantly, the x-rays it produces outside the focal spot negatively impact the image quality and increase patient exposure[36], [47]. This effect was found to increase when a magnetic field was placed so that the field lines run parallel to the beam axis[48].

An electron trap can help alleviate the problem by providing an alternative destination for the electrons to travel[49]. Placing the cathode further away from the anode decreases the strong field felt by the electrons as they exit the anode. The backscattered

electrons will then travel back towards the cathode direction. An electron trap made of low-Z material is placed close to the anode and the backscattered electrons deposit the energy there (See Figure 2.5b).

2.2.4. X-Ray Anode Designs. The design of the anode plays a large part in heat management. This section gives a brief summary of the different kinds of anodes and their methods of heat management.

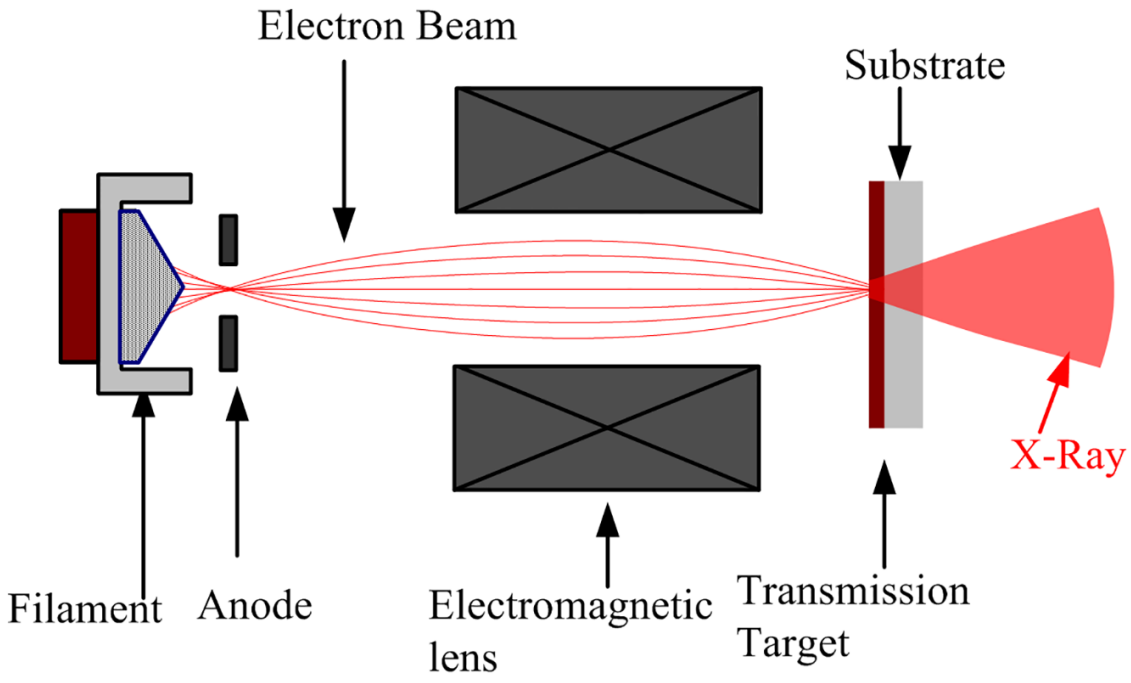

Figure 2.6 Transmission x-ray tube[50]

2.2.4.1. Transmission anodes. Figure 2.6 gives an example of an x-ray tube utilizing a transmission anode. The anode materials and dimensions are constructed in such a way that the x-rays produced in the target layer "transmit" through the anode. The trick here is to make the target layer thick enough that the x-ray production is maximized, yet

thin enough that those same x-rays don't get over-attenuated[51], [52]. The optimum thickness is energy dependent but the range doesn't vary by more than a few microns[53].

Innovations in this field typically rely on boosting the heat transfer properties of the substrate[53] or modifying the target to a point-like source[50]. The transmission anode has the benefit of being used in a compact environment[9], [10], [19]–[21], [54]–[56], but the "transmission" property means the surface area of the focal spot, A, must be kept small to maintain adequate spatial resolution for imaging purposes.

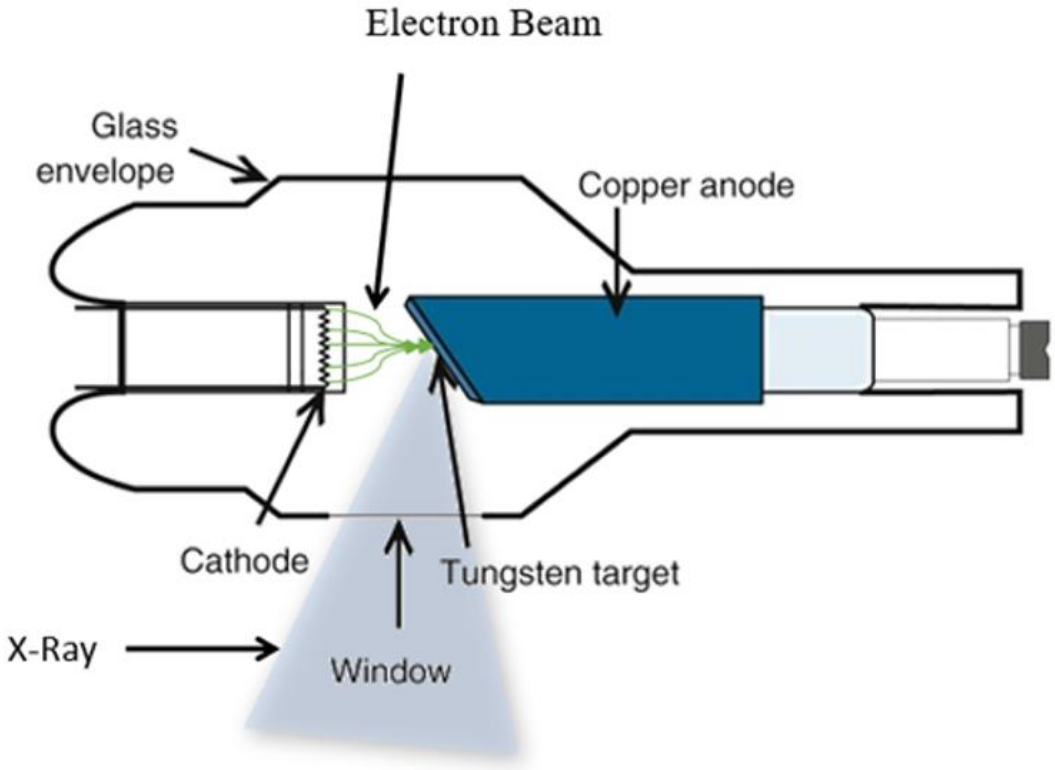

Figure 2.7 X-ray tube utilizing stationary angled anode

2.2.4.2. Stationary angled anodes. Figure 2.7 shows a stationary angled anode. A target layer (typically around 1 mm) is embedded in a copper anode block which carries

the heat away[36]. The tube powers in these designs are typically limited by the size of the focal spot and the heat capacity of the target, as thermal diffusivity of tungsten isn't high enough to carry the heat away from the target layer during operation. Long term thermal management is afforded by the high conductivity of the copper block, which dumps the heat into a reservoir outside the tube.

Stationary angled anodes take advantage of the principle of line focus[37]. Line focus allows the deposited beam area (called the thermal focal spot) to be elongated while still maintaining a small apparent focal spot when viewed from below (Figure 2.8). Referring back to Equation 3, this allows the maximum deposited power, Λ, to increase linearly with the increase in thermal focal spot length.

2.2.4.3. Rotating angled anodes. The advent of the rotating anode (shown in Figure 2.8) marked a huge step forward in x-ray tube technology. Not only did it utilize the line focus principle, but the rotating motion of the disk-shaped anode allowed for the heat to be spread over a much larger area during exposure. This increased the tube power by almost 50 times the stationary design[15]. The anode typically consists of a tungsten layer sintered onto a molybdenum alloy, such as TZM[57].

The long-term thermal behavior of the rotating anode is greatly dependent on the design of the rotor bearings. For traditional ball bearings, the contact surface is extremely small, leading to poor conduction efficiency. In these models, thermal radiation is the dominant form of heat transfer. Other iterations have replaced the ball bearings with hydrodynamic bearings, which significantly increases the thermal conductivity, allowing for better overall performance[58]–[61].

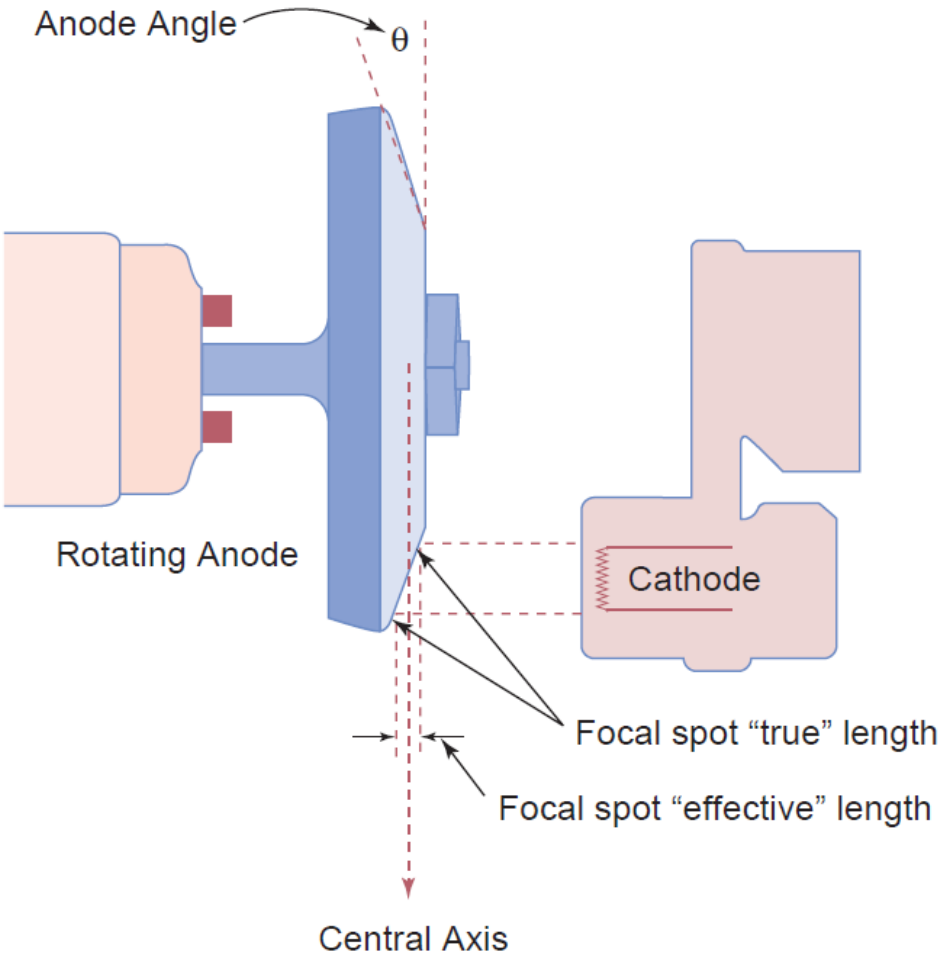

Figure 2.8 Rotating anode with line focus [36]

2.3. COMPUTED TOMOGRAPHY

Computed tomography (CT) is when three-dimensional radiographic data is acquired by taking projections from every angle and reconstructing them into slices. The speed at which these slices can to acquired is called its temporal resolution. Ideally, the temporal resolution would be fast enough to avoid blurring due to the motion of the imaging object. The following section summarizes the history of CT in regards to the advancement of temporal resolution.

2.3.1. First-Generation. The first-generation CT scanner was developed in 1967 by Godfrey N. Hounsfield, an engineer at the Central Research Laboratory of EMI, Ltd[3], [16]. A photo of the experimental setup is shown in Figure 2.9. The system consisted of an Americium source and sodium iodide detector with an imaging object between (in this case, a preserved brain)[62]. The source emitted a pencil beam which would travel through the imaging object and get detected by the detector on the other side. The source-detector pair would move incrementally along a specified plane (about 60 translational steps) until the entire imaging field had been covered. The imaging object would then be rotated slightly and the whole acquisition process would start again. This translate-rotate process was repeated until every angle of the imaging object was acquired (Figure 2.10a). Of course, acquisition time was extremely slow, taking around 9 days to acquire enough data for a single slice[62]. Obviously, this was too long to be used in a medical setting, but innovations soon followed that would fix that.

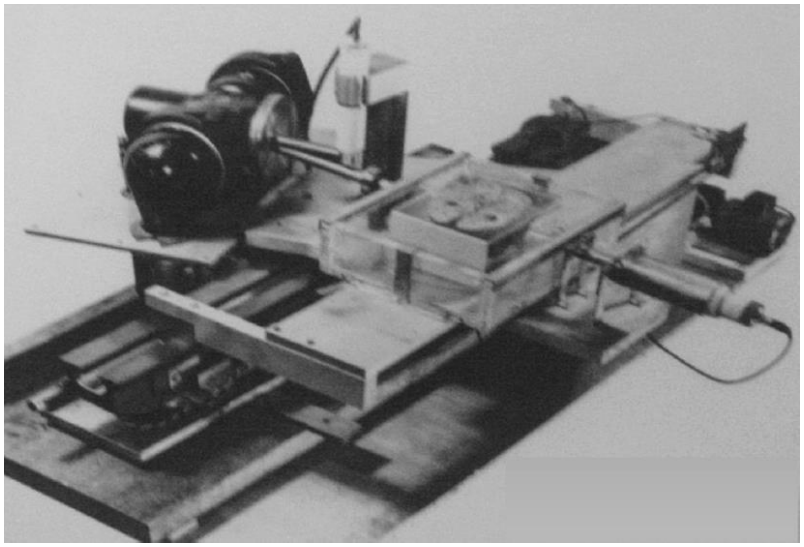

Figure 2.9 CT scanner setup of Hounsfield experiment at EMI laboratory[3]

2.3.2. Second-Generation. The second generation would introduce the fan-beam concept[3], [63]. The translational motion of the source-detector did not change, but the pencil beam was widened to a fan shape and the detector was elongated to accommodate the new beam geometry (Figure 2.10b). This allowed the number of translations to be reduced to 12. Acquisition time for the second generation took about 5 minutes, which was just short enough for certain medical applications.

2.3.3. Third-Generation. Translational motion was discarded altogether in the third generation (Figure 2.10c). Instead, this iteration utilized a source-detector pair rotating around a gantry. The invention of the slip ring was crucial to this design, allowing the power and communication cables to be completely removed from the x-ray source and detector[3], [64]. Cutting edge versions of this generation can acquire a slice in fractions of a second[18].

2.3.4. Fourth-Generation. Fourth generation (Figure 2.10d) was created to alleviate some of the perceived problems with third generation such as the sampling limitation. The third generation had a fixed detector location relative to the source, meaning that the spatial sampling is dependent on pixel size and pitch. The fourth generation fixed that problem by disjoining the traditional source-detector relationship. The source moved independently from the detector, which is now a full detector ring. This created a sort of role reversal in the sampling, where each detector pixel collects information from the entire fan beam. On the downside, this also increased the noise from scatter since no feasible post-patient collimator could be used[64].

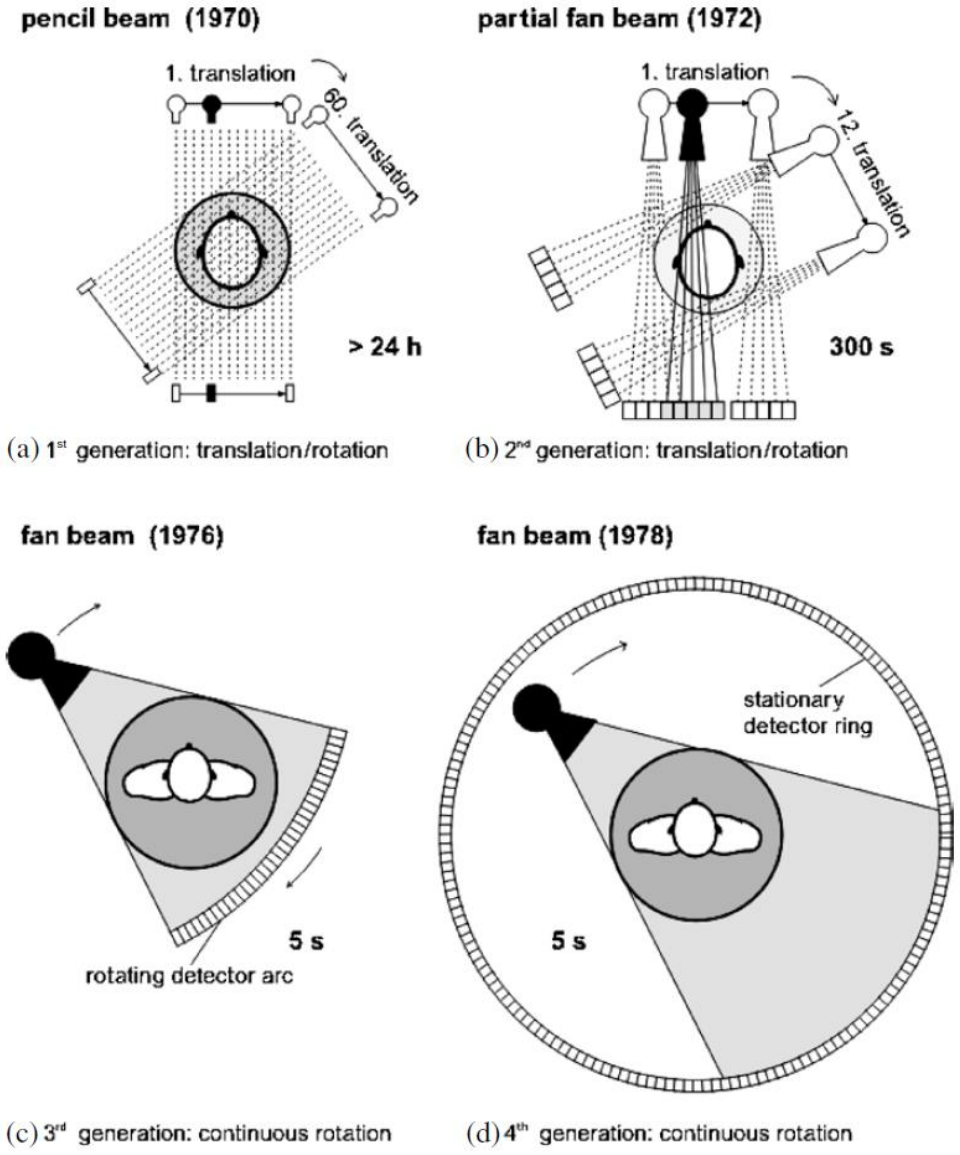

Figure 2.10 Generations of computed tomography scanners. a) First generation scanner with pencil beam source geometry. b) Second generation introduced the fan beam, allowing for much faster image acquisition times. c) Third generation used a rotational trajectory instead of the translational trajectories from previous generations. d) In an effort to improve temporal resolution, the fourth generation used a stationary detector ring and a rotating source[63].

2.3.5. Cardiac CT. Cardiac CT isn't exactly a generation of CT, but the technical requirements to be considered a "cardiac CT" definitely put it in a league of its own[18].

Applications that require the use of cardiac CT typically need two things: high tube power (decreases noise) and high temporal resolution (imaging a fast-moving object). Unfortunately, increasing the temporal resolution also increases the required tube power in order to maintain similar image quality[37].

Cardiac CT typically uses the third-generation architecture. Numerous advances have been made to incrementally improve image quality and acquisition speed[4], [65]–[67] but the weight of the gantry prevents any huge advancements in temporal resolution[7].

2.4. DISTRIBUTED SOURCE AND MULTISOURCE COMPUTED TOMOGRAPHY

One way to increase the temporal resolution of a CT system is to increase the number of sources. Remember that a 3-D slice requires projections to be taken from every angle. In a typical CT architecture, that means the source must be mechanically moved to each point. If the number of sources is increased, the distance each source has to travel is less, meaning the speed of movement can be reduced by the number of sources in order to maintain the same temporal resolution. Centrifugal force felt by a rotating object increases linearly with increases mass, but increases quadratically with increasing speed. So, for example, doubling the number of sources would roughly double the mass but halve the necessary rotation speed. This would then halve the centrifugal force felt by the gantry. Multisource, or distributed source, systems take advantage of this principle.

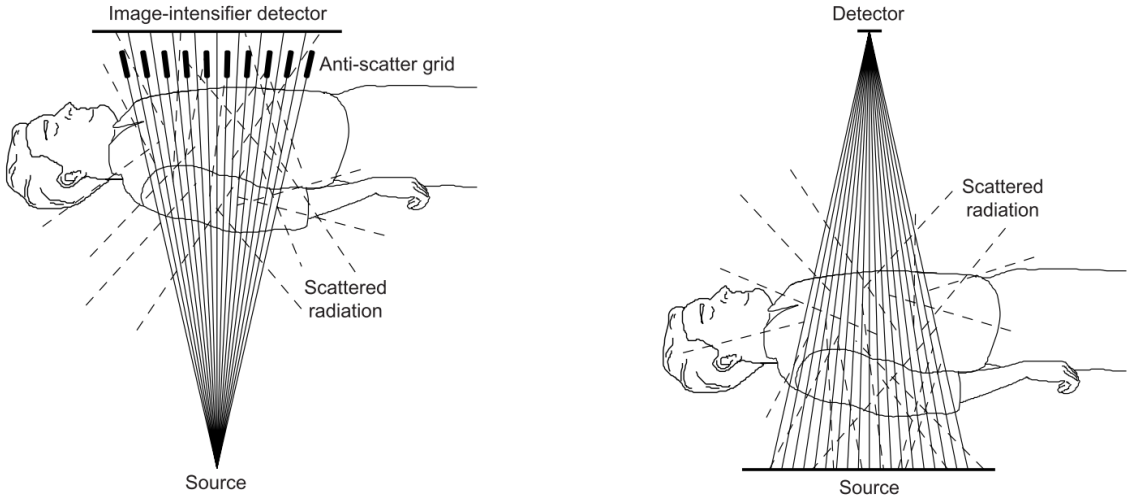

Figure 2.11 Intrinsic antiscatter properties of inverse geometry. (On the Left) Traditional x-ray setup with a single source and a detector array. Scatter from inside the imaging object causes decrease in image contrast. (On the Right) Inverse geometry uses a source array with a small detector area. Scatter from imaging object is significantly reduced[68].

2.4.1. Multisource X-Ray Systems. A multisource (or distributed source) x-ray system is an assembly that contains more than one x-ray source spot in a single module. They have the advantage of being able to form projections from multiple locations without mechanical movement[25]. A simple type would be a linear distributed source, where fast 3D data is acquired using tomosynthesis imaging[69], [70].

Multisource systems can also be used to form unique geometries such as inverse-geometry[9], [10]. Inherent to this layout is the significant decrease in scatter which can have a negative effect on image quality[68], [71] (Figure 2.11). Tetrahedron Beam CT (TBCT) expands on that concept by utilizing a source array and detector array positioned orthogonally. The resultant radiographic projection volume creates a tetrahedron shape. By rotating the system around the imaging object, 3D data similar to the traditional cone data

is formed, except scatter is again significantly reduced[12], [72], [73]. This design is meant to replace the cone beam CT used in image guided radiation therapy machines.

2.4.2. Multisource CT. There has also been interest in using multisource systems in diagnostic/interventional CT applications. Electron beam CT (EBCT), one of the first multisource systems to be used in a clinical setting, consisted of a single cathode emitting a high current electron beam that was magnetically swept along a semi-circle stationary anode target, similar to a cathode ray tube[29], [31] Figure 2.12). Temporal resolutions of between 33 ms and 100 ms were achievable, but it suffered from high scatter (a common problem for most stationary CT designs) and prohibitive costs[63].

Two forms of inverse geometry CT (IGCT) have been conceived. The first utilizes a rotating gantry system similar to third generation CT except the detector is much smaller and the single source is replaced with a source array[74], [75]. The second uses three modules with sweeping source beams projecting onto a small, rotating detector[11].

Research in stationary CT has seen a recent surge. A rectangular CT system was proposed for luggage CT[76]. This opened the door to non-circular CT design. A stationary CT for space applications was developed using a photocathode as the electron emitter[13]. A novel concept was investigated using an angled anode ring that took advantage of the thermal capacity of the tungsten target material by taking several, high-frequency projections of lower quality and combining them in post-processing to create a high-quality projection. This method allowed for a 1.3-fold increase in temporal resolution compared to conventional CT[14], [15]. Walker et al. demonstrated a modular multisource tube where multiple electron beams were magnetically swept along a long, stationary angled anode[16], [17], [77].

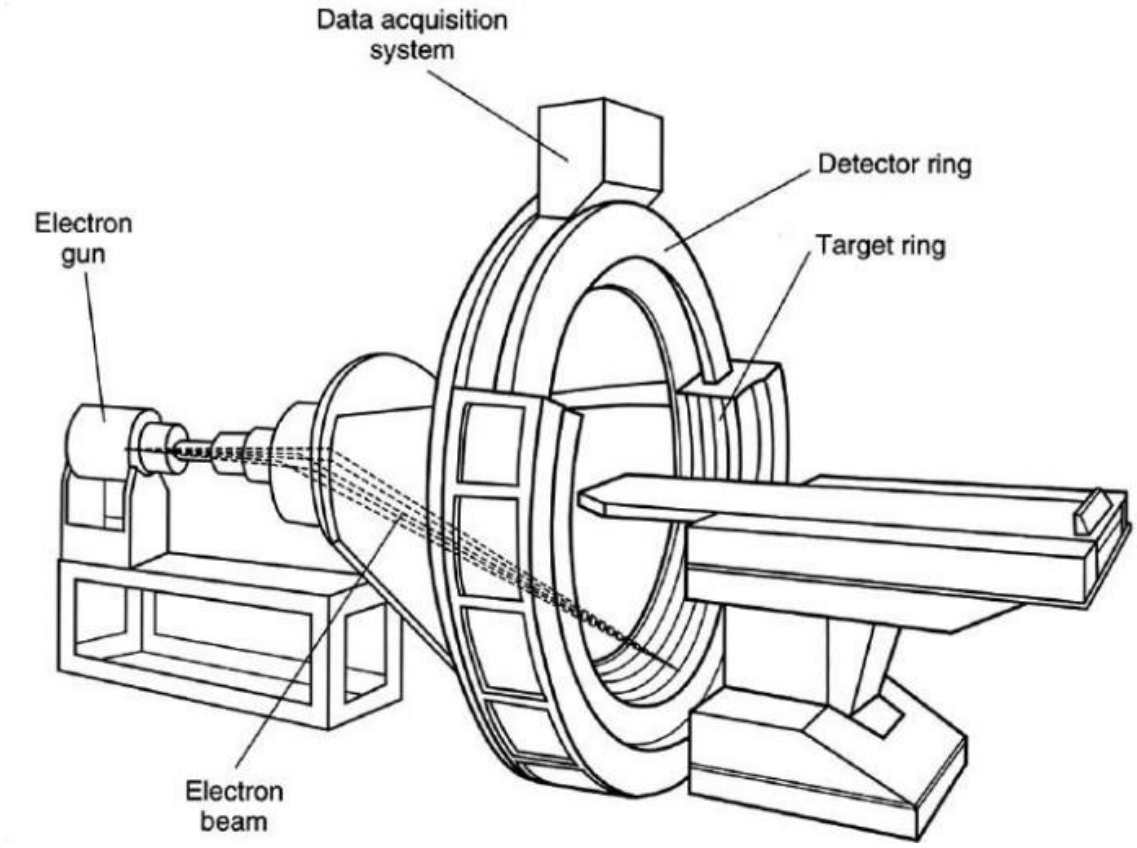

Figure 2.12 Electron beam CT [8]

3. TRANSMISSION TUBE SETUP AND SIMULATION

We first investigated a modular, linear x-ray tube with a transmission anode that could be placed radially around the gantry and sequentially pulsed for rapid image acquisition. We aimed for around 200 tubes, which meant each tube had to be as thin as possible in order to fit around the 1-meter diameter gantry. The electron emission, focusing, and targeting for the tubes are all designed to meet that need.

3.1. TUBE DESIGN

Figure 3.1 shows a schematic of the linear x-ray tube. The design consists of three major parts (cathode assembly, electrostatic lenses, and transmission target), described in the following sections. This design was used for an electron trajectory Particle-in-Cell (PIC) simulation and an electron deposition heat transfer simulation using COMSOL Multiphysics®[34].

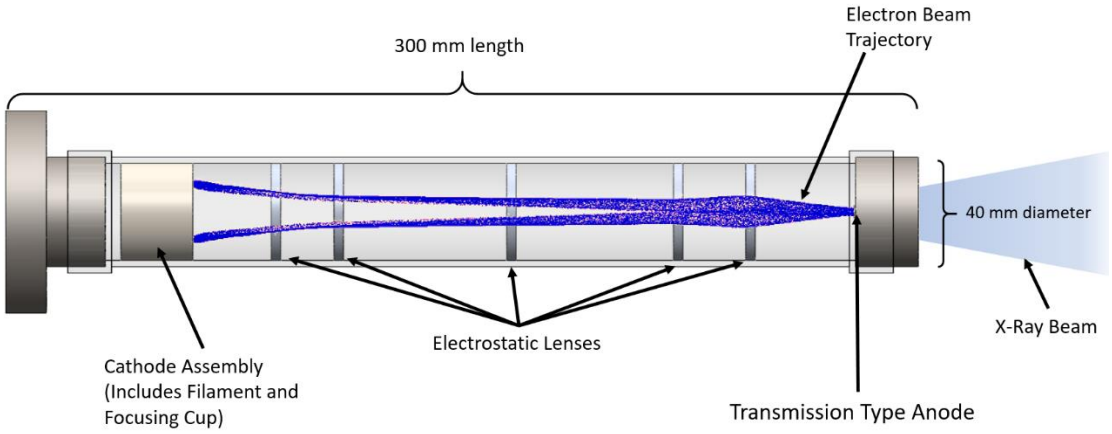

Figure 3.1 Schematic of linear x-ray tube

3.1.1. Cathode Assembly. A cathode assembly using a tungsten thermionic emitter was created to handle the high current needs of real-time CT.

3.1.1.1. Tungsten filament. Figure 3.2 shows a CAD model of the circular cathode assembly. It contains a focusing cup and a tungsten spiral filament. The circular pattern of the filament was used to take advantage of the relation between surface area and tube current as described by Richardson's Law of thermionic emission (Equation 1 of Literature Review).

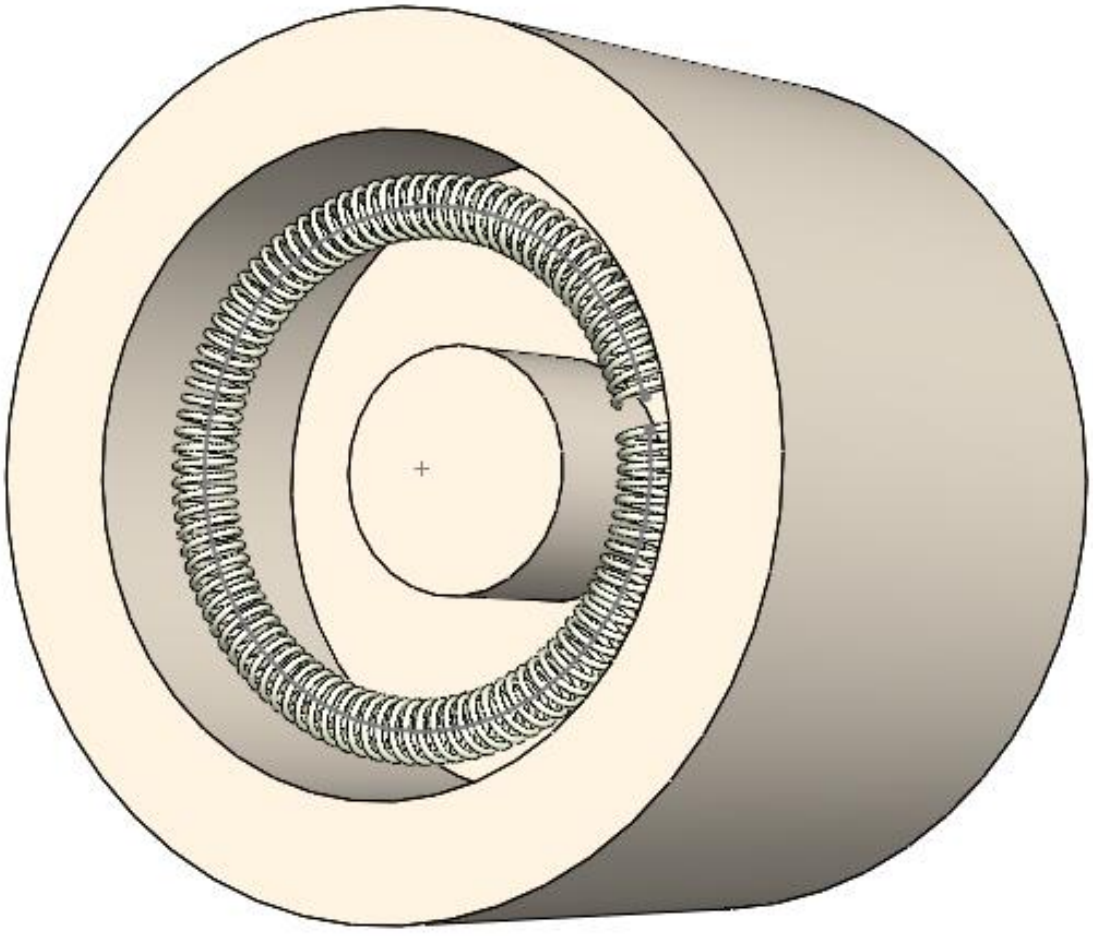

Figure 3.2 CAD model of cathode assembly

3.1.1.2. Focusing cup. Switching of the electron current from the tungsten filament can be controlled from the focusing cup by changing the electric potential. For our design, a focal cup potential of -4000 volts relative to the filament potential was sufficient to prevent the electrons from spilling out into the tube. Changing the cup potential to -100 volts allowed the electrons to be released and provided some focusing, as well.

3.1.2. Electrostatic Lenses. The length of the linear x-ray tube required the strategic use of electrostatic lenses for extraction and focusing. The following sub-sections talk about how the lenses were configured in the design.

a)

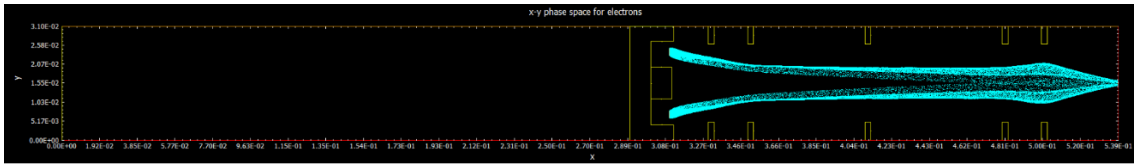

b)

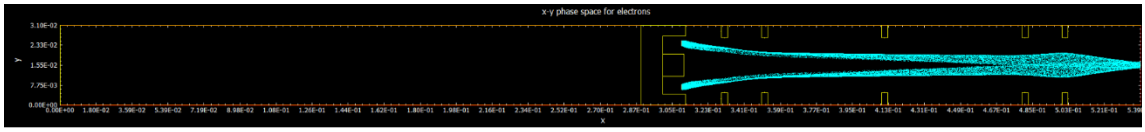

Figure 3.3 OOPIC output a) 60 kVp 500 mA b) 120 kVp 500 mA

3.1.2.1. Lens groups. The five lenses were split into three groups, each with a separate purpose. The first two lenses closest to the cathode were used as extraction lenses. Even with the large potential difference between cathode and anode (anode potential varied

from 60 kVp to 120 kVp), the distance prevented large tube currents from being efficiently focused. The extraction lenses created an initial electric field which prevented space charge effects from becoming an issue.

The length of the tube allowed for various currents and potentials to be used, but a longer travel distance means the electron beam will start to diverge. The third lens helped keep the electron beam focused. Finally, the last two lenses were the focusing lenses. Typically, the fourth lens was held at a potential almost as high as the anode, while the fifth lens was held at a potential much lower. This created a focusing effect, demonstrated in Figure 3.3.

3.1.2.2. Particle-In-Cell (PIC) simulation. A simulation for the electron trajectory of 60 kVp and 120 kVp potentials at 500 mA tube current was performed in OOPIC[78] to show the versatility of the linear x-ray tube. Figure 3.3 shows an output for the two simulations.

Figure 3.3a shows the output for 60 kVp. The focal spot width was measured using the built-in cursor and it came out to be 1.7 mm in diameter. The lens potentials were (starting from the left) 10 kV, 27.5 kV, 40 kV, 50 kV, and 6 kV. Figure 3.3b shows the output for 120 kVp. The focal spot width was measured to be 2 mm in diameter. The lens potentials were 20 kV, 55 kV, 73.5 kV, 100 kV, and 24 kV.

The above simulation supports the conclusion that the linear tube can be used for high-current, high-energy applications; at least from an electron trajectory standpoint. The next step would be to model the heat transfer in the transmission tube.

3.2. COMSOL SIMULATION

A transient thermal analysis simulation was performed on a compact, modular transmission-type x-ray tube anode operating in pulse-mode. The anode consisted of a tungsten layer with energy-dependent thickness deposited on a selection of three anode materials: beryllium, aluminum, and copper. Electron energy deposition depth profiles were created using CASINO for each combination of tungsten thickness and anode material. These material and energy dependent profiles were then used as depth-dependent heat inputs for COMSOL and compared with the traditional assumption of surface deposition for the proposed geometry. The transient thermal analysis was performed using 0.5 millisecond pulse widths from a cold starting condition (referred to as Single Pulse) and from a steady-state starting condition (referred to as Peak Pulse) to show how the maximum temperatures rise from the initial startup to long-term operation. The thickness of the anode was also varied in the heat transfer simulation to create an understanding of how the thickness correlated to maximum temperature. Finally, we performed an MCNP simulation to compare the relative spectrum filtration for each material.

3.2.1. Stationary CT Design. We assumed there were 201 transmission anodes[22] around the gantry, each inside a compact tube, firing around a ring making a complete “frame” (a stationary CT has no rotation by definition). The target temporal resolution was around 30 frames per second (real-time acquisition). Three sources were switched on simultaneously to reduce overheating in the anodes (Figure 3.4). This means that each x-ray “pulse” lasts for roughly 0.5 milliseconds.

3.2.2. Methods for COMSOL Simulation. The methods for the COMSOL simulation of the transmission x-ray anode are described in the following subsections.

3.2.2.1. Electron deposition. As the energetic electrons strike the anode target, around 99% of the energy will be "wasted" in the form of heat deposition in the anode, while the rest will generate x-rays to be used for imaging[3]. For a reflection-type anode, the tungsten target is relatively thick and the electron energy can be assumed to be deposited on the surface. That same assumption may not be true for a transmission type, due to the thinness of the tungsten layer required to avoid over-attenuation of x-ray spectrum. Because of this, electron deposition depth for each energy was found, and a comparison of surface heat deposition and volume heat deposition temperatures was conducted.

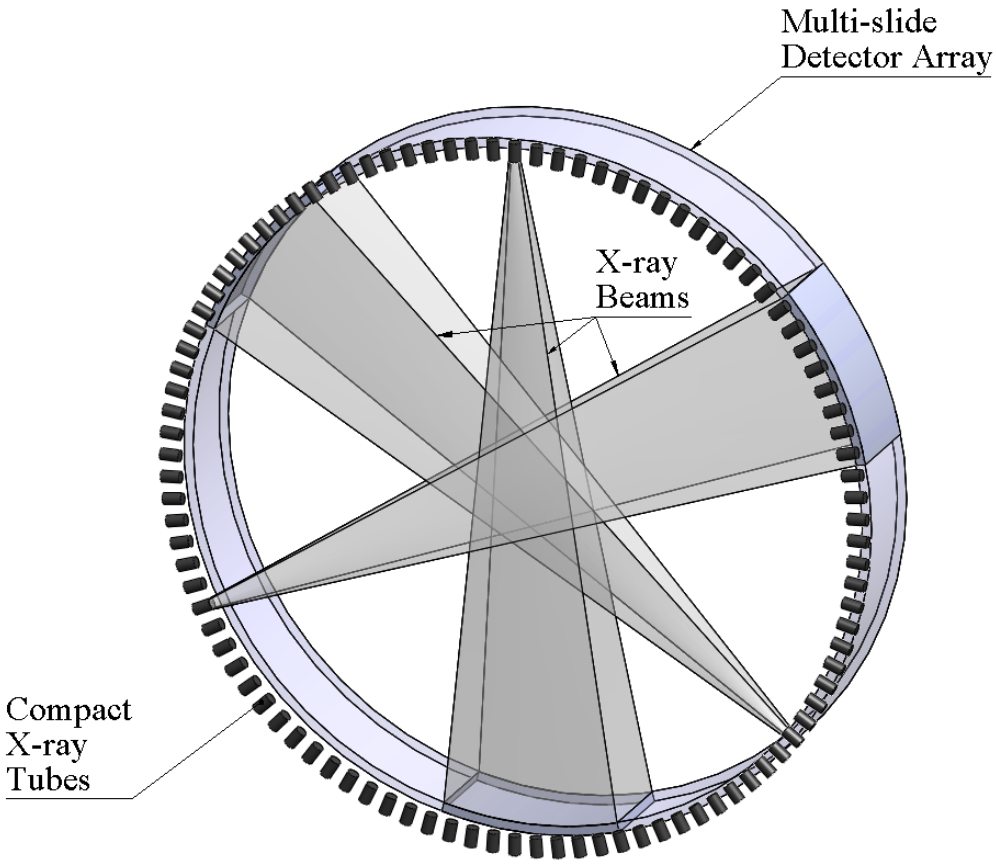

Figure 3.4 Schematic of stationary CT with 3 simultaneously firing projections

The optimum transmission thicknesses of the tungsten for each energy was estimated by the following equation from Nasseri[51]:

$$Y = -1.45 + 0.075X \quad (4)$$

where Y is the optimum tungsten thickness in μm and X is the incident electron energy in keV. From this equation the tungsten thicknesses for 30 keV, 60 keV, 100 keV, and 150 keV are 0.8 μm, 3.05 μm, 6.05 μm, and 9.8 μm, respectively. The volume heat deposition profiles were then found using the Monte Carlo electron simulation software, CASINO[32]. The comparison for surface heat deposition and volume heat deposition temperatures was made in COMSOL Multiphysics®[34].

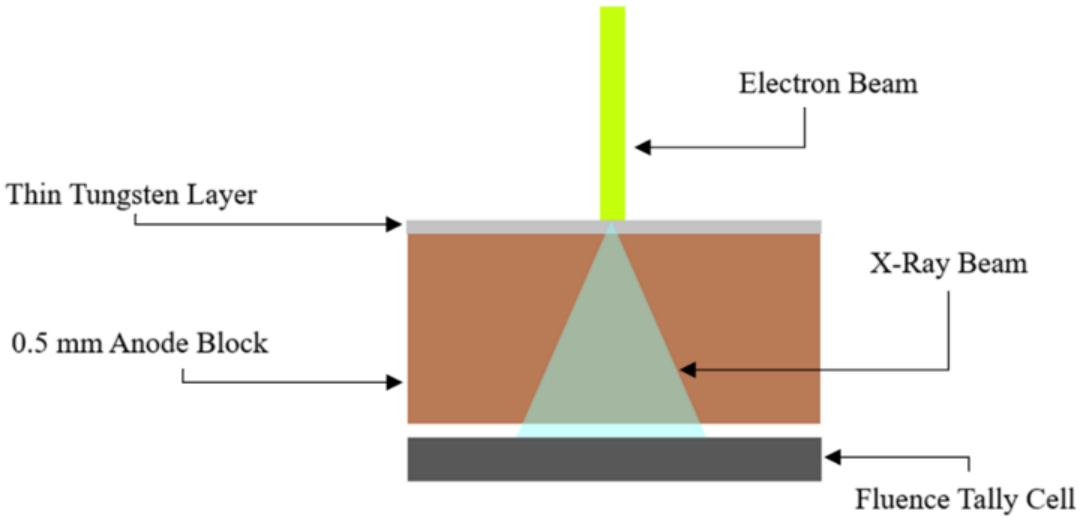

Figure 3.5 MCNP geometry for spectrum comparison of a 60 keV beam attenuated by 0.5 mm of beryllium, copper, or aluminum

3.2.2.2. Spectrum simulation in MCNP. A representation of the MCNP[33] cell geometry is shown in Figure 3.5. A 1 mm diameter, 60 keV electron beam bombarded a 3.05 μm thin tungsten layer, creating bremsstrahlung and characteristic x-rays. Those x-

rays attenuated through a 0.5 mm vacuum block cell and were tallied using an F2 surface tally to determine the x-ray spectrum yielded from the tungsten target interaction. Figure 3.5 represents the surface as a cell in order to visualize the placement of the virtual "detector". We then ran the same simulation three more times using beryllium, copper, and aluminum in place of the vacuum air block to find the relative x-ray attenuation for each material.

3.2.2.3. Modeling maximum temperature rise of anode. COMSOL Multiphysics® was used in the transient thermal analysis of a transmission-type anode being bombarded by electrons. Figure 3.6 shows a schematic for the input geometry. The part of the compact tube being studied is shown in the top right. Temperature-dependent thermal conductivities, heat capacities, and densities were used for tungsten, copper, beryllium, and aluminum[79]–[84]. Stainless steel and glass did not have temperature dependent properties.

A boundary condition was placed on the outer surface of the glass housing to approximate cooling by natural convection of a tube in room temperature transformer oil, a simplification that COMSOL offers. The outer surfaces of the molybdenum collimator also had a natural convection boundary condition using room temperature air. The inside surfaces of the tube were allowed to cool using radiative heat transfer. All other surfaces were adiabatic.

For the single pulse simulation, all components were initially at 20° Celsius. A 0.5 millisecond heat flux was turned on to represent electron bombardment of the tungsten layer. Temperature probes were placed in the tungsten layer and the anode block to record the maximum temperature during and shortly after the pulse. The same simulation was ran

again using steady-state initial conditions to represent the maximum temperature of the anode after long-term operation. This was called the peak pulse.

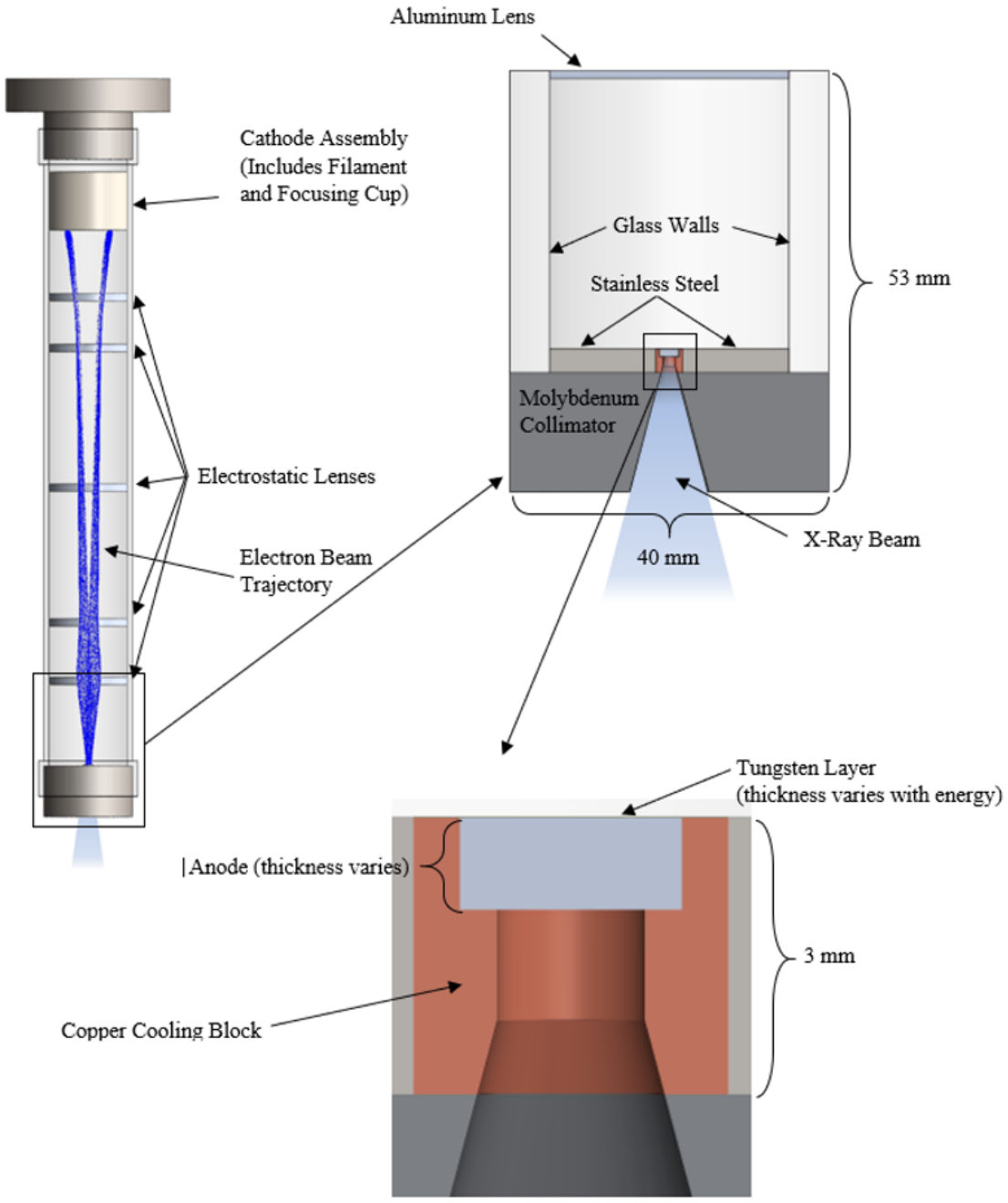

Figure 3.6 A detailed schematic of the geometry of the transmission-type anode

Various parameters were changed for each iteration. The electron energies used were 30 keV, 60 keV, 100 keV, and 150 keV. The tube current parameters were 0.5 mA, 3 mA, and 6 mA. The anode thickness parameters were 0.1 mm, 0.3 mm, 0.5 mm, 0.75 mm, 1 mm, and 2 mm. The anode block materials were copper, beryllium, and aluminum. Each iteration consisted of a combination of electron energy, tube current, anode thickness, and anode material. The simulations were ran until all combinations were found.

3.2.3. Results for COMSOL Simulation. The results for the linear transmission anode are summarized in the following sub-sections.

3.2.3.1. Electron deposition. Figure 3.7, Figure 3.8, and Figure 3.9 show the electron heat deposition profiles found from the CASINO simulations. The dotted vertical lines represent the interface between the tungsten layer and the anode material for each energy. Using these profiles as inputs for the heat flux (referred to as volume function), we compared the temperature pulses to uniform surface deposition.

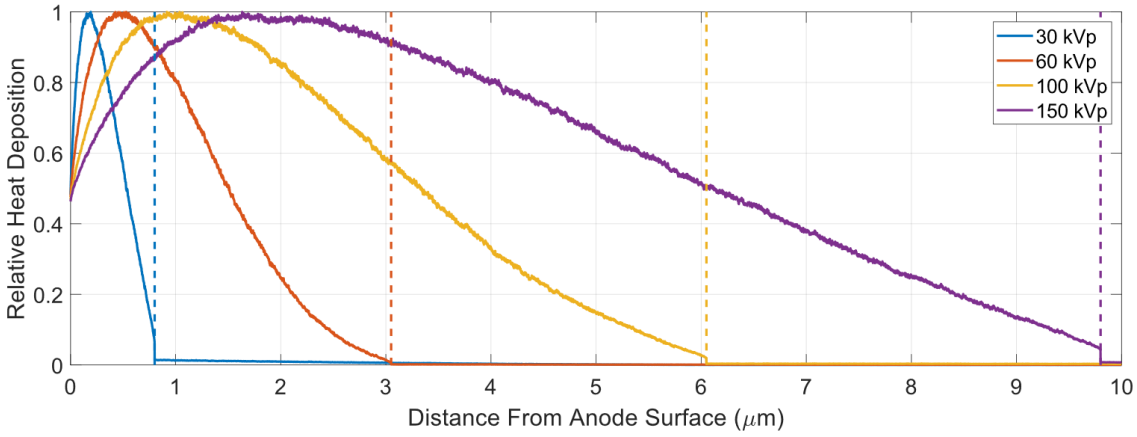

Figure 3.7 Electron heat deposition in tungsten with aluminum anode

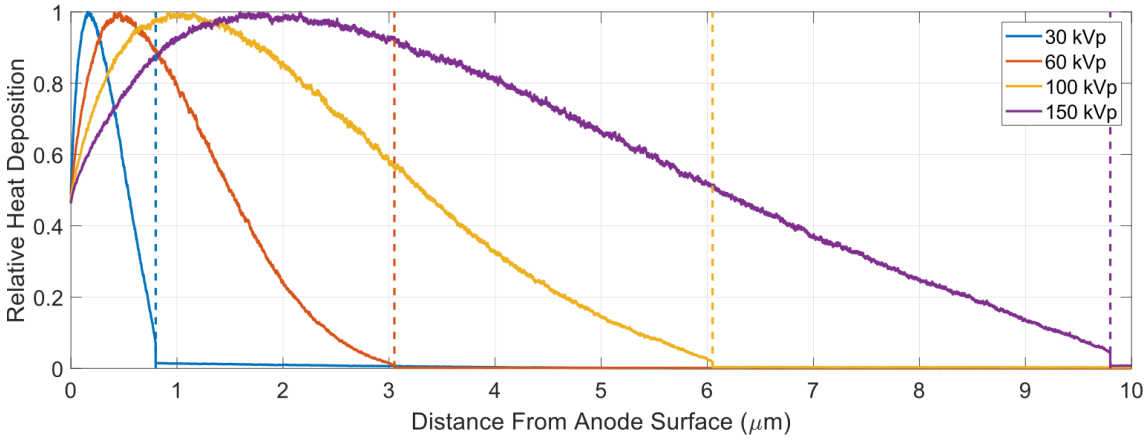

Figure 3.8 Electron heat deposition in tungsten with beryllium anode

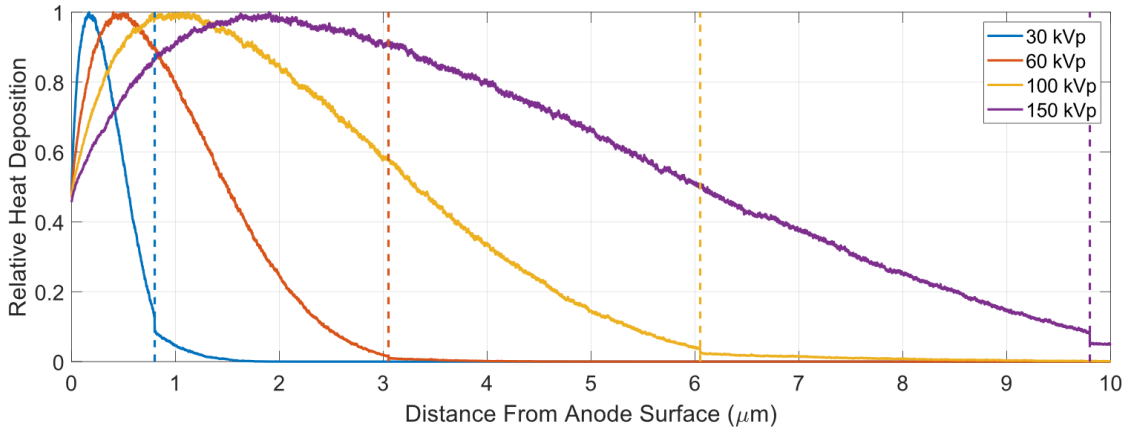

Figure 3.9 Electron heat deposition in tungsten with copper anode

3.2.3.2. Maximum temperature rise of anode. Figure 3.10 shows the temperature pulse profiles from both cases. The difference in the maximum element temperature for the two simulations was 0.0196%. The conclusion is that surface heat approximation is still valid for thin tungsten layers that are optimized to their respective energy.

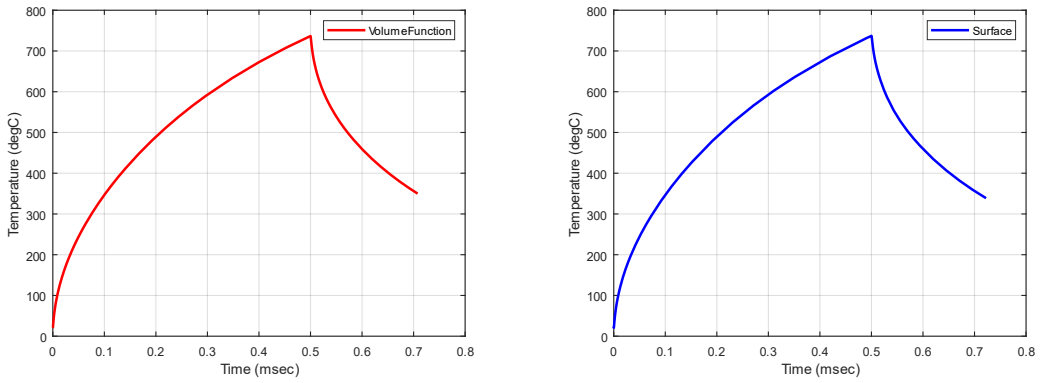

Max Element Size: 3.8e-7 m
Min Element Size: 7.6e-10 m
Run Time: 11 minutes, 36 seconds

Max Element Size: 3.8e-4 m
Min Element Size: 7.6e-7 m
Run Time: 36 seconds

Figure 3.10 Comparison study of pulses using volume function input and surface heat flux. The pulse is from a 150 keV electron beam and 6 mA tube current. The anode material is copper

Figure 3.11 shows the Single Pulse maximum element temperature for copper, aluminum, and beryllium being bombarded by a 0.5 millisecond pulse of 30 keV, 60 keV, 100 keV, and 150 keV electrons for varying block thicknesses and currents. From the values in Figure 3.11, it becomes clear that the maximum temperature starts to plateau for blocks greater than 0.5 mm thick, regardless of anode block material.

Figure 3.12 shows the peak pulse temperature for the same configuration as shown in Figure 3.11. As mentioned in the Methods section, the peak pulse is the pulse that comes after a steady-state solution. This represents the highest temperature that the anode will face for a certain beam power. Again, a temperature plateau forms around 0.5 mm anode thickness.

3.2.3.3. Temperature VS beam power. Utilizing the plateau effect of the anode temperature graphs, Figure 3.13 shows the relationship between deposited beam power (keV*mA) and maximum element temperature of the anode blocks. The operational temperature range for each material is bounded by the single pulse and peak pulse lines. The shaded area between those lines give transition temperatures for the anode during operation. The vertical dotted lines give a beam power maximum that each material can handle.

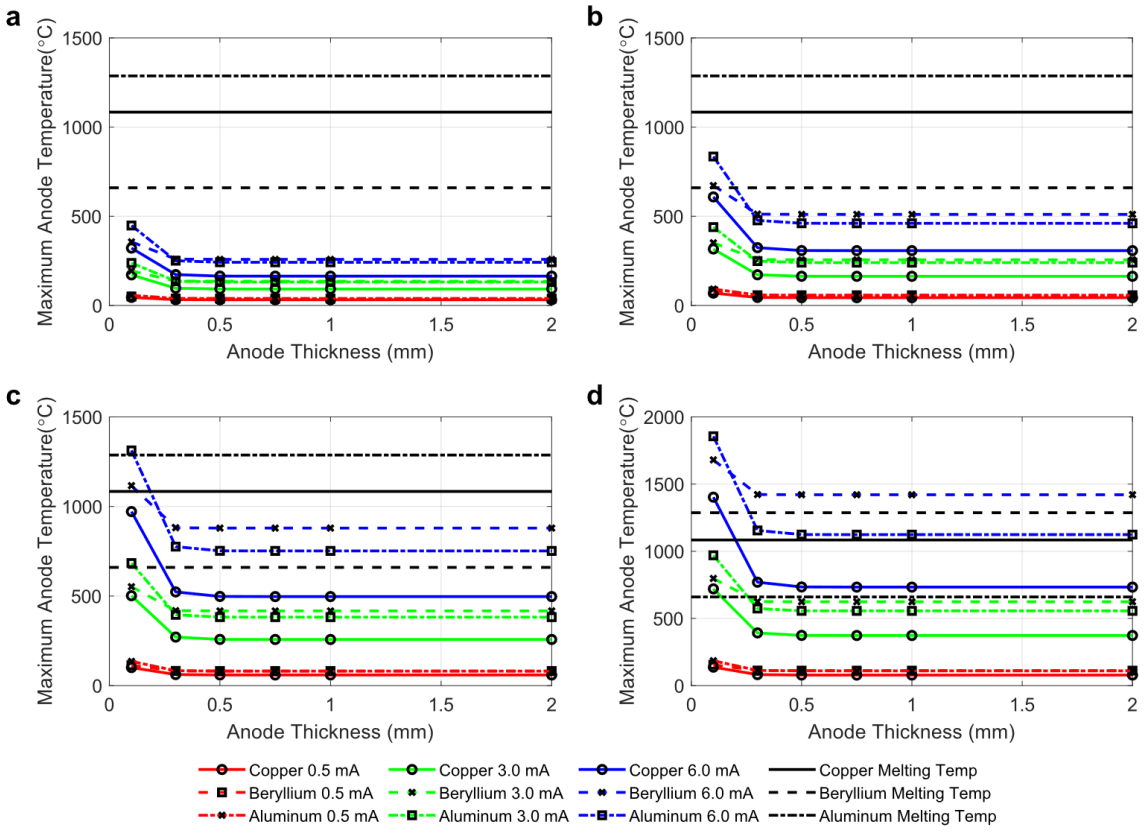

Figure 3.11 Maximum Single Pulse temperature for anode thicknesses between 0.05 mm and 2 mm for (a) 30 keV. (b) 60 keV. (c) 100 keV. (d) 150 keV

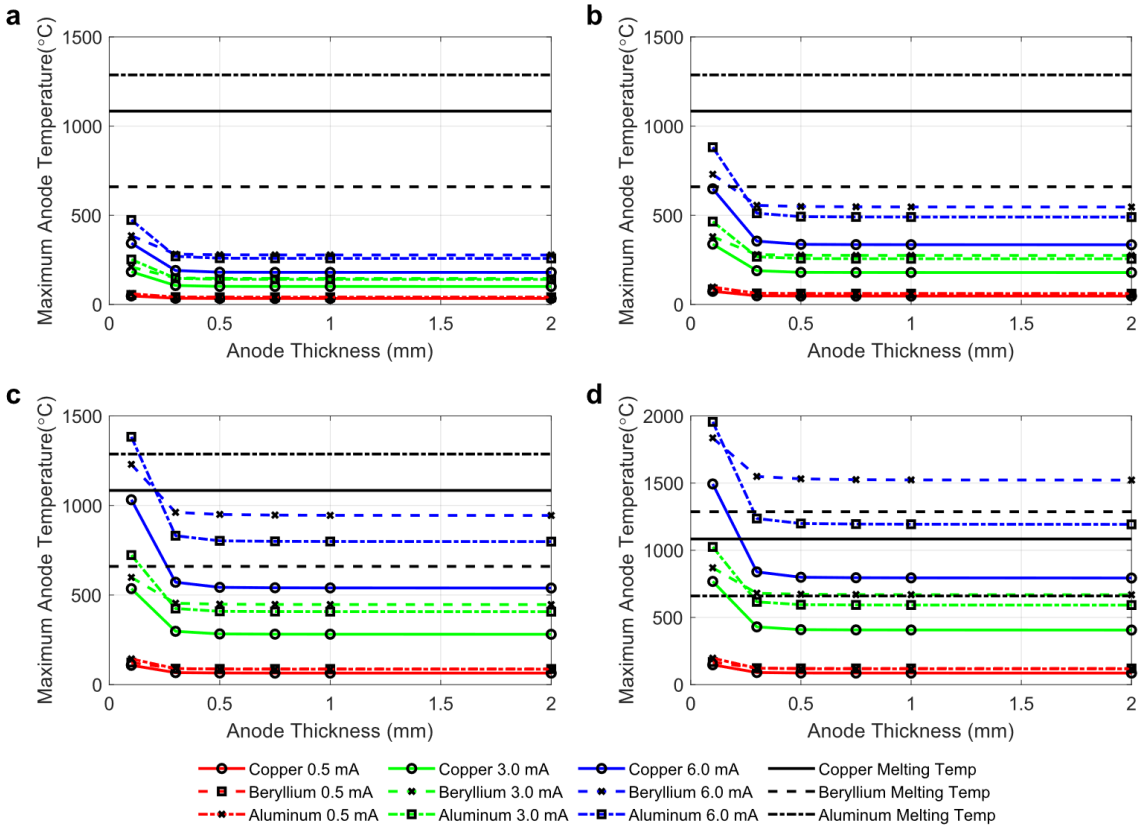

Figure 3.12 Maximum Peak Pulse temperature for anode thicknesses between 0.05 mm and 2 mm for (a) 30 keV. (b) 60 keV. (c) 100 keV. (d) 150 keV

3.2.3.4. Spectrum. Figure 3.14 shows how much copper and aluminum will attenuate the original spectrum when compared with beryllium. The 0.5 mm of aluminum filtered out about 53% of the photons while copper filtered almost 97% of the photons. The beryllium, however, only attenuated around 5.5% of the photons. This difference becomes less dramatic as energy is increased, but for diagnostic energy ranges, the beryllium is significantly less attenuative. This, along with a high melting temperature and decent thermal conductivity, means that beryllium is better than copper and aluminum for anode material for diagnostic energies. At high energies, copper might be better suited for a filtering material depending on the desired spectrum.

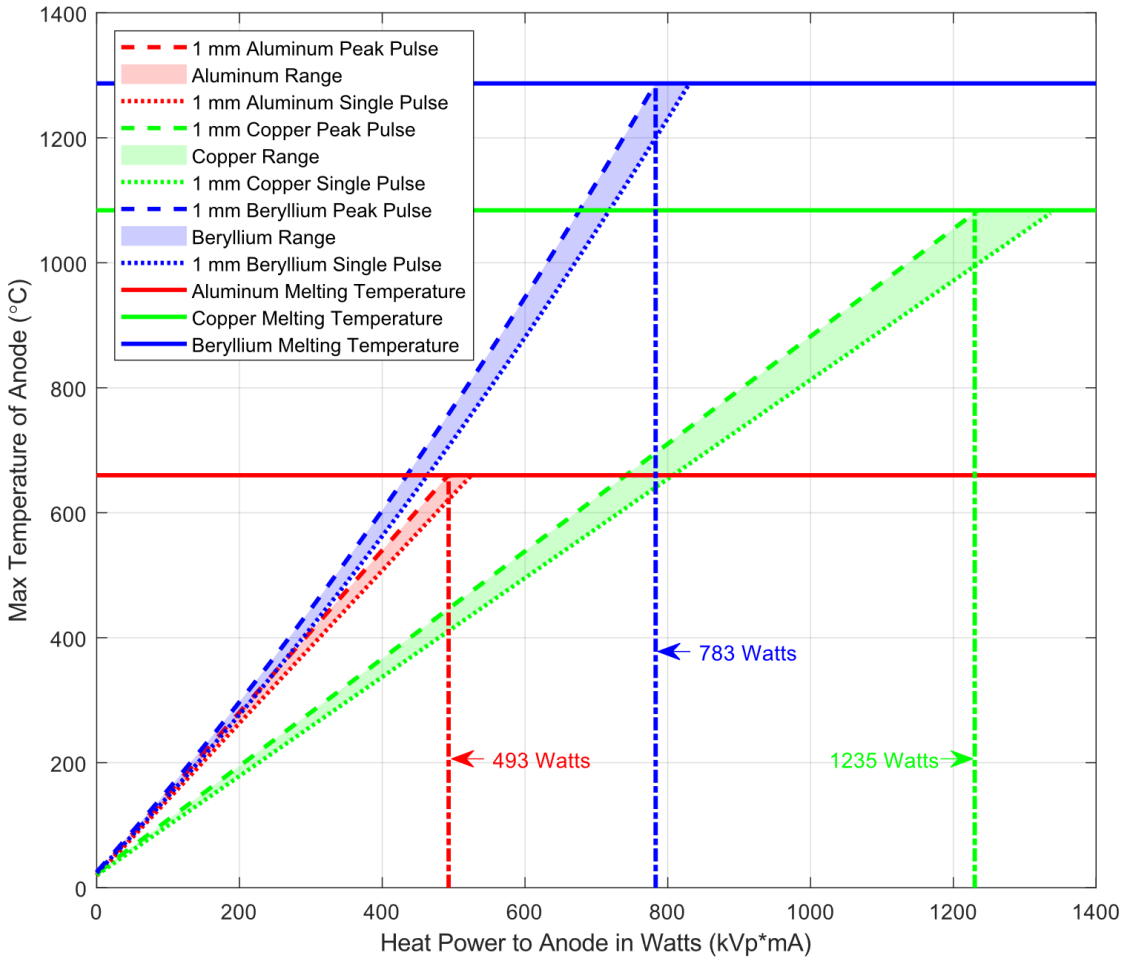

Figure 3.13 Relationship of beam power to maximum temperature in the anode

3.2.4. Summary of Findings. COMSOL, MCNP, and CASINO were used to simulate a compact, modular transmission-type x-ray tube anode operating in pulse-mode with varying thicknesses of copper, aluminum, and beryllium blocks. In comparison, the beryllium had adequate heat removal and a much lower x-ray attenuation, making it a better option in the electron energy ranges of 30 keV to 150 keV. The results showed a temperature plateau starting around 0.5 mm which would allow for future researchers to tune their anode to the spectrum they desire without worrying about significant variations in temperature. That plateau lasted even over long-term operation which is closer to real-

world application. From the data, a maximum beam power of 743 watts plus a reasonable margin of safety is recommended to prevent the beryllium anode from melting. Also, it was found that the surface deposition assumption for beam power is still valid, even for tungsten thicknesses in the micrometer range.

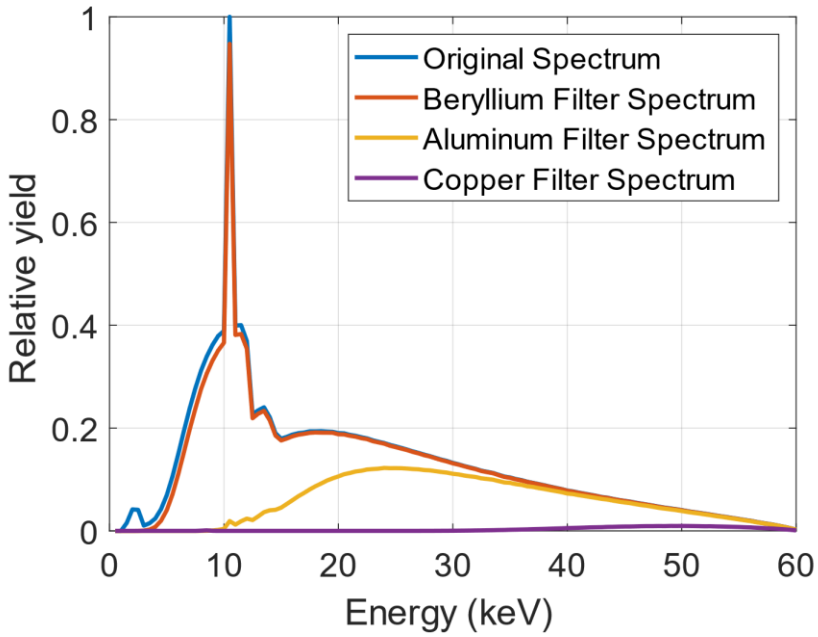

Figure 3.14 60 keV x-ray spectra comparison for 0.5 mm anode block. The blue spectrum is the original x-ray spectrum created in the forward direction from 60 keV electrons interacting with 3.05 μm of tungsten using MCNP

3.3. CYLINDRICAL ANODE

Since the goal of this research is to develop a real-time CT, the transmission type anode does not allow a high enough power to be used for this purpose. We then decided to change tactics and go with a rotating cylinder design. The rationale behind this is that a drum utilized in a multisource[16] could allow much higher beam power than previous attempts have been able to make.

4. COMPARISON OF ELECTRON BEAM SEQUENCES FOR ROTATING CYLINDER MULTISOURCE ANODE

The reduction of motion blur in cardiac CT drives the current research for multi-source CT. The rationale being that as the number of sources increase, the distance each source has to travel around the axis decreases. Reducing this source travel distance allows for faster acquisition of slice information. The obvious conclusion this leads to is to completely remove any source movement in the radial direction by creating a ring of x-ray sources, or multi-source x-ray modules. This would mean that the acquisition speed is completely dependent on how fast the machine can project x-rays from source points around the object, known as focal spots.

Attempts have been made to create such a system [14], [17], [76]. These lead to great advances in acquisition speed, but the general consensus is that the stationary anode arrays are not capable of handling the high beam powers that "real-time" CT (i.e. 30 frames per second) requires [8].

A rotating cylindrical multisource anode (shown in Figure 4.1) is proposed to break this barrier and allow for higher image quality at lightning fast acquisition speeds. The unique geometry also lets us study the effect of different sweeping sequences on image quality. Since the cylinder anode is rotating in a direction orthogonal to conventional CT tubes, multiple focal spots can be placed on a single anode, just as in the stationary multisource anodes, but the added benefit of rotation allows for a significant improvement in heat rate. Three beam sequences will be tested using this new geometry and compared with a traditional stationary reflection anode design.

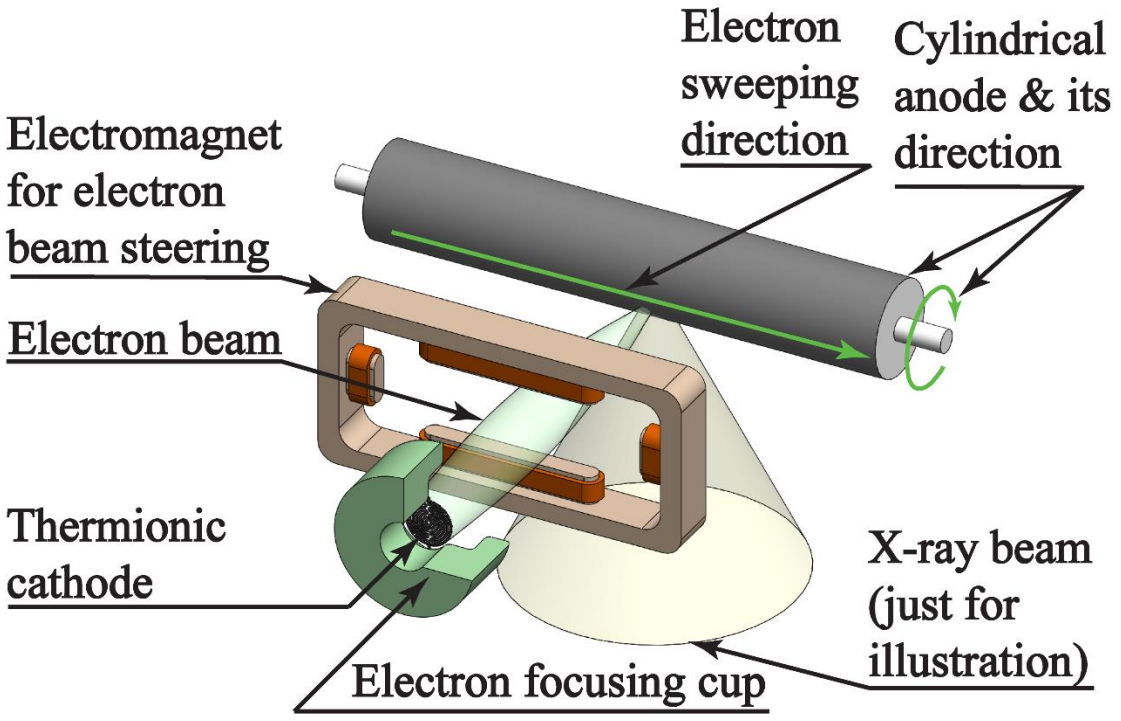

Figure 4.1 Rough schematic of cylinder CT array

4.1. METHODS FOR SWEEPING STUDY

Anode temperature rise was calculated using a form of the Oosterkamp equation [44], [85] modified for use in 2-dimensional electron beam sweeping. The results were then compared with COMSOL Multiphysics [34] simulations and maximum deposited powers for a focal spot temperature of 2600°C was found for the various beam sizes and sweeping speeds. These results were then used to compare the different beam sequences with a conventional stationary reflection multisource array.

4.1.1. Modifying the Oosterkamp Equation. A basic design for the cylindrical anode multisource x-ray system is shown in Figure 4.1. An electron beam is generated from a thermionic emission cathode, accelerated and focused onto a rotating cylindrical

anode radially encapsulated by a 1 mm layer of tungsten. The incident beam deposits its energy over a rectangular area of size W x L, where W is the beam width and L is the beam length. If the cylinder and the beam were stationary (cylinder is NOT rotating), the temperature rise ΔT of the beam impact area over short exposure time τ could be estimated by the Oosterkamp equation [44].

$$\Delta T = \frac{2\Lambda}{WL}\sqrt{\frac{\tau}{k\rho c_p \pi}} \tag{5}$$

where Λ is deposited power. k is the thermal conductivity, ρ is the density, and c_p is the heat capacity for the thin tungsten layer surrounding the cylinder at the starting temperature. The maximum temperature of the beam area is equal to the starting temperature plus the temperature rise. This equation is valid for very short exposure times (less than 0.005 seconds) with surface deposition onto a stationary target layer [85].

Equation 5 can be modified to estimate an electron beam that moves relative to the target surface by replacing τ with λ/V_λ, which will be referred to as temperature rise time. V_λ is the velocity of the beam relative to the target surface ($V_\lambda = \sqrt{V_L{}^2 + V_W{}^2}$). V_L is the further broken down into $V_L = V_{rot} + V_{Y\text{-}Sweep}$.

For a rotating cylinder, $V_{rot} = f\pi d$ where f is the rotational frequency in Hz, d is the cylinder diameter, and V_{rot} is the rotational surface speed which is in the direction of the beam length (y-direction from beam reference frame). $V_{Y\text{-}Sweep}$ is the beam sweeping speed in the y-direction, while V_W is the beam sweeping speed in the x-direction. λ is the maximum distance travelled through the original beam impact area measured collinear to

the direction of velocity V_λ (see Figure 4.2). The temperature rise for a beam with velocity V_λ relative to the anode surface now becomes

$$\Delta T_\lambda = \frac{2\Lambda}{WL}\sqrt{\frac{\lambda}{k\rho c_p \pi V_\lambda}} \tag{6}$$

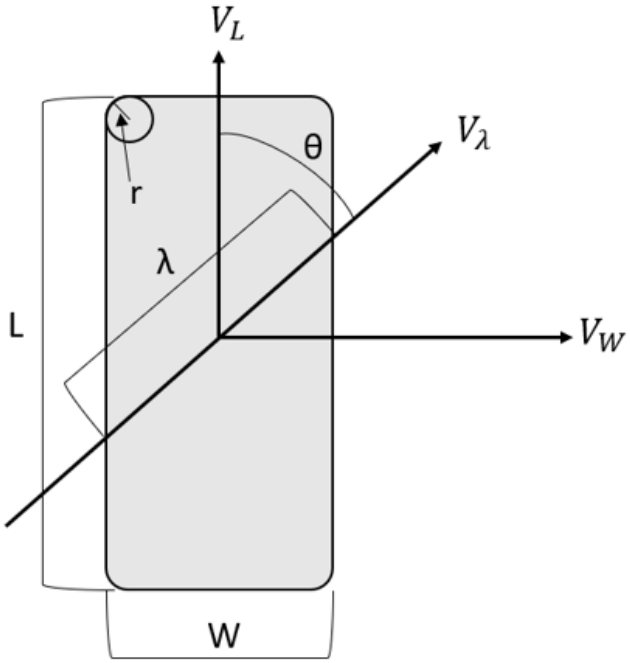

Figure 4.2 Visual representation of focal spot variables

The angular dependency of λ can be estimated for a rectangular beam area by treating it like a rounded rectangle with corners of very small radii (Figure 4.2**)**. In practice, the actual beam shape in an x-ray generator is rounded at the corners anyway [37]. For a rounded rectangle of sides W and L with corner radius r, the equation describing its perimeter is

$$\left(\frac{X}{a}\right)^{\frac{2a}{r}} + \left(\frac{Y}{b}\right)^{\frac{2b}{r}} = 1 \tag{7}$$

where $a = W/2$ and $b = L/2$. For this equation to adequately estimate a standard rectangle, the radius of the corners must be very small compared to the length of the sides. In the calculations, r was estimated to be equal to $a/25$ in order to avoid rounding errors. Also, for very small r, a/r behaves very similar to b/r, meaning that $2b/r$ and $2a/r$ can be replaced by another variable we can call z. Now, replacing X with $\lambda\cos(\theta)/2$ and Y with $\lambda\sin(\theta)/2$, the new equation for angular dependent λ is

$$\lambda = \frac{2ab}{\sqrt[z]{b^z \sin(\theta)^z + a^z \cos(\theta)^z}} \tag{8}$$

where $\theta = \tan^{-1}\frac{V_W}{V_L}$ and $z = 50$.

Equation 5 and equation 6 were used for the calculation of temperature rise for the three different beam sequences described below. For a given beam sequence and acquisition time, if the acquisition time is less than the temperature rise time (λ/V_λ), equation 5 will be used. For all else, equation 6 will be used.

A focal spot will be defined in the following sections as the total x-ray producing area that a detector will see during a single projection. It is shown in Figure 4.3 as the black outline. The red, rectangular region is the electron beam area. The electron beam area is the location of electron bombardment with the anode at any single point in time. To allow for a more intuitive grasp of the results of the simulation, RPM and anode diameter will be replaced with a singular concept: surface speed. Rotational surface speed is the vertical movement (denoted by the longer, vertical arrow in Figure 4.3) of the surface of the anode relative to the location of the beam area. Sweeping surface speed is the speed at which the beam is swept, either in the x or y-direction. This is denoted in Figure 4.3b and Figure 4.3c by the shorter lines pointing away from the beam area.

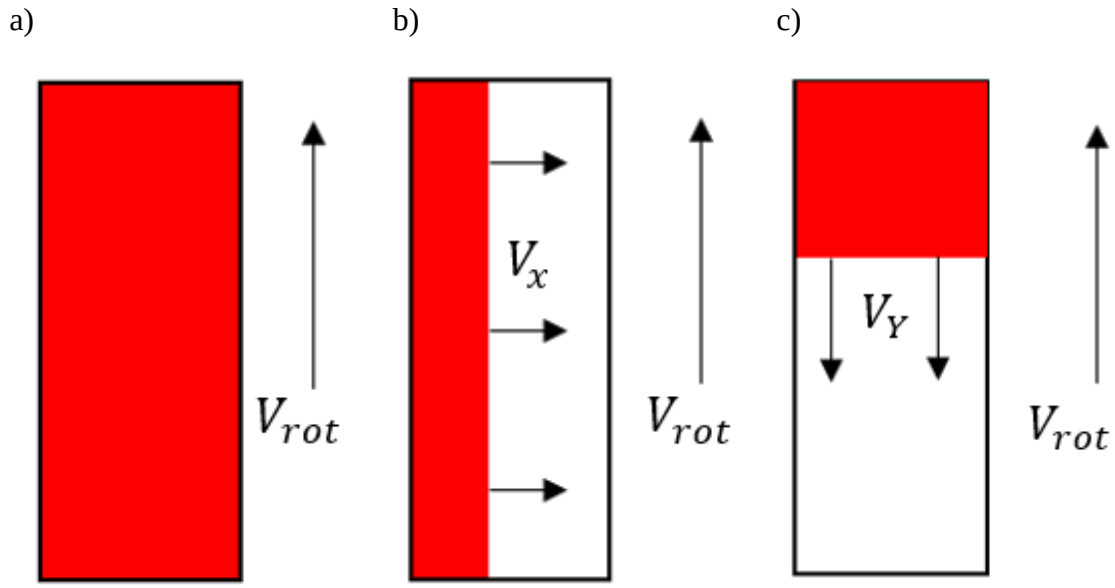

Figure 4.3 Different sequences being tested. The red represents the electron beam area while the black outline represents the focal spot area. a) Step-and-shoot b) X-sweeping c) Y-sweeping

4.1.2. COMSOL Simulations. COMSOL Multiphysics was used to find maximum temperatures of the focal spots for different scanning sequences. The maximum allowed temperature for the focal spot was 2600° C which is well below the melting point of the tungsten target material. The deposited power, Λ, that resulted in a maximum focal spot temperature of 2600°C was referred to as maximum deposited power. Three sequences were measured: Step-and-Shoot (Rotating Only) Figure 4.3a; Rotating with sweeping in the x-direction Figure 4.3b, and Rotating with sweeping in the y-direction Figure 4.3c.

To compare the different sequences with each other, total energy deposited during the acquisition time was also calculated. Around 99% of the energy from the bombarding electrons are converted into heat, with less than 1% converted to useful x-rays. X-ray production efficiency is dependent on the kinetic energy of the incoming electrons and the

material of the target [37]. Therefore, assuming both sequences have the same incident electron energy and target material (i.e. tungsten), the amount of x-ray energy being produced in the focal spot is directly proportional to the amount of heat deposited in that same focal spot. Increasing the quantity of x-rays produced per focal spot increases the signal-to-noise ratio of the image at the detector [86]**.**

To save computation time, a flat surface was simulated instead of the curved surface of a cylinder. The focal spot sizes were small enough that the curvature of the cylinder was negligible in regards to its effect on the heat transfer over very short time scales. The flat surface was a 1 mm thick tungsten slab. The width and length were dependent on the scanning sequence, beam dimensions, and focal spot dimensions. The width and length of the flat surface was equal to the total distance the beam travels in each direction plus 0.5 mm padding on each side to allow for the heat to spread laterally during acquisition time. All other boundaries were open to allow heat to flow out.

Tungsten's thermal conductivity, density, and heat capacity were independent of temperature. To simplify the results, electron backscattering was ignored and only the energy absorbed in the focal spot during the acquisition was simulated.

4.1.2.1. Step-and-shoot sequence. Rotating-Only Beam Sequence, aka Step-and-Shoot, refers to a sequence where the beam trajectory does not change during the acquisition of the focal spot area. The electrons are accelerated from the cathode and bombard a single focal spot on the anode during the entire acquisition. After the desired acquisition time has been met, the beam trajectory changes to the next focal spot. Throughout the acquisition, the apparent location of the beam area relative to the detector does not change due to the cylinder anode surface being the object that's moving and the

electron beam is stationary. This allows for longer beam exposures without significant temperature rise or focal spot blurring.

The simulation focused on the temperature rise in one focal spot starting from 20°C. The surface speed in the y-direction (rotational surface speed) was simulated at 0 m/s, 100 m/s, 200 m/s, and 300 m/s. 0 m/s rotational surface speed represented a scenario where a stationary anode was used instead of a rotating cylinder. The focal spot length was varied from 5 mm to 10 mm [37]. The focal spot width remained constant at 1 mm throughout the entire simulation. In the case of rotation-only beam sequence, the focal spot dimensions and the incident beam dimensions were the same. For these parameters, the maximum deposited power the focal spot can withstand without surpassing 2600°C was found.

For step-and-shoot mode, the total energy deposited was simply the maximum deposited power for a particular acquisition multiplied by the acquisition time, with the assumption the cylinder diameter was large enough that the beam always passed over a fresh target surface. The simulated acquisition time varied from 1 microsecond to 1 millisecond.

4.1.2.2. X-sweeping with rotation sequence. X-Direction Sweeping, shown in Figure 4.3b, refers to a sequence where the beam trajectory sweeps along a path colinear with the focal spot width and deposits its energy in the anode continuously. This sweeping of the electron beam typically is done using some form of shifting magnetic field. An example of this type of sequence was used in the electron beam CT [29].

In this sequence the beam width and the focal spot width are not the same, although the two lengths are identical. As the beam sweeps across the target, it passes across a location that will be used by the detector as the “focal spot”. For the simulation, the focal

spot was still 1 mm wide but the beam widths were simulated at 0.1 mm, 0.6 mm, and 0.9 mm. The acquisition time (τ) for a single focal spot was dependent on its beam width (W), sweeping speed (V_X), and focal spot width (FS_W) in the following way:

$$\tau = \frac{FS_W\text{-}W}{V_X} \tag{9}$$

The above equation assumes that the electron beam was already travelling at its sweeping speed across the surface of the target when the focal spot projection was taken. The acquisition time, as defined, started when the beam was completely inside the assigned focal spot area and ended when the beam has just touched the other edge of the same focal spot.

The maximum deposited power for sweeping speeds ranging from 0.05 m/s to 20 m/s was found. For each sweeping speed, the rotational surface speed was also varied at 0 m/s (stationary anode), 100 m/s, 200 m/s, and 300 m/s. The focal spot length will be kept constant at 7 mm.

The simulation for total energy deposited in the focal spot was ran so that the acquisition time, τ, was predefined, ranging from 1 microsecond to 1 millisecond. This meant that as the beam widths varied, the sweeping speeds were calculated using Equation 9. The total energy deposited in the focal spot could then be calculated using the product of the maximum deposited power for each beam width/ sweeping speed combination and the predefined acquisition time, τ.

4.1.2.3. Y-sweeping with rotation sequence. Figure 4.3c shows the sequence that was referred to as Y-Direction Sweeping. This is when the electron beam travels in the direction colinear to the focal spot length, stopping once it has covered the entire focal spot area. The beam is then moved to the top of the next focal spot location and the process is

repeated. The advantage of this is that the sweeping speed can be added to the rotational speed in order to improve surface temperatures.

Again, the beam and focal spot dimensions were not the same. The widths both remained at 1 mm but the length of the beam varied. The lengths of the beam simulated were 0.7 mm, 4.2 mm, and 6.3 mm, which was 10%, 60%, and 90% of the 7 mm focal spot length, respectively. Similar to X-Sweeping, the Y-Sweeping equation for acquisition time is:

$$\tau = \frac{FS_L\text{-}L}{V_Y} \tag{10}$$

where L is the beam length and V_Y is the sweeping speed in the y-direction. Y-direction sweeping is a special case of Equation 6, where the characteristic length, λ, is the beam length, L; and V_λ becomes the rotational surface speed, V_{rot}, added to V_Y.

The maximum deposited power for the Y-Sweeping speeds ranging from 0.05 m/s to 40 m/s was found. For each sweeping speed, the rotational surface speed was also simulated at 0 m/s (stationary anode), 100 m/s, 200 m/s, and 300 m/s. The calculations for total energy deposited in the focal spot were the same as for X-Sweeping, except the beam lengths were changed instead of the widths.

4.2. RESULTS FOR SWEEPING STUDY

The results for the beam sweeping sequences are given below. A description of the definitions of deposited power for each sequence are shown in order to fully understand the how the results were found.

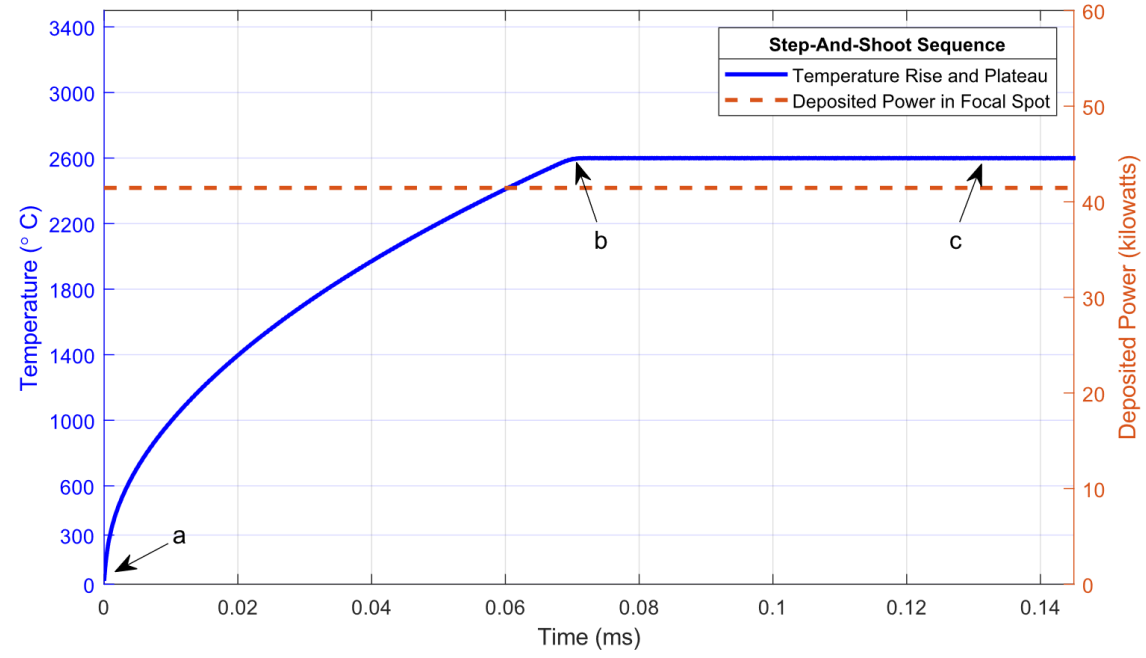

a b c

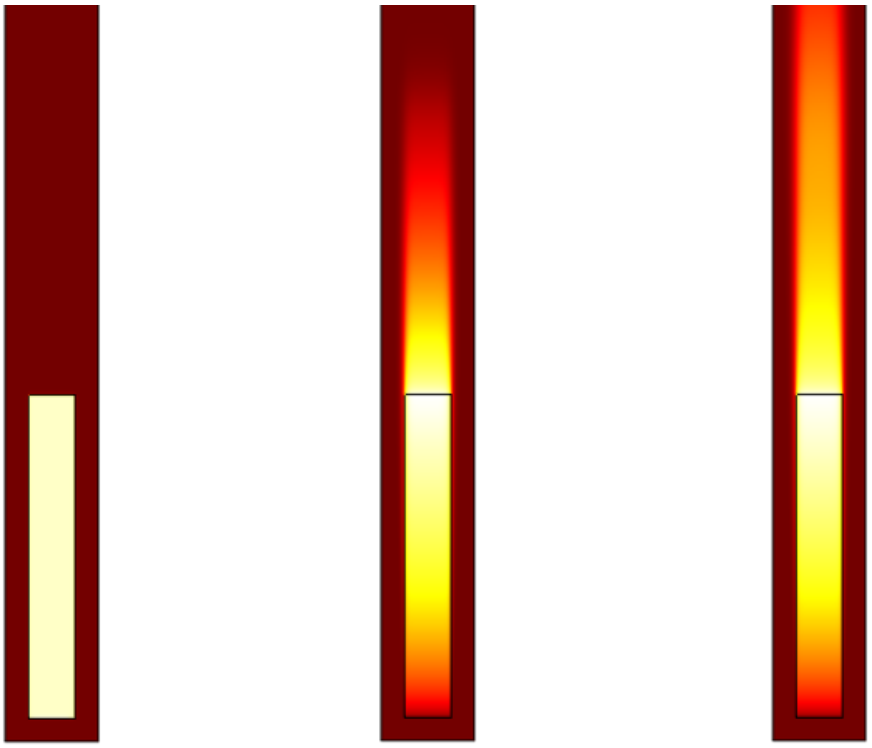

Figure 4.4 COMSOL simulation for step-and-shoot

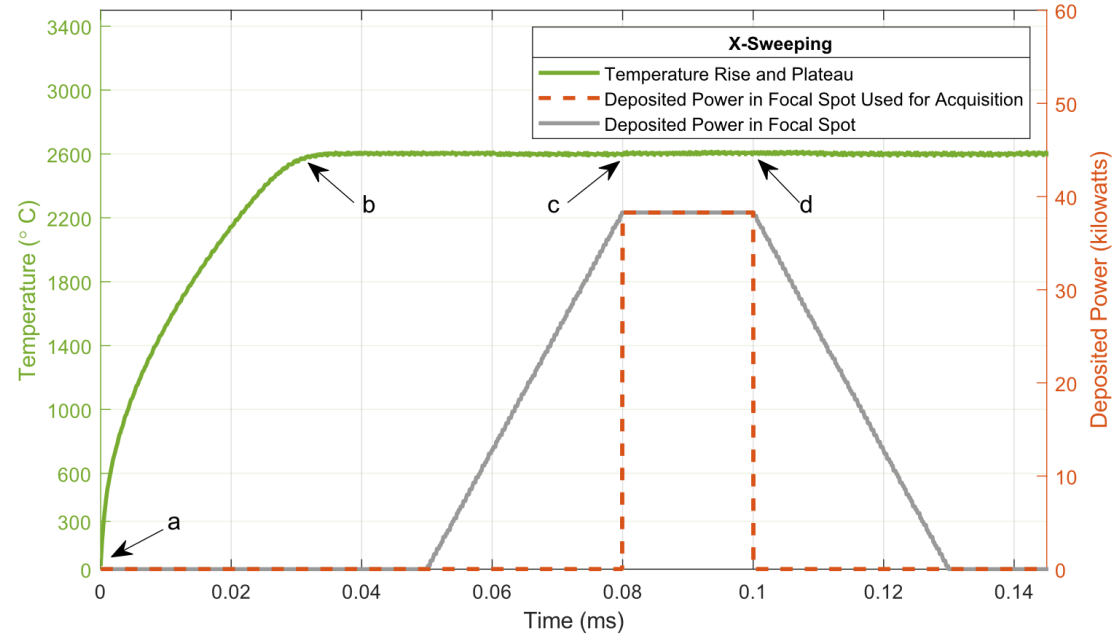

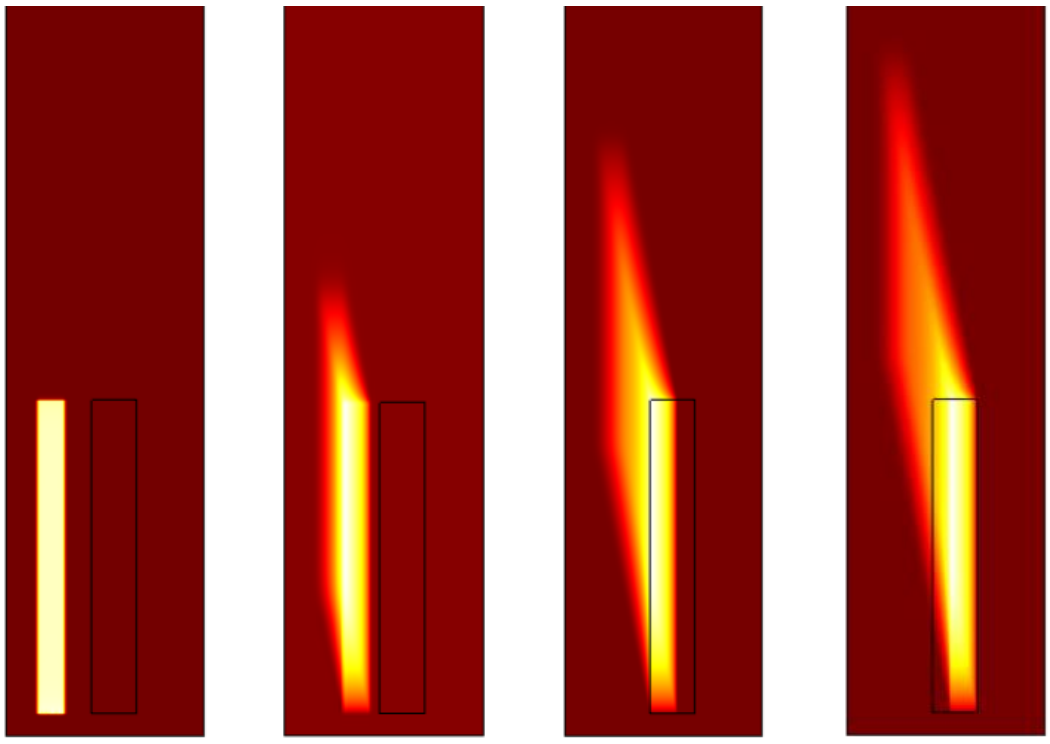

Figure 4.5 COMSOL simulation for X-Sweeping

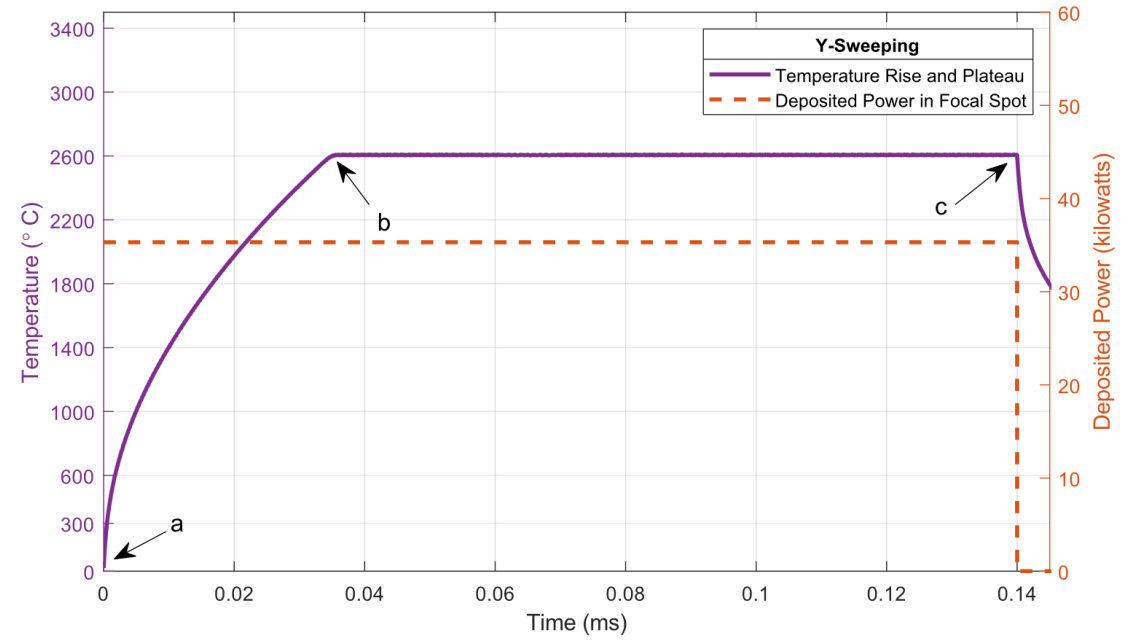

a b c

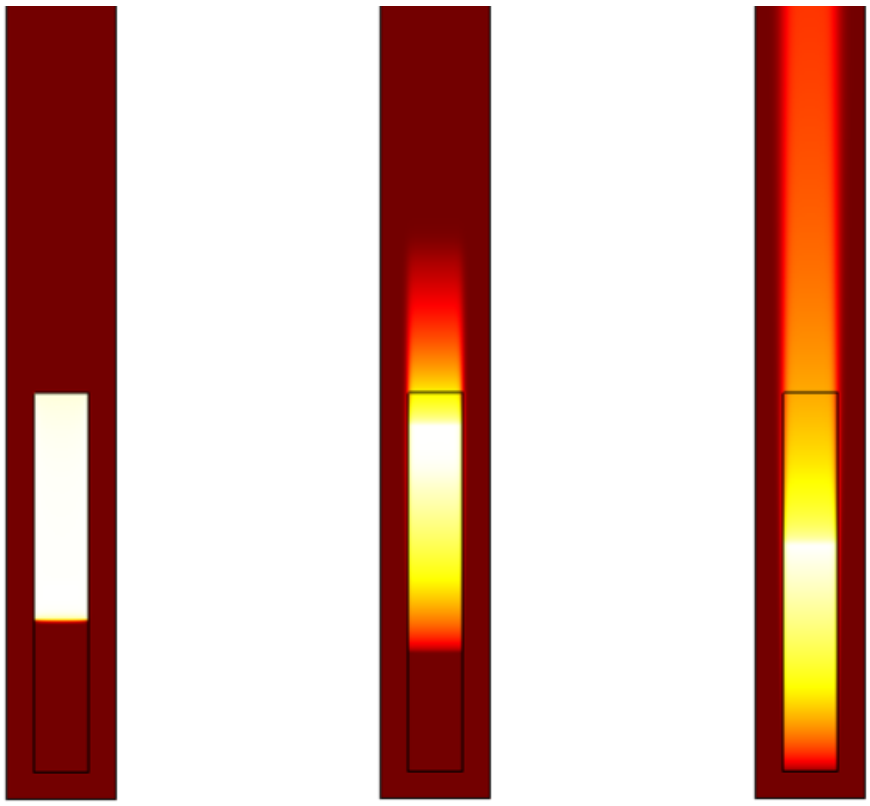

Figure 4.6 COMSOL simulation for Y-Sweeping

4.2.1. Pulse Shape and Deposited Power Definition for COMSOL Simulations.

Three different beam sequences were calculated using the modified Oosterkamp equation and verified using COMSOL. For all simulations, the focal spot area is 1 mm x 7 mm. Figure 4.4 shows an example of an output for a COMSOL simulation for a step-and-shoot sequence using a 1 mm x 7 mm beam area (same size as the focal spot area) with rotational surface speed of 100 m/s. Looking at the temperature profile, you can see the initial rise in temperature until a certain point where the beam has travelled in the anode reference frame a distance of one full beam length (Figure 4.4b). The amount of time it takes for this plateau to happen (referred to as $\Delta \boldsymbol{t_{rot}}$) is equal to the beam length divided by the rotational surface speed. The amount of energy deposited in the focal spot during acquisition time would be equal to the deposited power (equal to 41,449 W) times the length of the entire acquisition, which was 0.145 ms in this case.

A X-Sweeping beam sequence is shown in Figure 4.5. The beam area is 0.6 mm x 7 mm. The rotational surface speed is 100 m/s and the X-sweeping speed is 20 m/s. The initial location of the beam was intentionally placed outside the focal spot to represent the actual behavior of the temperature rise in the anode and the corresponding energy deposition in the focal spot area (Figure 4.5a). In this particular sequence, the electron beam begins sweeping across the surface of the anode and the corresponding temperature rise ensues. The amount of time it takes for temperature profile to reach the plateau region (referred to as $\Delta \boldsymbol{t_X}$) can be found by dividing the beam width by the X-sweeping speed, V_X. Instead of a sharp transition at time $\Delta \boldsymbol{t_X}$, it is rounded off (Figure 4.5b). This occurs because lateral heat dissipation cannot be ignored at that point, an assumption that does not follow with the Oosterkamp equation. Once the beam area is completely inside the focal spot, the

detector begins the image acquisition (Figure 4.5c) and ends it when the right edge of the beam has reached the other end (Figure 4.5d). The beam continues moving, depositing its energy as it goes to the next focal spot area. The gray line represents the actual energy deposited in the focal spot area, but the orange dotted line represents the energy deposited in the focal spot area during acquisition of the projection from that focal spot. As mentioned previously, the amount of x-ray energy being produced for a particular projection is proportional to the amount of energy being deposited in the focal spot during the acquisition time. In this case, the total amount of energy deposited in the focal spot is calculated by multiplying the deposited power (equal to 37,989 W) by the acquisition time, calculated by equation 9 (0.02 ms in this case).

The Y-Sweeping is the most complicated sequence between the three but it's meant to take advantage of the additive benefit of the rotational surface speed and the Y-directional sweeping speed. Figure 4.6a shows a 1 mm x 4.2 mm beam area sweeping in the negative y-direction with a speed of 20 m/s. The rotational surface speed of the target is 100 m/s. The beam area starts from the top of the focal spot and moves in a downward motion (Figure 4.6b). Temperature rise time, $\Delta \boldsymbol{t_Y}$, is equal to the beam length divided by $\boldsymbol{(V_{rot} + V_Y)}$. After the beam reaches the bottom of the focal spot (Figure 4.6c), the beam is turned off and moves on to the next focal spot. The total energy deposited in the focal spot is the deposited power (equal to 35,307 W for this case) multiplied by the acquisition time, which can be calculated by equation 10.

4.2.2. Comparing Deposited Power Capabilities for X-Sweeping and Y-Sweeping. Figure 4.7 shows the maximum power each type of beam sequence allows in order to reach a maximum focal spot temperature of 2600°C. The green lines represent a

X-Sweeping beam sequence (Figure 4.7a) while the purple lines represent a Y-Sweeping beam sequence (Figure 4.7b). Looking at the X-Sweeping plot, for a stationary anode (Rotational Surface Speed=0 m/s), the maximum deposited power increases with the Sweeping speed. For the rotating cylindrical anode, the maximum deposited power is constant until X-Sweeping temperature rise time, Δt_X, is less than Δt_{rot}. After which the rotating anode power curve converges with the stationary anode curve. Notice the acquisition time for a focal spot 1 mm wide drops quickly as the sweeping speed increases (orange line).

The same initial behavior shows up in the Y-Sweeping plot, except the deposited power does increase before eventually converging with the stationary anode line. This is due to the superposition of the rotational speed and the Y-Sweeping speed. The behavior continues until the acquisition time is less than Δt_Y. For lower sweeping speeds, the maximum deposited power is mostly dominated by the rotational speed, although the Y-Sweeping does contribute slightly. For higher sweeping speeds, the X-Sweeping allows for significantly higher maximum deposited powers when compared to the Y-Sweeping.

The two plots in Figure 4.8 represent the energy deposited in the focal spot for various acquisition times. The rotational surface speed for both plots is 200 m/s. Using equations 9 and 10, the corresponding sweeping speeds for each designated acquisition time was calculated. For both plots, the energy deposited in the focal spot during the acquisition time increases linearly with acquisition time, although the sweeping speed decreased with increasing acquisition time. A blue line in each plot represents the step-and-shoot sequence in order to easily compare the sequences. It's plain to see that the step-and-shoot allows more energy to be deposited per focal spot regardless of the acquisition

time. Another takeaway is the energy deposited in the focal spot per acquisition is greater for y-sweeping than x-sweeping for identical beam areas (i.e. length X width).

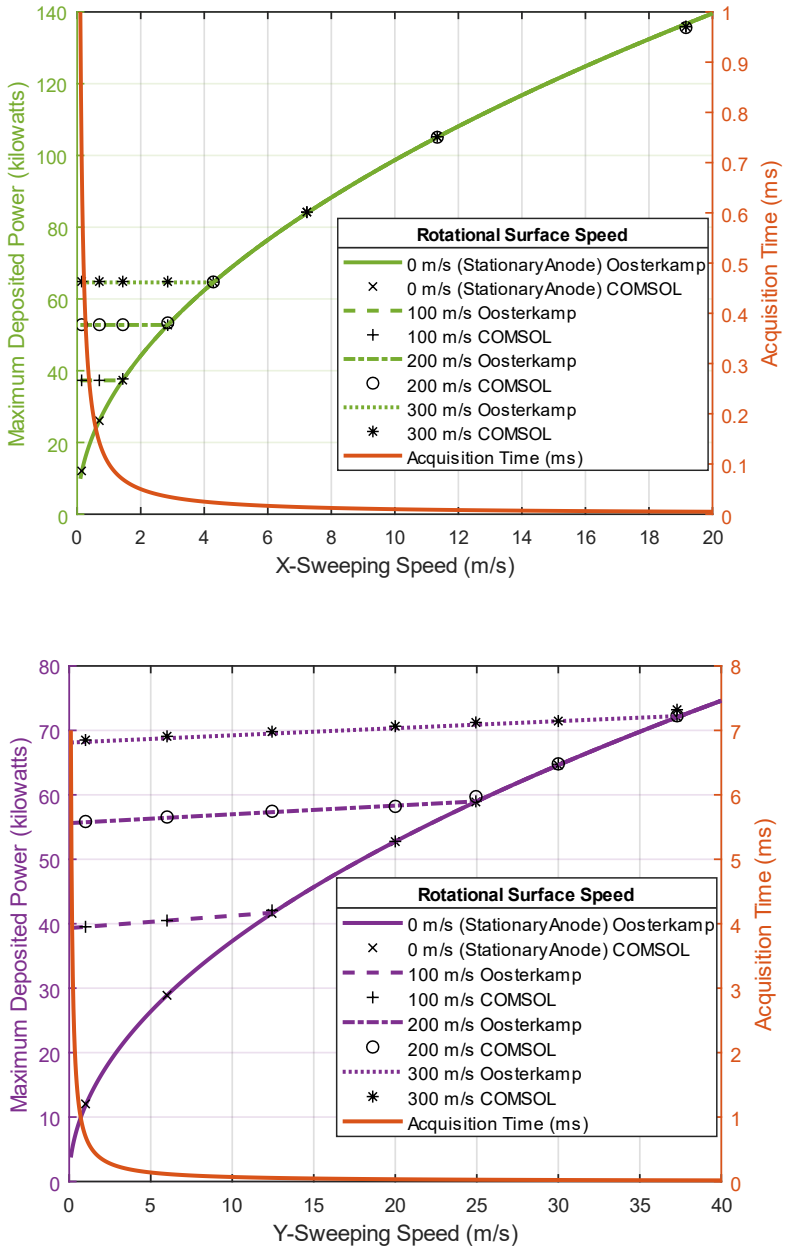

Figure 4.7 Maximum deposited power for a) 0.9 mm wide x-sweeping b) 6.3 mm long y-sweeping

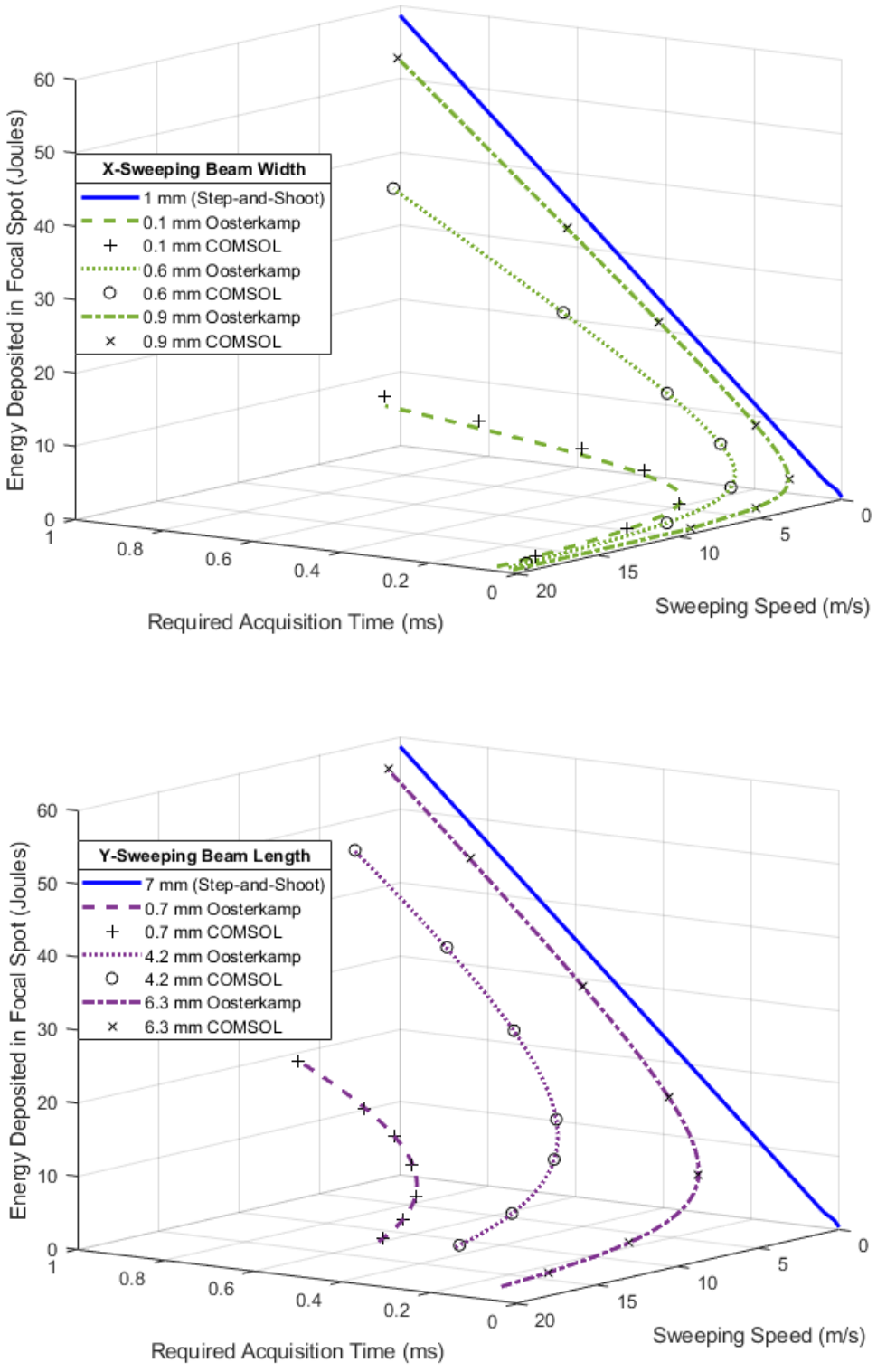

Figure 4.8 Energy deposited in focal spot for: a) x-sweeping b) y-sweeping

4.2.3. Step-And-Shoot. Strictly staying with step-and-shoot beam sequences allows the designer to make the most out of each x-ray projection in the multisource system. With no sweeping, the total energy deposited into the focal spot during the acquisition time for a stationary target (shown with red line) increases with the square-root of acquisition time. However, for the rotating cylindrical anodes in step-and-shoot mode, the total energy deposited in the focal spot during the acquisition time increases linearly with increasing acquisition time (Figure 4.9). The faster the rotation speed, the steeper the slope of the line. This trend will last as long as the cylinder's diameter is large enough that the beam only encounters fresh tungsten during the acquisition time. Figure 4.10 shows how deposited power increases with rotational surface speed and focal spot size, assuming acquisition time of the focal spot is greater than Δt_{rot}. Given the current state-of-the-art in multisource x-ray technology, this is a huge leap forward in the goal of high-speed CT imaging.

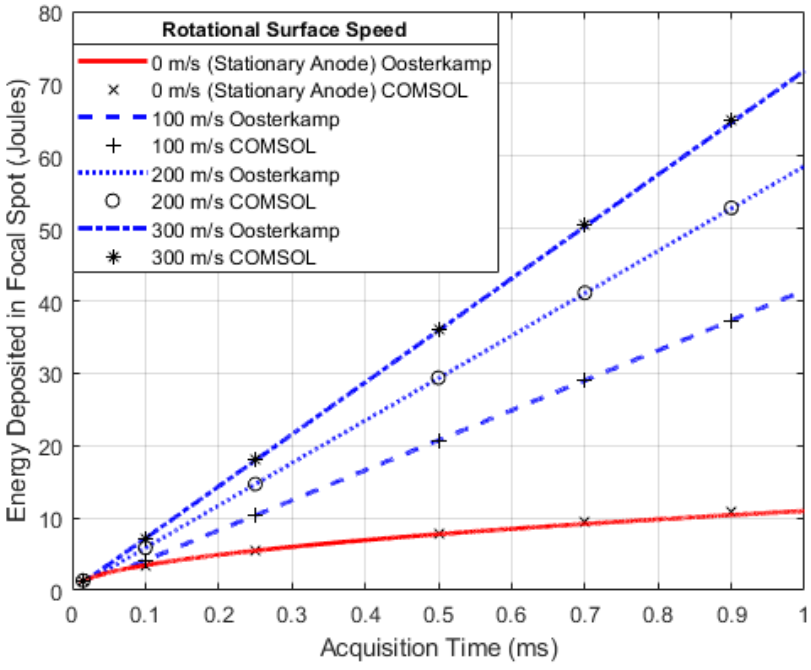

Figure 4.9 Energy deposited in focal spot for step-and-shoot beam sequence

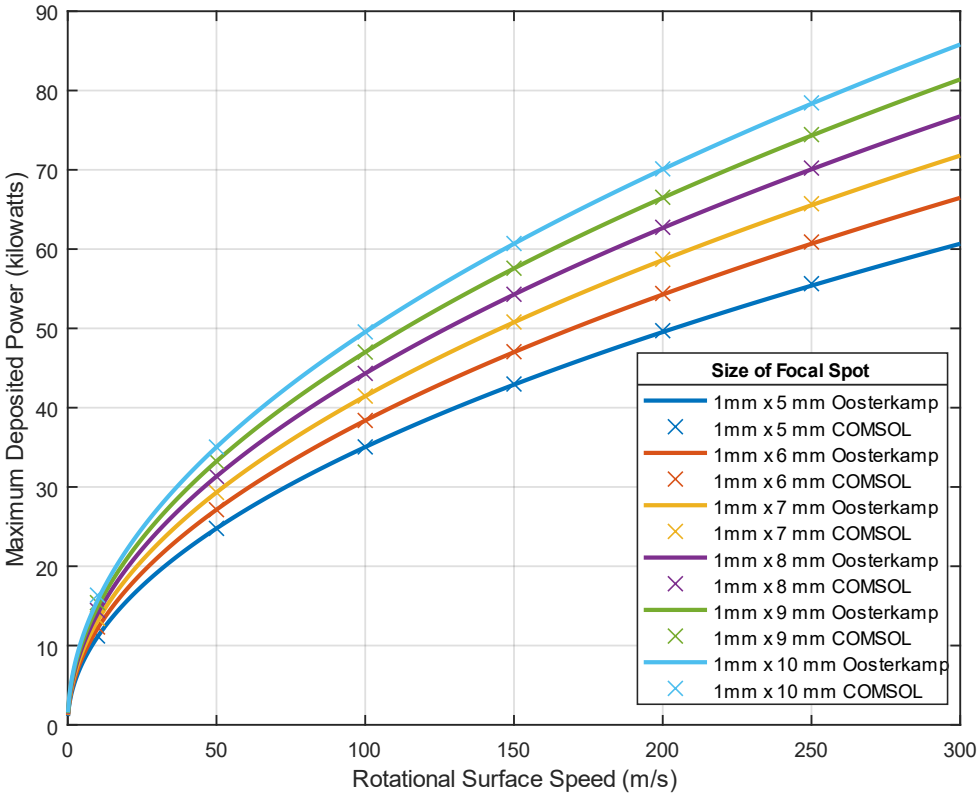

Figure 4.10 Deposited power vs rotational surface speed

4.3. DISCUSSION

The results showed that the step-and-shoot configuration allows for the most amount of heat to be deposited into the focal spot for a given acquisition time. The sweeping motion had very little effect on the maximum deposited power (especially in X-Sweeping) for low sweeping speeds. For higher speeds, the acquisition times became too short, and the power curve was identical to that of a stationary anode. Next, it was found that the amount of energy deposited per focal spot decreased with increasing sweeping speeds. The conclusion one could draw from this result is that sweeping does not actually

provide any benefit to output. An effective cylindrical multisource anode should employ a step-and-shoot beam sequence.

A cylindrical multisource system could be used in TBCT [12] to increase tube power, although a smaller diameter anode would need to be used to decrease size and weight. Due to the curved surface of the anode, a smaller diameter would limit the maximum focal spot length that can be projected onto the anode while still maintaining a 1 mm x 1 mm focal spot projection size on the detector. This would, of course, decrease the allowable power that can be used for imaging.

Another application is traumatic brain injury (TBI) research. Using a ring of cylinder multisource systems allows for 4D imaging of an impact onto a phantom. A rotating cylinder multisource anode is uniquely suited for this task. It combines the high-temporal resolution potential that multisource systems intrinsically possess and the heat management capabilities that conventional rotating anodes excel in.

4.4. CONCLUSIONS FOR SWEEPING STUDY

Three different beam sequences for a cylindrical multisource anode were compared using a combination of analytical and numerical approaches. It was shown that although adding a sweeping motion to the electron beam increased allowable beam power, the amount of energy deposited in the focal spot, and thus the amount of x-rays produced in that focal spot, decreased with increasing sweeping speed. This led to the inescapable conclusion that a step-and-shoot beam sequence should be used for the further study of the possibilities that a cylindrical anode could offer, such as significant increase in temporal resolution when compared to conventional CT.

5. DESIGN CONSIDERATIONS FOR CYLINDER MULTISOURCE ANODE

Computed Tomography (CT) scanners are one of the most widely used diagnostic tools. The most common designs involve an x-ray tube and a detector quickly rotating around the patient. Although great advances in tube and detector design have increased the rate at which image slices can be acquired[1], [2], [4], the mechanical stress from the heavy, rotating components prevents any significant gain[7].

One way to solve this problem is to completely remove gantry rotation by placing multiple sources axially around the target object. This is referred to as a multi-source (or distributed source) x-ray system. Previous research[14]–[17] typically used a stationary, angled anode. And while mechanically this is advantageous, the lack of movement prevented high heat loads from being applied to the target, limiting the x-ray output.

This section suggests the possibility that replacing the stationary, angled anode with a rotating, cylindrical anode in a multi-source system would allow for much greater x-ray output per source projection. For this hypothesis to be supported, a study of the thermal load for various cases of size and rotational speed needs to be performed. The curved surface of the cylinder means the thermal load from the incident electron beam will not be uniform across the target surface, as is the case for a traditional, angled anode. To compound the matter, the proportion of energy carried away by electron backscatter is angular dependent[37], [45], [46], meaning this too will contribute to the differential thermal load along the length of the source projection area (called a focal spot). The consequence of this has not been studied. A thorough investigation into the effect of this uneven loading is the primary objective of this paper.

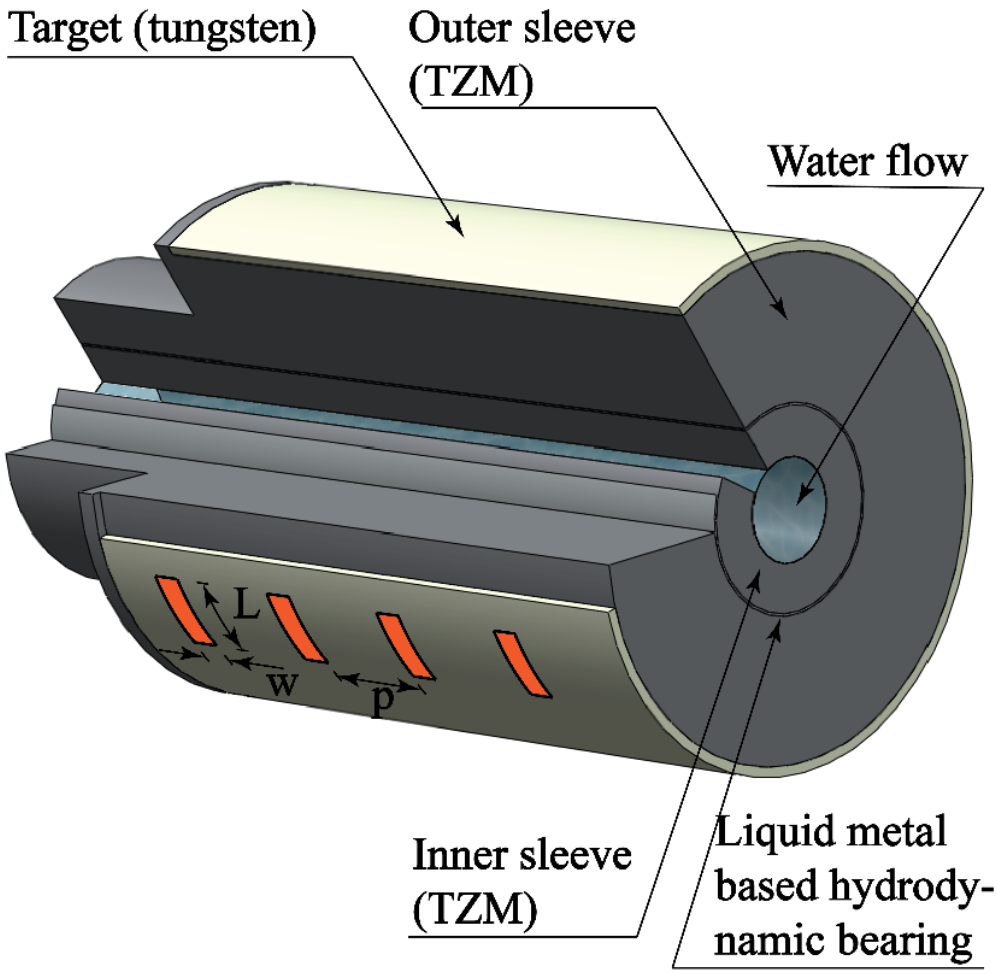

Figure 5.1 Cross-section of the cylinder multisource x-ray anode

5.1. METHODS FOR DESIGN CONSIDERATIONS

Figure 5.1 shows a cross-section of the cylinder multisource anode. The length of the tungsten target area is 400 mm with a thickness of 1 mm. This layer is sintered onto a TZM outer sleeve which rotates around the stationary TZM inner sleeve. The interface between the two sleeves is lubricated by a gallium-based liquid metal bearing. The anode is cooled by a 10 mm diameter water channel flowing at 5 m/s. There are 30 focal spots along the target area of the anode. A full CT system would contain 7 multisource anodes placed radially around the object to be imaged. 210 projections (7 anodes x30 focal spots

each) would form one complete slice[22]. Real-time is defined as 30 slices (called frames) per second.

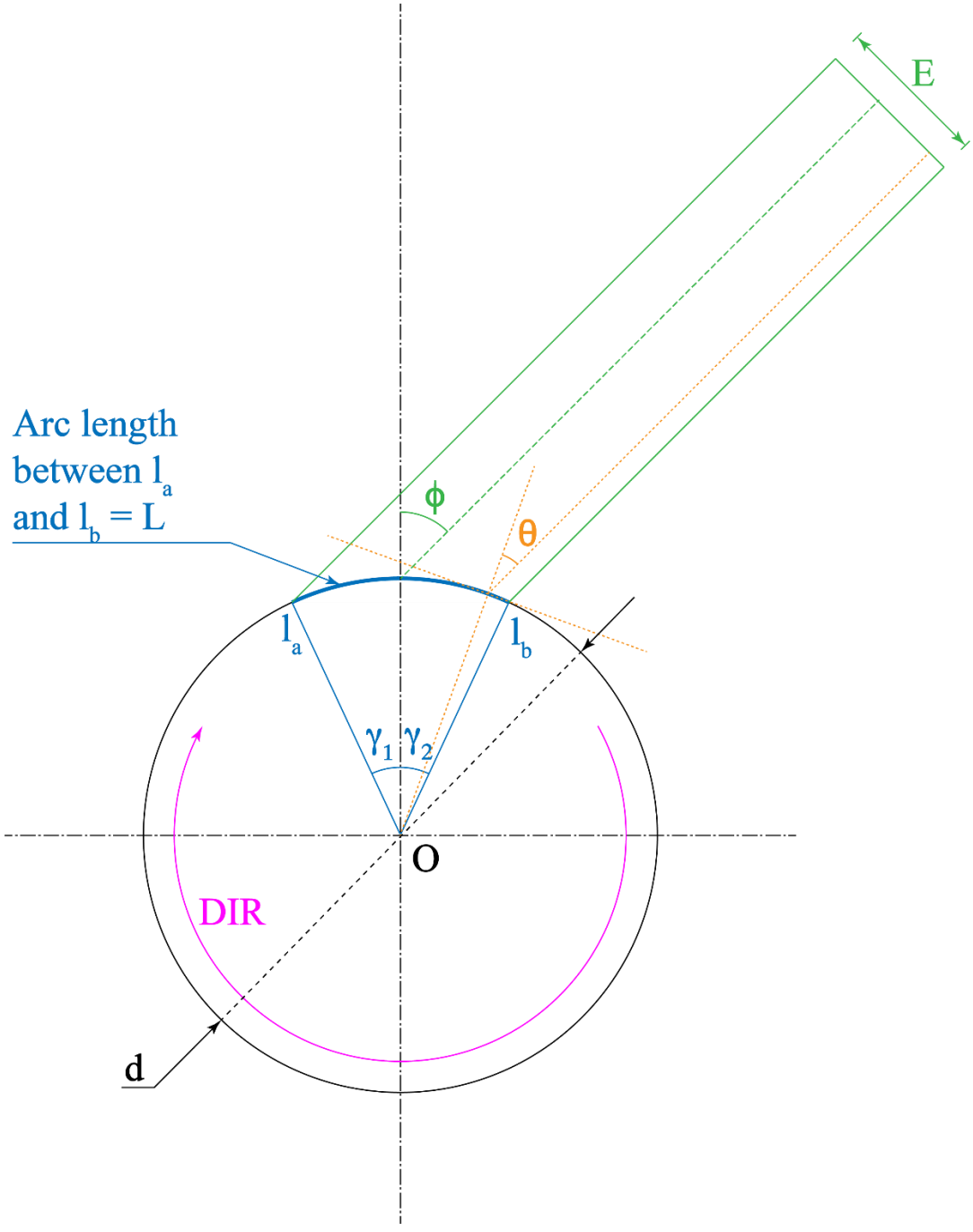

Figure 5.2 Geometry of the cylindrical anode

5.1.1. Description of the Geometry. An electron beam is accelerated toward the anode and bombards the focal spot for a fixed exposure time, depositing heat and emitting x-rays in all directions. During the exposure time, the anode rapidly rotates, spreading the deposited heat around axially. For a rotating anode, the temperature rise time is the focal spot length divided by the surface speed[85]. After this rise time, the maximum temperature in the anode is constant.

Figure 5.2 shows the geometry of the cylindrical anode with diameter d being bombarded by an electron beam of width, E. The projection of E onto the cylinder surface at angle Φ is defined as the Focal Spot Length, L, bounded by the points l_a and l_b. θ is the local incident angle of the incoming electrons inside the beam. This value varies across length, L. γ_1 and γ_2 are the angular deviations from the center of the focal spot that correspond with the points l_a and l_b, respectively. Since angle Φ is defined by the vertical axis that runs through the center of the L, γ_1 equals γ_2. Take note that the center of the electron beam does not necessarily intersect with the center of the focal spot. The equation for the electron beam width for a fixed focal spot length is given by the following equation:

$$E = d*\cos(\Phi)*\sin(\frac{L}{d}) \quad (11)$$

The maximum beam angle, Φ_{max}, is the angle Φ at which the beam line intersecting at point l_a is tangent to the cylinder surface at that point. This should convince you that $\Phi_{max} = \boldsymbol{\pi}/2 - L/d$.

5.1.2. Angular Dependence of Backscatter Energy Fraction. For the curved surface shown in Figure 5.2, the local incident angle, θ, of the electron beam varies along L. For large diameters and small focal spots ($L/d \approx 0$), this difference is negligible; but as L/d increases, the variation becomes increasingly more dramatic.

It is already known that the electron backscatter fraction is dependent on the local incident angle, θ, of the beam[37], so MCNP6[33], [87] was used to find the angular dependency of the energy that the backscattered electrons take away from the focal spot. The MCNP geometry consisted of a 2-millimeter diameter sphere half-filled with tungsten and the other half filled with vacuum air (shown in Figure 5.3). A circular electron beam 10 micrometers in diameter pointed in the negative y-direction released 5,000,000 particles. To test the energy dependency of electron backscatter, the electron energies for the source were 50 keV, 100 keV, and 150 keV. The incident angle θ was placed at 0º, 10º, 20º, 30º, 40º, 50º, 60º, 70º, 80º, and 85º. F1 and *F1 tallies were placed on the outer surface of the sphere to find backscatter fraction and energy spectrum for each combination of energy and angle.

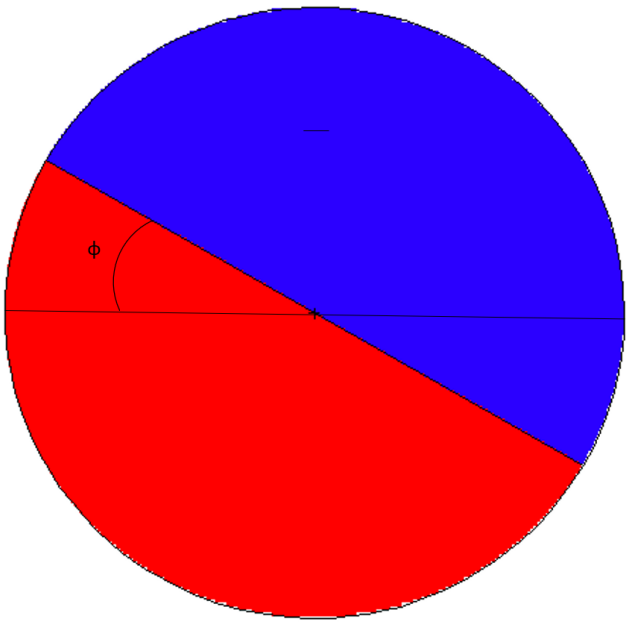

Figure 5.3 MCNP geometry

5.1.3. Finite Element Simulation. The backscattered electron energy fraction, β, was defined as the fraction of electrons backscattered multiplied by the average energy of those electrons divided by the original energy of the incident electrons. β for each angle was found and the MATLAB curve-fit tool was used to find an empirical equation for β(θ). This was then put into COMSOL Multiphysics®[34] as a function for the Heat Flux Node, acting as the focal spot. The units for angle are in radians. The Heat Flux Node does not take curvature of the incident surface into account which can cause a conservation of energy issue for a cylindrical surface (total power deposited on a surface is greater than input power of the beam). Therefore, a correction for surface curvature was also added. The heat deposited outside the focal spot from backscattered electrons returning to the anode was not considered, as Kellermeier stated that they had negligible contribution to temperature rise[14]. It can also be assumed that an electron trap was used to remove backscattered electrons away from the anode. Also, the loss of power from x-ray production was ignored since it only accounts for less than 1% of the deposited energy in the diagnostic energy range[37]**.**

5.1.3.1. Power efficiency per incident beam angle. Temperature rise over a focal spot is correlated with the power per unit area deposited in the focal spot during exposure[44]. Conventional angled anodes have a flat surface, meaning the power per unit area deposited in the target is constant across the area of the focal spot. For cylindrical anodes, however, the heat is not deposited uniformly because the backscatter fraction of electrons changes across the length of the focal spot.

COMSOL was used to find the power efficiency of the electron beam on the surface of the cylinder anode for various values of L/d, as the curvature of the anode across the

focal spot was solely dependent on the ratio of focal spot length over diameter of the anode. Power efficiency was defined as the total power deposited in the focal spot area divided by the total power of the incoming beam (called tube power). In COMSOL, a boundary heat flux was incident on the exterior surface of the anode while the interior side (1 mm away) was set at 20ºC. A boundary probe was placed on the surface of the focal spot to measure the integrated power deposited in the target. The simulation was ran with 1000 Watts tube power and the power that was picked up by the probe was tallied in the output as the deposited power.

For the cylindrical anode, L/d values were set at 0.01, 0.1, 0.2, and 0.5. The power efficiency was measured at angles of 0º through Φ_{max}. The anode had no rotation since power efficiency was independent of rotation. For comparison, an angled anode was ran as well. The focal spot size was 7 mm in length.

5.1.3.2. Maximum deposited power per angle. Deposited power was found for a maximum focal spot temperature of 2600ºC. Since the amount of heat that is actually deposited onto the focal spot is proportional to x-ray output, that was the value that was used for comparison. Different values of deposited power were found for angles of 0º through Φ_{max}. Values for L/d were set at 0.01, 0.1, 0.2, and 0.5. The focal spot size was 7 mm in length and 1 mm in width. The rotational surface speed was 100 m/s. Both rotation directions were ran (Clockwise and Counterclockwise) using Figure 5.2 as the reference direction for Clockwise.

The boundary heat flux was again incident on the exterior target surface. The other surfaces were open boundaries, which treated the material as extending to infinity in each direction. This assumption was valid, as short-term temperature rise was all that was being

measured. For long-term behavior, other components of the cylindrical anode should be included. Tungsten was used as the target material. The density, heat capacity, and thermal conductivity were all temperature dependent[79]–[81].

Table 5.1 Baseline properties

Property:	Baseline value:	Description:
Gallium Film Thickness (h)	50 [μm]	Gap thickness of liquid metal bearing.
Anode Diameter (d)	200 [mm]	Diameter of cylindrical anode
Water Speed (V)	5 [m/s]	Velocity of cooling fluid running through center of anode
Tungsten Thickness (TG)	1 [mm]	Target thickness layer
Tungsten/TZM Interface Thermal Conductivity (ITC)	80 [W/m-K]	Thermal conductivity between tungsten layer and TZM body
Frame Acquisition Time (TR)	0.0333 [sec]	Time for CT to fully acquire one slice
Pause-Time between CT frames (DT)	1 [msec]	Time between slices for patient movement, etc.

5.1.3.3. Sensitivity analysis of thermal properties and dimension changes. A long-term sensitivity analysis of the cylinder anode shown in Figure 5.1 was performed by varying dimensional and mechanical properties and solving for steady-state temperature in the tungsten. The baseline properties being changed are shown in Table 5.1. The deposited

power, K, is 50,000 Watts spread over the 210 focal spots (number of projections in a frame). The average power deposited in each focal spot is equal to:

$$K_{PerFS} = {K * (1/(TR + DT)) * TR}/{210} \quad (12)$$

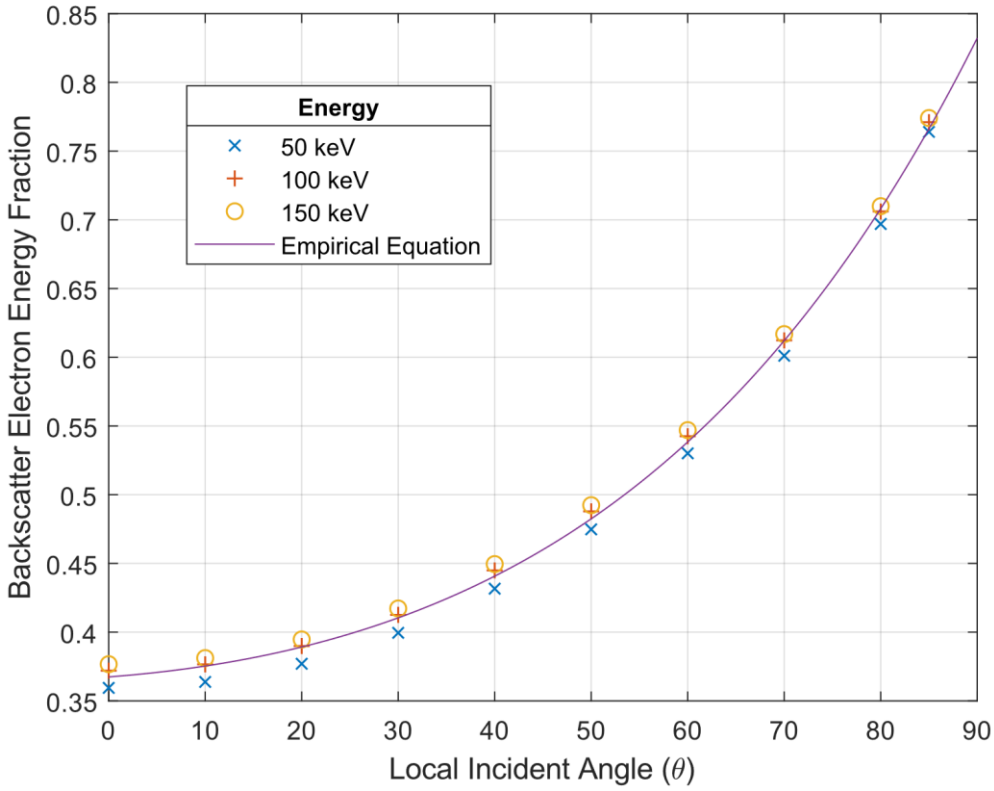

Figure 5.4 Backscatter electron energy fraction

5.2. RESULTS FOR DESIGN CONSIDERATIONS

The following subsections give the results from the thermal loading simulations, including a sensitivity analysis for a simple rotating cylindrical anode design.

5.2.1. Electron Backscatter. The backscatter electron energy fraction β(θ) was found to be relatively independent of incident electron energy, although it did increase

slightly with increasing energies (Figure 5.4). The average energy of the backscattered electrons increases with increasing angles θ. Also, as θ increases, the fraction of the energy carried away by backscattered electrons increases exponentially. The equation for the relationship between backscattered electron energy fraction and angle is:

$$\beta(\theta)=0.2892*e^{(-0.2564*\theta)}+0.07823*e^{(1.337*\theta)} \quad (13)$$

where angle is in radians. This equation does not account for curvature of the anode.

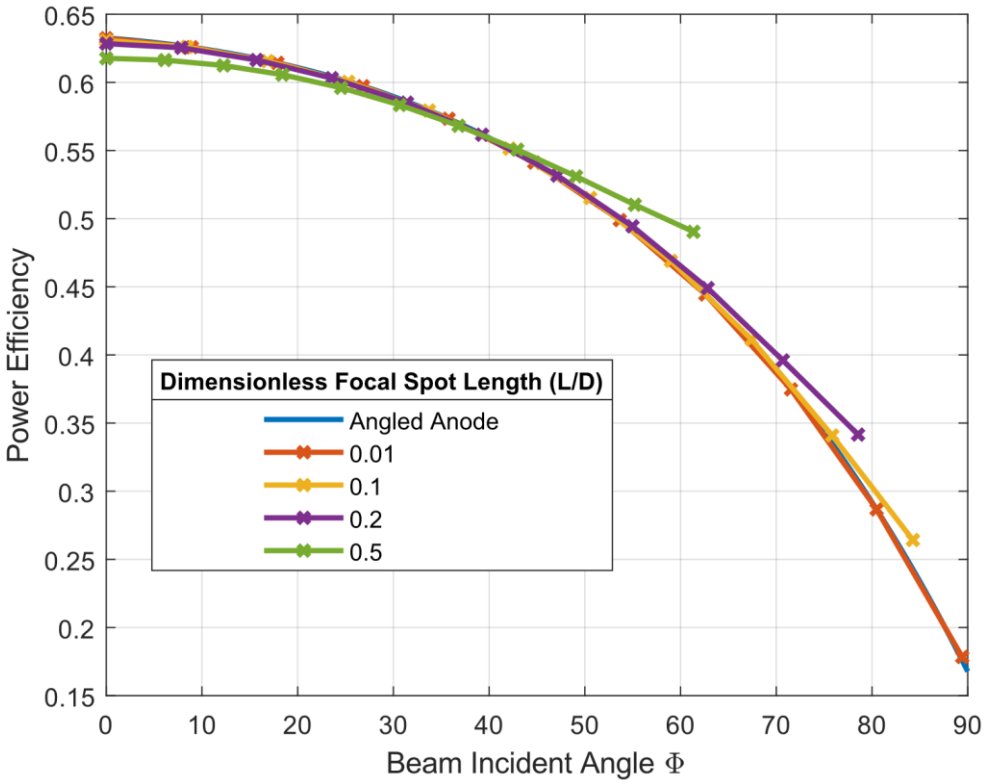

Figure 5.5 Power efficiency per angle

5.2.2. Power Efficiency. The lower values for L/d conform with the curve for a flat surface (Figure 5.5). The greater values, however, diverge significantly. For L/d=0.5, the value at Φ_{max} is about 49.0%.

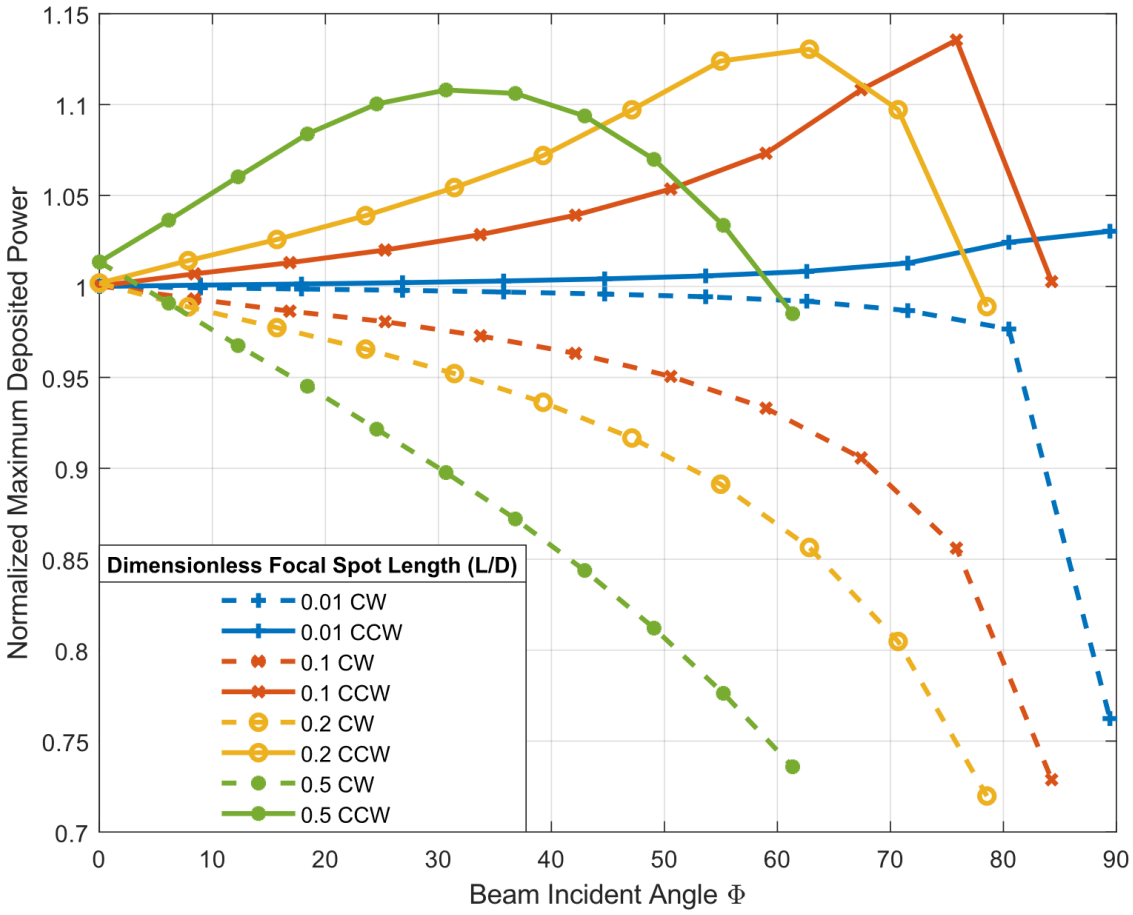

Figure 5.6 Effect of L/d, rotation direction, and beam angle on normalized deposited power. The normalized deposited power is defined as the maximum deposited power at beam angled divided by the maximum deposited power of flat angled anode at normal incidence. The normalized deposited power of a flat anode is unity for all angles.

5.2.3. Rotation Direction and L/d. L/d and rotation direction play a significant part in the angular dependence of the normalized maximum deposited power (Figure 5.6). At Φ = 0, the rotational direction does not change maximum deposited power. However, L/d does have a slightly positive impact on that value. For greater values of Φ, the rotational direction is significant. The counterclockwise direction allows the maximum deposited power to temporarily increase in value while the clockwise direction generally decreases

the maximum deposited power with Φ. The peak for L/d = 0.2 is around 13% higher than the power for a traditional angled anode.

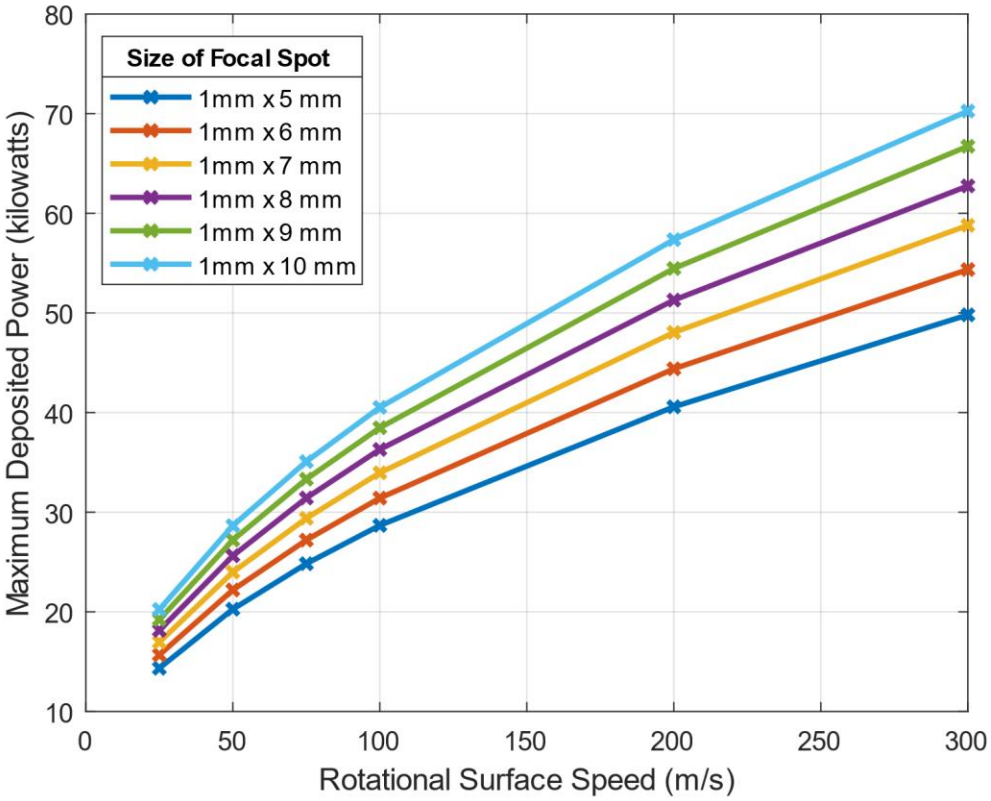

Figure 5.7 Maximum deposited power vs speed and focal spot length

5.2.4. Maximum Deposited Power VS Focal Spot Size and Rotational Speed. Figure 5.7 shows the relationship of maximum deposited power with varying focal spot lengths and rotational speeds for an anode with L/d close to 0. The length of the focal spot plays a significant role in the maximum power the anode is capable of handling. The rotational surface speed also has a positive influence on the maximum power.

5.2.5. Sensitivity Analysis. Water speed has the largest effect on long-term tungsten temperature. The anode diameter and frame acquisition time both had a moderate

effect. Pause time, tungsten thickness, and film thickness had no significant effect. Tungsten interface thermal conductivity had a large effect for very low values but quickly plateaued at around 5% of baseline (Figure 5.8).

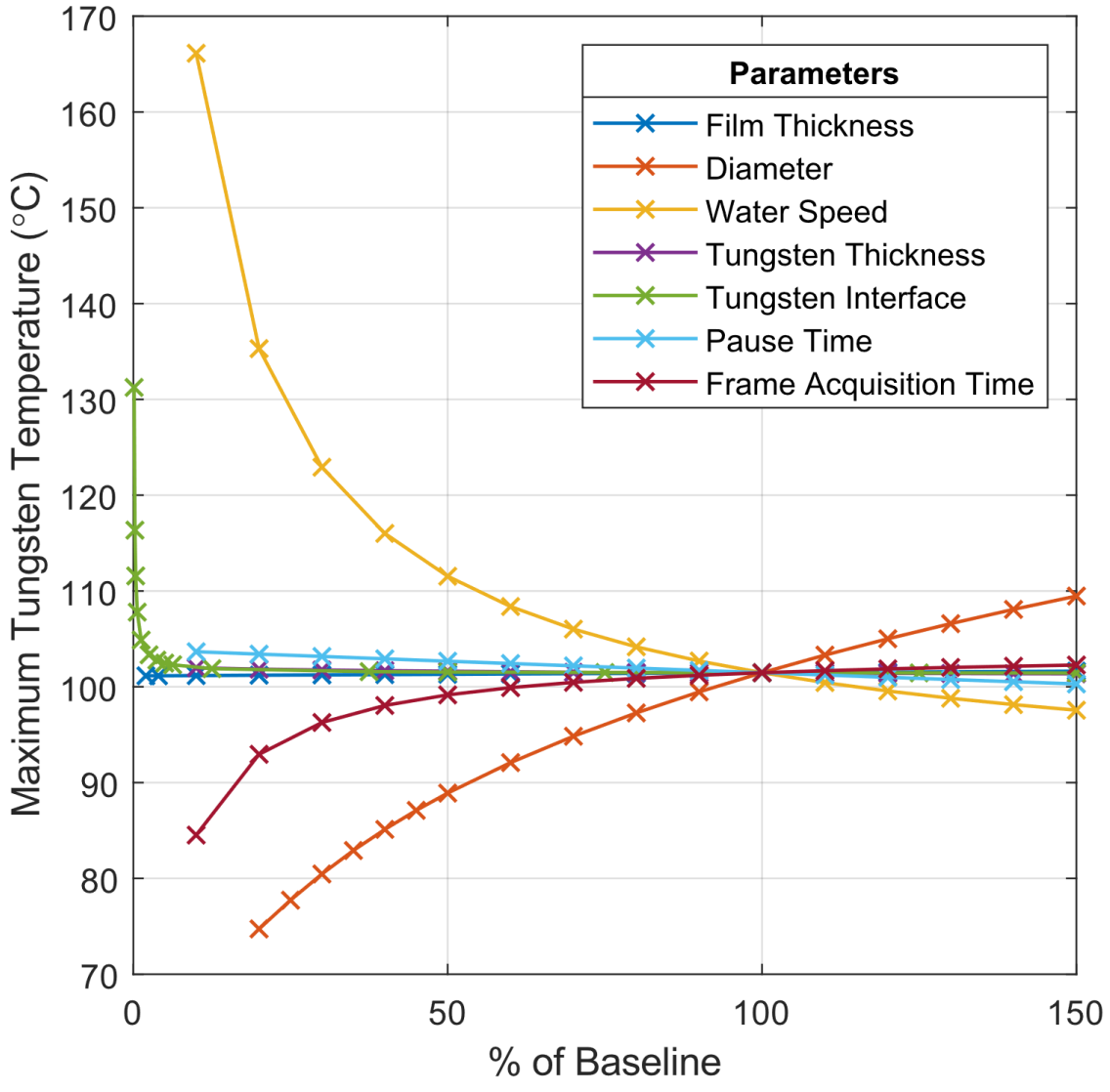

Figure 5.8 Sensitivity analysis

5.3. DESIGN IMPLICATIONS AND DISCUSSION

The results suggest the ratio of the focal spot length to anode diameter should be large enough to take advantage of the curvature of the surface. Unfortunately, the power efficiency drops with increasing beam angle, which is where the advantageous region appears in Figure 5.6. If electron beam efficiency is the primary factor for anode design, then the best choice would be to have a dimensionless focal spot length that is very small. This would allow the efficiency profile to be very similar to a flat anode, while still having the rotational benefit of the cylindrical anode. If a larger dimensionless focal spot size is used, the rotational direction of the anode must be in the counterclockwise direction or any benefit will be lost.

If a designer knows their focal spot size and deposited power requirements (imaging exposure needs), Figure 5.7 could be used to find the required rotational surface speed to achieve that power. Figure 5.6 would then be used to find the optimum incident angle and anode diameter. Finally, Figure 5.5 would allow the designer to estimate the required tube power based on efficiency.

The sensitivity analysis suggests that the water speed is the most important factor. Anode diameter and frame acquisition time are the next important factors, although these would most likely be fixed depending on the application. The results came from steady-state conditions which could be considered a conservative estimate of anode temperature just before a new acquisition cycle starts. Even in this case, the temperature rise in the tungsten is only 80° above initial starting conditions (i.e. room temperature). Assuming the maximum temperature of 2600°C in the tungsten, this would only affect the maximum

allowable deposited power by a little over 3%, making the plot in Figure 5.7 a reliable estimate, even for long-term operation.

5.4. CONCLUSIONS FOR DESIGN CONSIDERATIONS

The angular dependence of the thermal loading for a rotating cylindrical multisource anode was investigated. The results showed that the ratio of focal spot length over diameter played a major role in maximum deposited power, with greater values of that ratio allowing for up to a 13% increase at certain angles. The sensitivity analysis suggests that, for long-term operation, the water speed will play a crucial role in this design.

6. DISCUSSION AND CONCLUSION

6.1. GENERAL CONCLUSIONS

A linear, compact x-ray tube and a cylindrical anode designed for multisource CT imaging were studied. Tungsten target thickness and anode material and thickness were varied so we could investigate the effect of these parameters on anode material temperature. It was found that the thickness of the tungsten did not have a significant impact on the temperature of the anode. We found that beryllium was the best anode for the widest range of tube powers, providing the best combination of heat transfer properties, high melting temperature, and low x-ray attenuation. Based upon the temperature plateau at anode thickness greater than 0.5 mm, a plot was created to give the power range of the x-ray tubes. It was found that the focal spot size in the transmission anode prevented an acceptable level of deposited electron beam power for the application of real-time CT.

Based upon the findings for the linear x-ray tube, the focus was switched to a rotating cylindrical anode shape. The assumption was that the anode would have the benefit of both line focusing and rotatory motion, as well as providing ample surface area for an adequate number of focal spots. Investigation into the effects of rotation and beam sweeping on maximum deposited power were first studied. It was found that the step-and-shoot sequence was optimal, as the heat-spreading benefit from rotation dominated maximum deposited power for low sweeping speeds. Although higher sweeping speeds did increase the maximum deposited power, the deposited energy per acquisition time in the focal spot decreased.

The effects of the curved geometry on maximum deposited power in a cylindrical multisource anode had not been studied before. The amount of energy carried away from the anode by backscattered electrons changes as the incident angle changes. Since the anode is curved, an electron beam with a relatively large width would have different local incident angles at different parts of the beam. This causes an uneven heat deposition rate along the focal spot size. It was found that, although the power efficiency decreases at higher beam incident angles, the maximum deposited power can increase by as much as 13%. Also, a sensitivity analysis found the speed of the coolant water had the biggest effect on long term temperature.

6.2. FUTURE WORK

The next step for this project would be to perform a beam optics study. We assumed the anode would be around 450 mm in length. Past studies have shown it is not feasible to have a single beam being steered along that entire length[17]. Therefore, the x-ray module would probably consist of multiple cathodes. Another reason for a beam optics study is the incident beam angle greater than 0 which would mean the beam would have to be steered in both the lateral and vertical direction. In the near future, a prototype cylindrical anode will be fabricated and studied to perform these and other studies.

REFERENCES

[1] H. Hu, "Multi-slice helical CT: Scan and reconstruction," *Med. Phys.*, vol. 26, no. 1, pp. 5–18, 1999.

[2] C. R. Crawford and K. F. King, "Computed tomography scanning with simultaneous patient translation," *Med. Phys.*, vol. 17, no. 6, pp. 967–982, 1990.

[3] J. Hsieh, *Computed Tomography: Principles, Design, Artifacts, and Recent Advances*, Third. Bellingham, Washington: SPIE, 2015.

[4] T. G. Flohr *et al.*, "First performance evaluation of a dual-source CT (DSCT) system," *Eur. Radiol.*, vol. 16, no. 2, pp. 256–268, 2006.

[5] M. Lell *et al.*, "Prospectively ECG-triggered high-pitch spiral acquisition for coronary CT angiography using dual source CT: Technique and initial experience," *Eur. Radiol.*, vol. 19, no. 11, pp. 2576–2583, 2009.

[6] T. R. C. Johnson *et al.*, "Material differentiation by dual energy CT: Initial experience," *Eur. Radiol.*, vol. 17, no. 6, pp. 1510–1517, 2007.

[7] T. G. Flohr, R. Raupach, and H. Bruder, "Cardiac CT: How much can temporal resolution, spatial resolution, and volume coverage be improved?," *J. Cardiovasc. Comput. Tomogr.*, vol. 3, no. 3, pp. 143–152, 2009.

[8] V. B. Neculaes, P. M. Edic, M. Frontera, A. Caiafa, G. Wang, and B. De Man, "Multisource X-Ray and CT: Lessons learned and future outlook," *IEEE Access*, vol. 2, pp. 1568–1585, 2014.

[9] M. A. Speidel, "Inverse geometry x-ray imaging: application in interventional procedures," *J. Am. Coll. Radiol.*, vol. 8, no. 1, pp. 74–77, 2011.

[10] M. A. Speidel, B. P. Wilfley, J. M. Star-Lack, J. A. Heanue, and M. S. Van Lysel, "Scanning-beam digital x-ray (SBDX) technology for interventional and diagnostic cardiac angiography," *Med. Phys.*, vol. 33, no. 8, pp. 2714–2727, 2006.

[11] S. S. Hsieh, J. A. Heanue, T. Funk, W. S. Hinshaw, and N. J. Pelc, “The feasibility of an inverse geometry CT system with stationary source arrays,” *Med. Phys.*, vol. 40, no. 3, 2013.

[12] T. Zhang, D. Schulze, X. Xu, and J. Kim, “Tetrahedron beam computed tomography (TBCT): A new design of volumetric CT system,” *Phys. Med. Biol.*, vol. 54, no. 11, pp. 3365–3378, 2009.

[13] A. Cramer *et al.*, “Stationary Computed Tomography for Space and other Resource-constrained Environments,” *Sci. Rep.*, vol. 8, no. 1, pp. 1–10, 2018.

[14] M. Kellermeier, C. Bert, and R. G. Müller, “A novel concept for CT with fixed anodes (FACT): Medical imaging based on the feasibility of thermal load capacity,” *Phys. Medica*, vol. 31, pp. 425–434, 2015.

[15] M. Kellermeier, “Physical assessment of a novel concept for computed tomography with a stationary source ring of fixed X-ray anodes for medical imaging,” 2015.

[16] B. J. Walker, “A Modular Multi-Source X-ray Tube for Novel Computed Tomography Applications,” University of Wisconsin-Madison, 2017.

[17] B. J. Walker, J. Radtke, G. H. Chen, K. W. Eliceiri, and T. R. Mackie, “A beam optics study of a modular multi-source X-ray tube for novel computed tomography applications,” *Nucl. Instruments Methods Phys. Res. Sect. A Accel. Spectrometers, Detect. Assoc. Equip.*, vol. 868, no. June, pp. 1–9, 2017.

[18] M. A. Lewis, A. Pascoal, S. F. Keevil, and C. A. Lewis, “Selecting a CT scanner for cardiac imaging: The heart of the matter,” *Br. J. Radiol.*, vol. 89, no. 1065, pp. 1–11, 2016.

[19] A. V. Avachat, “Design and development of a compact x-ray tube for stationary CT architecture In Partial Fulfillment of the Requirements for the Degree,” 2018.

[20] A. V. Avachat, W. W. Tucker, C. H. C. Giraldo, and H. K. Lee, “Particle-in-cell simulations of electron focusing for a compact x-ray tube comprising CNT-based electron source and transmission type anode,” *IEEE Trans. Electron Devices*, vol. 66, no. 3, pp. 1525–1532, 2019.

[21] A. V. Avachat, W. W. Tucker, C. H. C. Giraldo, D. Pommerenke, and H. K. Lee, “Looking Inside a Prototype Compact X-ray Tube Comprising CNT-Based Cold Cathode and Transmission-Type Anode,” *Radiat. Res.*, 2020.

[22] J. C. Park *et al.*, “Fast compressed sensing-based CBCT reconstruction using Barzilai-Borwein formulation for application to on-line IGRT,” *Med. Phys.*, vol. 39, no. 3, pp. 1207–1217, 2012.

[23] M. L. Taubin, D. A. Chesnokov, and A. A. Pavlov, “Cathodes for medical purpose X-Ray Tubes,” in *Journal of Physics: Conference Series*, 2017, vol. 808, no. 1.

[24] P. Kandlakunta, R. Pham, R. Khan, and T. Zhang, “Development of multi-pixel x-ray source using oxide-coated cathodes,” *Phys. Med. Biol.*, vol. 62, no. 13, pp. N320–N336, 2017.

[25] J. Zhang *et al.*, “Stationary scanning x-ray source based on carbon nanotube field emitters,” *Appl. Phys. Lett.*, vol. 86, no. 18, pp. 1–3, 2005.

[26] W.Zhu, C. Bower, and O. Zhou, “Large current density from carbon nanotube field emitters,” vol. 75, no. 6, pp. 873–875, 1999.

[27] D. J. Heuscher, “Cylindrical X-Ray Tube for Computed Tomography Imaging,” US 7,305,063 B2, 2007.

[28] Philips, “Brilliance iCT configuration.” Philips, 2008.

[29] D. P. Boyd and M. J. Lipton, “Cardiac Computed Tomography,” *Proc. IEEE*, vol. 71, no. 3, pp. 298–307, 1983.

[30] D. P. Boyd, W. B. Herrmannsfeldt, J. R.Quinn, and Robert A Sparks, “X-Ray Transmission Scanning Sysytem and Method and Electron Beam X-ray Scan Tube for us Therewith,” 1982.

[31] D. P. Boyd *et al.*, “High-Speed, Multi-Slice, X-ray Computed Tomography,” in *Proc. SPIE 0372, Physics and Engineering in Medical Imaging*, 1982.

[32] D. Drouin, A. R. Couture, D. Joly, X. Tastiet, V. Aimez, and R. Gauvin, "CASINO V2.42-A Fast and Easy-to-use Modeling Tool for Scanning Electron Microscopy and Microanalysis Users," *Scanning*, vol. 29, pp. 92–101, 2007.

[33] J. T. Goorley *et al.*, "MCNP6 user's manual," 2013.

[34] S. COMSOL AB, Stockholm, "COMSOL Multiphysics® v.5.4 COMSOL AB, Stockholm, Sweden." [Online]. Available: ww.comsol.com.

[35] L. Solymar and D. Walsh, *Electrical properties of materials*, 8th ed. Oxford University Press, 2010.

[36] J. T. Bushberg, J. A. Seibert, E. M. Leidholdt, and J. M. Boone, *The Essential Physics of Medical Imaging , 3rd ed.* Wolters Kluwer Health, 2012.

[37] R. Behling, *Modern Diagnostic X-Ray Sources*. 2015.

[38] J. Shan, O. Zhou, and J. Lu, "Anode thermal analysis of high power microfocus CNT x-ray tubes for in vivo small animal imaging," *Med. Imaging 2012 Phys. Med. Imaging*, vol. 8313, p. 83130O, 2012.

[39] V. E. Cosslett and R. N. Thomas, "Multiple scattering of 5-30 keV electrons in evaporated metal films II: Range-energy relations," *Br. J. Appl. Phys.*, vol. 15, no. 11, pp. 1283–1300, 1964.

[40] R. Whiddington and J. J. Thomson, "The Transmission of Cathode Rays through Matter," *Proc. R. Soc. London. A.*, vol. 86, pp. 360–370, 1912.

[41] J. R. Young, "Dissipation of energy by 2.5–10 keV electrons in Al2O3," *J. Appl. Phys.*, vol. 28, no. 5, 1957.

[42] M. J. Berger, J. S. Coursey, M. A. Zucker, and J. Chang, "ESTAR, PSTAR, and ASTAR: Computer Programs for Calculating Stopping-Power and Range Tables for Electrons, Protons, and Helium Ions (version 1.2.3)," *National Institute of Standards and Technology, Gaithersburg, MD.*, 2005. [Online]. Available: http://physics.nist.gov/Star.

[43] G. G. Poludniowski and P. M. Evans, “Calculation of x-ray spectra emerging from an x-ray tube. Part I. Electron penetration characteristics in x-ray targets,” *Med. Phys.*, vol. 34, no. 6Part1, pp. 2164–2174, 2007.

[44] W. J. Oosterkamp, “The heat dissipation in the anode of an X-ray tube,” *Philips Res. Rep.*, vol. 3, pp. 49–59, 1948.

[45] E. S. M. Ali and D. W. O. Rogers, “Benchmarking EGSnrc in the kilovoltage energy range against experimental measurements of charged particle backscatter coefficients,” *Phys. Med. Biol.*, vol. 53, no. 6, pp. 1527–1543, 2008.

[46] E. S. M. Ali and D. W. O. Rogers, “Energy spectra and angular distributions of charged particles backscattered from solid targets,” *J. Phys. D. Appl. Phys.*, vol. 41, no. 5, 2008.

[47] E. S. M. Ali and D. W. O. Rogers, “Quantifying the effect of off-focal radiation on the output of kilovoltage x-ray systems,” *Med. Phys.*, vol. 35, no. 9, pp. 4149–4160, 2008.

[48] Z. Wen, N. J. Pelc, W. R. Nelson, and R. Fahrig, “Study of increased radiation when an x-ray tube is placed in a strong magnetic field,” *Med. Phys.*, vol. 34, no. 2, pp. 408–418, 2007.

[49] J. Freudenberger and L. Werner, “X-Ray Tube with a Backscattering Electron Trap,” US 2012/0170715A1, 2012.

[50] R. Zhou, X. Zhou, X. Li, Y. Cai, and F. Liu, “Study of the Microfocus X-Ray Tube Based on a Point-Like Target Used for Micro-Computed Tomography,” *PLoS One*, vol. 11, no. 6, pp. 1–12, 2016.

[51] M. M. Nasseri, “Determination of Tungsten Target Parameters for Transmission X-ray Tube: A Simulation Study Using Geant4,” *Nucl. Eng. Technol.*, vol. 48, no. 3, pp. 795–798, 2016.

[52] L. Tavora, E. J. Morton, and W. B. Gilboy, “Design considerations for transmission x-ray tubes operated at diagnostic energies,” *J. Phys. D. Appl. Phys.*, vol. 33, pp. 2497–2507, 2000.

[53] P. Kandlakunta, A. Thomas, Y. Tan, R. Khan, and T. Zhang, "Design and numerical simulations of W-diamond transmission target for distributed x-ray sources," *Biomed. Phys. Eng. Express*, vol. 5, no. 2, p. 025030, 2018.

[54] E. J. Grant, C. M. Posada, C. H. Castaño, and H. K. Lee, "A Monte Carlo simulation study of a flat-panel X-ray source," *Appl. Radiat. Isot.*, vol. 70, no. 8, pp. 1658–1666, 2012.

[55] E. J. Grant, C. M. Posada, C. H. Castaño, and H. K. Lee, "Electron field emission Particle-In-Cell (PIC) coupled with MCNPX simulation of a CNT-based flat-panel x-ray source," *Med. Imaging 2011 Phys. Med. Imaging*, vol. 7961, p. 796108, 2011.

[56] D. Chen *et al.*, "Transmission type flat-panel X-ray source using ZnO nanowire field emitters," *Appl. Phys. Lett.*, vol. 107, no. 24, 2015.

[57] A. Plankensteiner and P. Rödhammer, "Finite Element Analysis of X-Ray Targets," *Proceedings 15th International Plansee Seminar*, 2001. [Online]. Available: https://www-plansee-com.azureedge.net/fileadmin/user_upload/Finite_Element_Analysis_of_X-Ray_Targets.pdf.

[58] R. Behling, "The MRC 200: A new high-output X-ray tube," *Medicamundi*, vol. 35, no. 1, pp. 57–64, 1990.

[59] R. Behling, "Medical X-ray sources now and for the future," *Nucl. Instruments Methods Phys. Res. Sect. A Accel. Spectrometers, Detect. Assoc. Equip.*, vol. 873, pp. 43–50, 2017.

[60] R. Behling and F. Grüner, "Diagnostic X-ray sources—present and future," *Nucl. Instruments Methods Phys. Res. Sect. A Accel. Spectrometers, Detect. Assoc. Equip.*, vol. 878, no. May 2017, pp. 50–57, 2018.

[61] R. Behling, "Perfomance and pitfalls of diagnostic x-ray sources: an overview," *Med. Phys. Int. J.*, vol. 4, no. 2, pp. 107–114, 2016.

[62] R. Cierniak, *X-Ray Computed Tomography in Biomedical Engineering*. Springer, 2011.

[63] W. A. Kalender, “X-ray computed tomography,” *Phys. Med. Biol.*, vol. 51, no. 13, 2006.

[64] L. W. Goldman, “Principles of CT and CT technology,” *J. Nucl. Med. Technol.*, vol. 35, no. 3, pp. 115–128, 2007.

[65] V. Russo, M. Garattoni, F. Buia, D. Attinà, L. Lovato, and M. Zompatori, “128-slice CT angiography of the aorta without ECG-gating: efficacy of faster gantry rotation time and iterative reconstruction in terms of image quality and radiation dose,” *Eur. Radiol.*, vol. 26, no. 2, pp. 359–369, 2016.

[66] M. Yanagawa *et al.*, “Thin-section CT of lung without ECG gating: 64-detector row CT can markedly reduce cardiac motion artifact which can simulate lung lesions,” *Eur. J. Radiol.*, vol. 69, no. 1, pp. 102–107, 2009.

[67] B. Desjardins and E. A. Kazerooni, “ECG-Gated Cardiac CT,” *Am. J. Roentgenol.*, vol. 182, pp. 993–1010, 2004.

[68] E. G. Solomon, B. P. Wilfley, M. S. Van Lysel, A. W. Joseph, and J. A. Heanue, “Scanning-beam digital x-ray (SBDX) system for cardiac angiography,” in *SPIE Medical Imaging 1999 Conference*, 1999.

[69] P. R. Schwoebel, J. M. Boone, and J. Shao, “Studies of a prototype linear stationary x-ray source for tomosynthesis imaging,” *Phys. Med. Biol.*, vol. 59, no. 10, pp. 2393–2413, 2014.

[70] F. Sprenger *et al.*, “Distributed Source X-Ray Tube Technology for Tomosynthesis imaging,” *Proc SPIE*, vol. 7622, 2010.

[71] T. G. Schmidt, “What is inverse-geometry CT?,” *J. Cardiovasc. Comput. Tomogr.*, 2011.

[72] X. Xu, J. Kim, P. Laganis, D. Schulze, Y. Liang, and T. Zhang, “A tetrahedron beam computed tomography benchtop system with a multiple pixel field emission x-ray tube,” *Med. Phys.*, vol. 38, no. 10, pp. 5500–5508, 2011.

[73] T. Kim, Joshua; Lu, W; Zhang, “Dual source and dual detector arrays tetrahedron beam computed tomography for image guided radiotherapy,” *Phys. Med. Biol.*, vol. 59, no. 3, pp. 615–630, 2014.

[74] B. De Man *et al.*, “Multisource inverse-geometry CT. Part I. System concept and development,” *Med. Phys.*, vol. 43, no. 8, pp. 4607–4616, 2016.

[75] V. B. Neculaes *et al.*, “Multisource inverse-geometry CT. Part II. X-ray source design and prototype,” *Med. Phys.*, vol. 43, no. 8, pp. 4617–4627, 2016.

[76] B. Gonzales *et al.*, “Rectangular Computed Tomography using a stationary array of CNT emitters: Initial experimentel results,” in *Proc. SPIE 8668, Medical Imaging 2013: Physics of Medical Imaging*, 2013, vol. 8668.

[77] T. R. Mackie, B. J. Walker, and J. R. Seaton, “System and Method for Multi-Source X-ray- Based Imaging,” US 9,490,099 B2, 2016.

[78] “OOPIC PRO.” 2008.

[79] R. W. Powell, Ho C. Y., and P. E. Liley, “Thermal Conductivity of Selected Materials,” 1966.

[80] G. K. White and S. J. Collocott, “Heat Capacity of Reference Materials: Cu and W,” *J. Phys. Chem. Ref. Data*, vol. 13, no. 4, pp. 1251–1257, 1984.

[81] P. Tolias, “Analytical expressions for thermophysical properties of solid and liquid tungsten relevant for fusion applications,” *Nucl. Mater. Energy*, vol. 13, pp. 42–57, 2017.

[82] A. R. Kurochkin, P. S. Popel’, D. A. Yagodin, A. V. Borisenko, and A. V. Okhapkin, “Density of copper-aluminum alloys at temperatures up to 1400°c determined by the gamma-ray technique,” *High Temp.*, vol. 51, no. 2, pp. 197–205, 2013.

[83] A. Goldberg, “Atomic , Crystal , Elastic , Thermal , Nuclear , and Other Properties of Beryllium,” 2006.

[84] “Beryllium (Be).” [Online]. Available: https://janaf.nist.gov/tables/Be-001.html.

[85] W. J. Oosterkamp, “The heat dissipation in the anode of an x-ray tube: II. Loads of short duration applied to rotating anodes,” *Philips Res. Reports*, vol. 3, no. 3, pp. 161–173, 1948.

[86] J. T. Bushberg, J. A. Seibert, E. M. Leidholdt, and J. M. Boone, *The Essential Physics of Medical Imaging*. Wolters Kluwer, 2012.

[87] A. Poškus, “Evaluation of computational models and cross sections used by MCNP6 for simulation of electron backscattering,” *Nucl. Instruments Methods Phys. Res. Sect. B Beam Interact. with Mater. Atoms*, vol. 368, pp. 15–27, 2016.

VITA

Wesley William Tucker graduated from Missouri University of Science and Technology in May 2016 with a B.S. in Nuclear Engineering. He received his PhD in Nuclear Engineering from Missouri University of Science and Technology in May 2020. His research during his academic career focused on design of an x-ray source for real-time computed tomography, as well as CT image processing. Wesley was very active in teaching at Missouri S&T for both undergraduate and graduate level classes. While he was an undergrad, he co-founded the Nuclear Science Design Team and served as the first president.